ASSESSMENT OF HAND-TYPE HAMMER DRILL BITS UNDER PERCUSSIVE LOADING

A THESIS SUBMITTED TO
THE GRADUATE SCHOOL OF NATURAL AND APPLIED SCIENCES
OF
MIDDLE EAST TECHNICAL UNIVERSITY

BY

OSMAN KORAY DEMİR

IN PARTIAL FULFILLMENT OF THE REQUIREMENTS
FOR
THE DEGREE OF MASTER OF SCIENCE
IN
MECHANICAL ENGINEERING

MARCH 2007

Approval of the Graduate School of Natural and Applied Sciences

Prof. Dr. Canan ÖZGEN
Director

I certify that this thesis satisfies all the requirements as a thesis for the degree of Master of Science.

Prof. Dr. S. Kemal İDER
Head of Department

This is to certify that we have read this thesis and that in our opinion it is fully adequate, in scope and quality, as a thesis for the degree of Master of Science.

Prof. Dr. A. Erman Tekkaya	Prof. Dr. Mehmet Çalışkan
Co-Supervisor	Supervisor

Examining Committee Members

Prof. Dr. Suat Kadıoğlu	(METU, ME)	
Prof. Dr. Mehmet Çalışkan	(METU, ME)	
Prof. Dr. A. Erman TEKKAYA	(Atılım Uni., MFGE)	
Assoc. Prof. Dr. Uğur Polat	(METU, CE)	
Asst. Prof. Dr. Merve Erdal	(METU, ME)	

I hereby declare that all information in this document has been obtained and presented in accordance with academic rules and ethical conduct. I also declare that, as required by these rules and conduct, I have fully cited and referenced all material and results that are not original to this work.

Osman Koray DEMİR

ABSTRACT

ASSESSMENT OF HAND-TYPE HAMMER DRILL BITS UNDER PERCUSSIVE LOADING

Demir, Osman Koray
M.S., Department of Mechanical Engineering
Supervisor: Prof. Dr. Mehmet Çalışkan
Co-Supervisor: Prof. Dr. A. Erman Tekkaya

March 2007, 153 pages

The task of a drill bit in percussive drilling is to transport the initial kinetic energy of the hammer to the workpiece in terms of stress waves. The efficiency of this transportation and the stresses that the drill bit is exposed to during the process is dependent on the nature of the stress waves. In hand-type hammer drilling, changing dimensions of the bit means changing conditions for the propagation and interaction of the stress waves.

In this study, using finite element method, wave propagation and interaction in hand-type hammer drill bits is investigated with respect to drill bit dimensions. The main aim is to assess the effect of length and thickness on the efficiency and stress history of a hand-type drill bit. The results are evaluated in regard to workpiece hardness, which is a factor changing the effect of dimensions. In addition, chiseling test, which is used to prove bits under percussive loading, is carried out to detect differences between thin and thick drill bits, and the results are explained with the help of finite element simulations.

Conclusions are drawn revealing the efficiency and stress history of drill bits under percussive loading with respect to thickness, length and workpiece hardness. Finally, it is seen that the real-life results of chiseling test are in agreement with the simulation results.

Keywords: Percussive Drilling, Stress Waves, Finite Element Method, Efficiency, Chiseling Test.

ÖZ

EL TİPİ DARBELİ MATKAP UÇLARININ VURMA YÜKÜ ALTINDA DEĞERLENDİRİLMESİ

Demir, Osman Koray
Yüksek Lisans, Makina Mühendisliği Bölümü
Tez Yöneticisi: Prof. Dr. Mehmet Çalışkan
Ortak Tez Yöneticisi: Prof. Dr. A. Erman Tekkaya

Mart 2007, 153 sayfa

Vurarak delme işleminde matkap ucunun görevi çekicin başlangıçtaki kinetik enerjisini iş parçasına gerilme dalgaları cinsinden nakletmektir. Bu naklin verimliliği ve işlem boyunca matkap ucunun maruz kaldığı gerilmeler, gerilme dalgalarının durumuna bağlıdır. El tipi darbeli delme işleminde ucun boyutlarını değiştirmek, gerilme dalgalarının yayılma ve birbirine etki etme koşullarını değiştirmek demektir.

Bu çalışmada, sonlu eleman yöntemi kullanılarak, el tipi darbeli matkap uçlarında dalgaların yayılması ve birbirine etki etmesi, matkap ucu boyutlarına göre incelenmiştir. Temel amaç, boy ve kalınlığın bir el tipi matkap ucunun verimliliği ve gerilme geçmişi üzerindeki etkisini değerlendirmektir. Sonuçlar, boyutların etkisini değiştiren bir faktör olan iş parçası sertliğine bağlı olarak değerlendirilmiştir. Ayrıca, uçları vurma yükü altında denemek için kullanılan keski muayenesi, ince ve kısa matkaplar arasındaki farkları meydana çıkarmak için icra edilmiş, sonuçlar sonlu eleman simülasyonları yardımıyla açıklanmıştır.

Matkap uçlarının vurma yükü altındaki verimlilikleri ve gerilme geçmişlerini kalınlık, boy ve iş parçası sertliğine göre açıklayan sonuçlar çıkarılmıştır. Son olarak, keski muayenesinin gerçek hayat sonuçlarının simülasyon sonuçları ile uyum içerisinde olduğu görülmüştür.

Anahtar Kelimeler: Vurarak Delme, Gerilme Dalgaları, Sonlu Eleman Yöntemi, Verimlilik, Keski Muayenesi.

To My Family

ACKNOWLEDGEMENTS

I would like to express my appreciation and thankfulness to Prof. Erman Tekkaya for his encouragement and support that created this study.

I would like to thank Alper Güner, for his invaluable collaboration and friendship.

I would like to thank Prof. Mehmet Çalışkan for his kind help and support.

I would like to thank my colleagues Günter Domani, Martin Matheis and Ralf Bauman. The support provided by HILTI A.G. is greatly acknowledged.

I also wish to thank Dr. Merve Erdal, Prof. Suat Kadıoğlu and Dr. Uğur Polat for their suggestion and comments.

Thanks to all my colleagues in FİGES, leading Ercenk Aktay, Emre Karalarlı and Ufuk Penekli.

My best wishes to all FEMLAB members, Muin Öztop, Oya Okman, Erkan Önder, Erge Koray, Nagihan Topçu, Canderim Önder, Mert Aygen, and to Emrah Demirci.

I owe Hasan Ali Hatipoğlu for his precious helps and friendship.

I would like to thank Utku and Ogün for being my friends; and the thanks extend to Osman, Sinan, Korhan, Türkmen, Selçuk, Özgür, Murat, M.Eröz, Berat and Emine.

I have to thank ODTÜ-SAT; and I cannot exclude Camel, Tull and Caravan.

And Birgül, for her existence.

The special thanks go to my parents Ramazan Demir and Fatma Demir for their infinite support, and to my brother Emre Demir.

TABLE OF CONTENTS

LIST OF FIGURES

CHAPTER 1

INTRODUCTION

1.1 Percussive Drilling

Percussive drilling is basically a process in which high force intensity, short duration blows are applied in rapid succession to the workpiece. The blows are usually generated by the impact of an accelerated piston [1]. The acceleration can be performed by means of air or hydraulic pressure, or even gravity in more elementary tools [2].

The piston collides with a body that is usually called the drill bit, in order to transfer its kinetic energy by means of a stress wave. The stress wave travels through the drill bit until it hits the opposite end, in which the bit is in contact with the workpiece, usually rock or concrete. While drilling or breaking, high point stresses occur at the interface between the bit and the workpiece; hence, tungsten carbide inserts are mounted on the drill bit head [2].

Generally in percussion drilling tools, an additional element called anvil exists between the piston and the drill bit, and a thrust force can be applied over the drill. Furthermore, the drill bit can be continuously rotated [2]. A simple percussive drilling system can be seen in Figure 1.1.

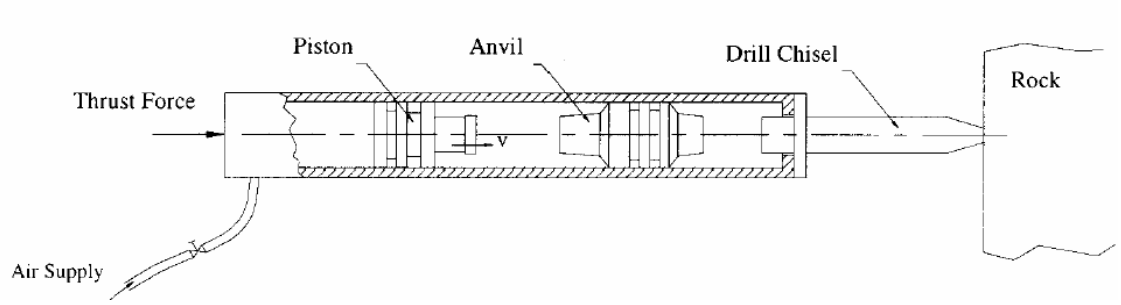

Figure 1.1 Schematics of a percussive drilling system [2].

1.2 Types and Utilization of Percussive Drilling

There are three main types of percussive drilling. Down-the-hole (DTH) drilling and hammer drilling can be distinguished by the length ratio of the hammer and the bit. In DTH drilling, that ratio is around one; while in hammer drilling, the length of the hammer is significantly smaller than the bit. In churn drilling, there is not a hammer, but the bit itself is accelerated to hit the workpiece. In Figure 1.2, three methods of percussive drilling can be seen [3].

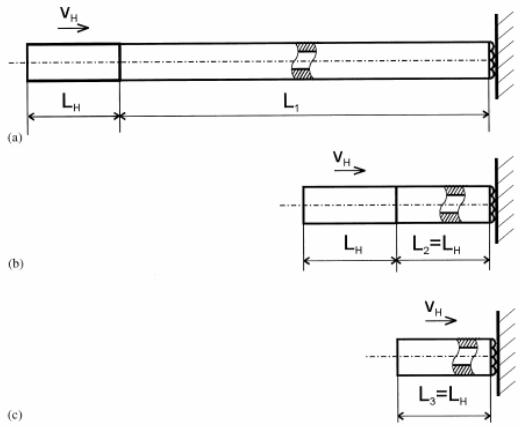

Figure 1.2 (a) Hammer drilling, (b) Down-the-hole drilling, (c) Churn drilling [3].

Percussive drilling is used in a wide variety of applications: drilling and breaking rock in mining industry, drilling and breaking concrete or pavement in construction industry, etc. [2].

In mining industry, rock drilling tools are normally used to drill 70-300 mm diameter holes, with depths varying from a few to hundreds of meters. In drilling of such deep holes by DTH drilling, the hammer (piston) itself has to be introduced into the hole [4]. This is not the case in hammer drilling, in which the hammer remains on the surface benefiting from the long drill bit. Hence, the stress wave has to travel through the long drill bit before hitting the workpiece.

The long distance to travel brings the disadvantage of stress wave attenuation in hammer drilling. Furthermore, DTH drilled holes tend to deviate less from a straight line. Therefore, DTH drilling is the preferred percussive drilling method in construction of mining pits, quarries and water dams [5].

1.3 Hand-Type Hammer Drilling

Although not the dominant one in mining engineering, hammer drilling is the method used in hand-type percussive drilling machines. Those devices are also called rotary hammers, demolition hammers, or hand-type hammer drills (Figure 1.3).

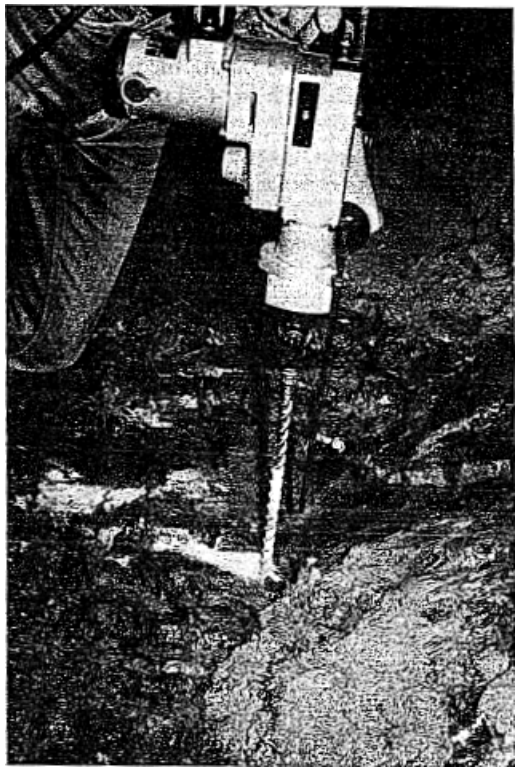

Figure 1.3 A standard hand-type hammer drill on rock [6].

Using hand-type hammer drills, holes shorter than a meter and having diameters of up to 52 mm can be drilled on rock, concrete or masonry. Hand-type hammer drills generally can be used with or without the rotating action; then the processes are called rotary hammering or chiseling, respectively.

In hand-type hammer drills, the blows are supplied by a flying piston, which is actuated by an electric motor driven piston by means of an air buffer. (Figure 1.4) The piston does not directly hit the drill bit, but an anvil exists between, like the system in Figure 1.1.

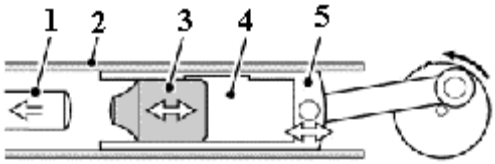

Figure 1.4 Pneumatic system used in hand-type hammer drills. (1) Anvil, (2) Housing, (3) Flying piston, (4) Compression chamber, (5) Piston cylinder [7].

When the hand-type hammer drill bits are examined, it can be seen that, there are three main sections of a drill bit: drill shank, drill rod (and spirals), and drill head. A sample drill bit can be seen in Figure 1.5.

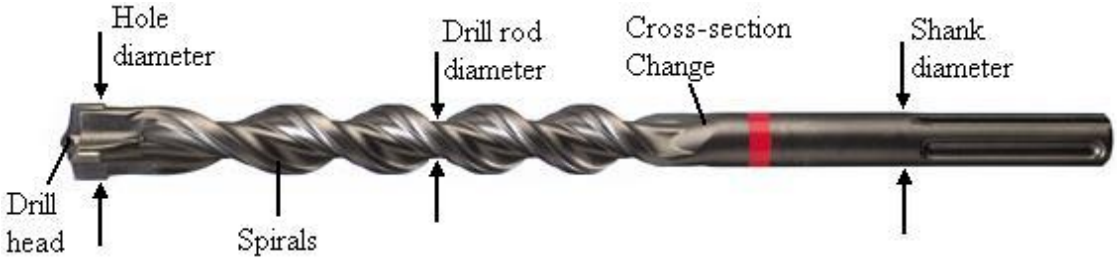

Figure 1.5 An hand type hammer drill bit [8].

The drill shank provides the connection with the drilling machine, and has standard dimensions. The diameters of the drill head and the drill rod varies with respect to hole diameter, which is equal to the outer diameter of the drill head. Generally, the diameter of the drill rod is much smaller than the diameter of the hole, because of the spirals and the drill head, as can be seen in Figure 1.5.

1.4 Aim and Scope

In the operation of hammer drilling tools, stress wave propagation is a fundamental issue. At the body interfaces and also at every geometric singularity within each body (i.e., cross-section change), those stress waves are partially reflected and transmitted. The rock itself also reflects a certain amount of energy back to the drill bit. The motion of the incoming and reflected energy waves in the drill bit is of overriding importance in the performance of the impact tools [2].

The performance of the impact tools and the effect of stress wave interactions on the performance are studied analytically, experimentally and numerically over a long period of time. However, the authors are generally interested in percussive drilling dedicated to mining, so the drilling tools investigated are DTH drilling tools, or hammer drilling tools with very long, uniform cross-section drill rods. Studies on design and performance of hand-type hammer drilling bits are very hard to find, as oppose to the wide usage of these tools.

In this study, a detailed assessment of the hand-type hammer drill bits under percussive loading is performed, using axisymmetric finite element simulations to model a single hit of the piston.

First, the performance of hammer drill bits is investigated in terms of dimensions of the drill rod and characteristics of the workpiece.

The next chapter deals with the stresses observed along the bits. The maximum tensile and compressive stress values reached are examined with respect to the same parameters used in the performance investigation.

The final step is to simulate chiseling test, which is used for evaluating hammer drill bits under percussive loading. In this chapter, real life test results are explained by the help of finite element simulations.

CHAPTER 2

LITERATURE SURVEY

2.1 Introduction

In this chapter, previous studies on percussive drilling are going to be summarized.

In 1958, Topanelian [9] compared conventional and percussion drilling by experiments. According to the results, percussion superimposed on conventional drilling more than doubled the penetration rate of the drilling process in meter penetration per hour. The author also shows that the total penetration increases with the frequency of blows.

In 1959, Hartman [10] focuses on a single impact. He changes the kinetic energy of the hammer while the velocity is constant, and the velocity of the hammer while the energy is constant. The aim is to see the effects of these parameters on penetration depth and volume of the crater created. The results are in Figure 2.1.

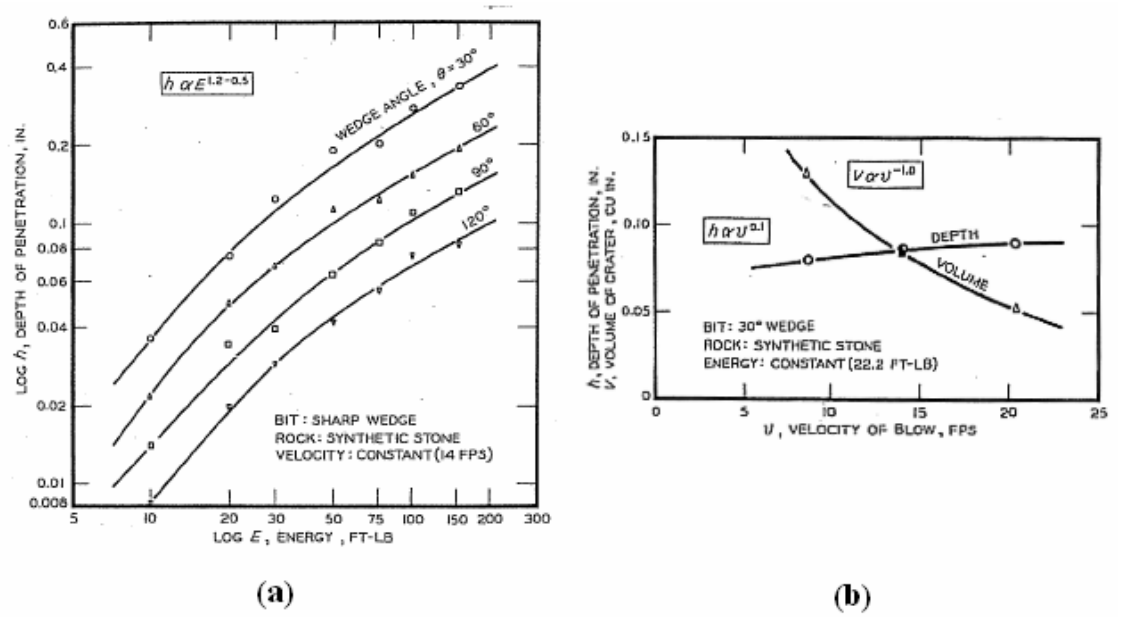

Figure 2.1 (a) Effect of blow energy on penetration depth, (b) Effect of blow velocity on penetration depth and volume of crater [10].

As can be seen in Figure 2.1a, penetration depth for a single blow increases with the blow energy and the wedge angle of the bit. However, Figure 2.1b shows that it is not so much dependent on the blow velocity. In addition, according to Figure 2.1b, volume of crater created decreases with the velocity. The author states that there is probably an optimum blow energy and velocity for any combination of bit shape and rock type.

Following the first basic ones in 1950's, the studies gain acceleration. They can be classified according to the section of percussive drilling they focus on:

- Studies on the piston impact,
- Studies on the characterization of the workpiece under percussive loading,
- Studies on energy transfer from the bit to the workpiece (efficiency),

- Studies taking stress wave interactions into account.

Below, the studies on those fields are going to be summarized one by one. Lastly, two studies that are focused especially on hand-type hammer drilling are going to be given.

2.2 Piston Impact

In 1961, Fairhurst [1] considers a simple percussive system (Figure 2.2) and calculates the stress waveforms created by the piston impact. The calculation and experimental results (solid and dashed lines, respectively) for varying piston geometries are given in Figure 2.3.

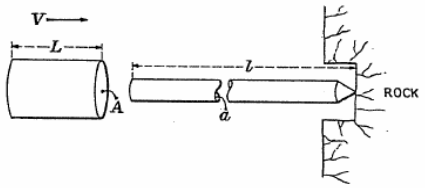

Figure 2.2 Basic percussive drilling system [1].

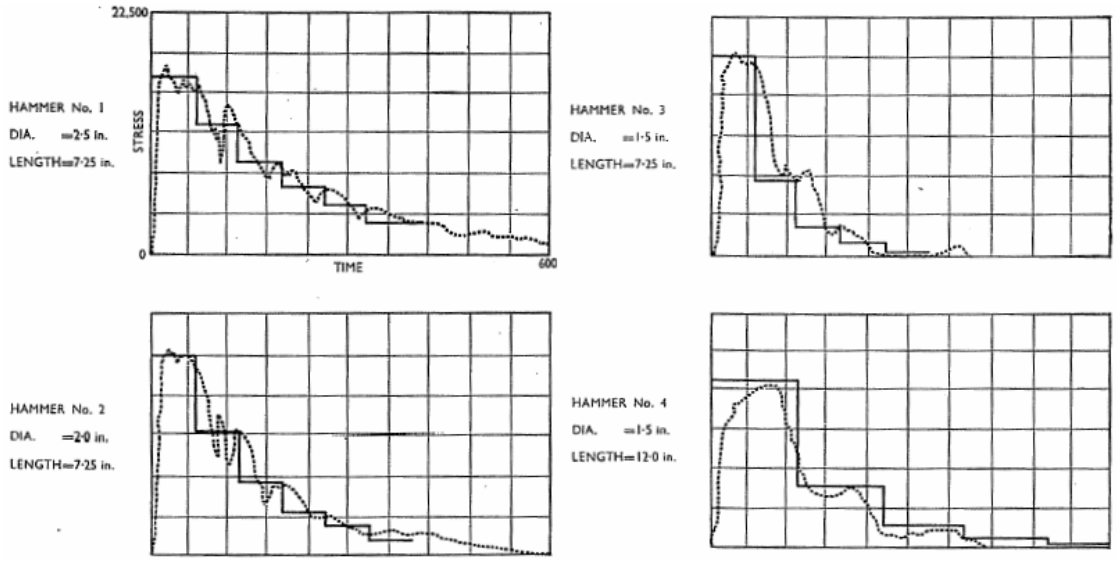

Figure 2.3 Comparative stress pulses for variable hammer dimensions [1].

The author considers the agreement between theoretical and experimental stress levels to be within the limit of experimental error. He also notes that the stresses measured are not developed instantaneously, and explains that with the fact that the full contact is not developed between the striking surfaces instantaneously.

All the pistons used in the experiments have uniform cross-section, and characteristic impedance (see Appendix A) greater than the drill bit. Observing Figure 2.3, the typical properties of the stress waveforms created by such pistons can be deduced: The waves are composed of successive square waves monotonically decreasing in dimension. The dimensions of the piston change the dimensions of the square waves.

The author also gives the waveform created by a piston with the shape shown in Figure 2.4 (which is called “the shank piston”).

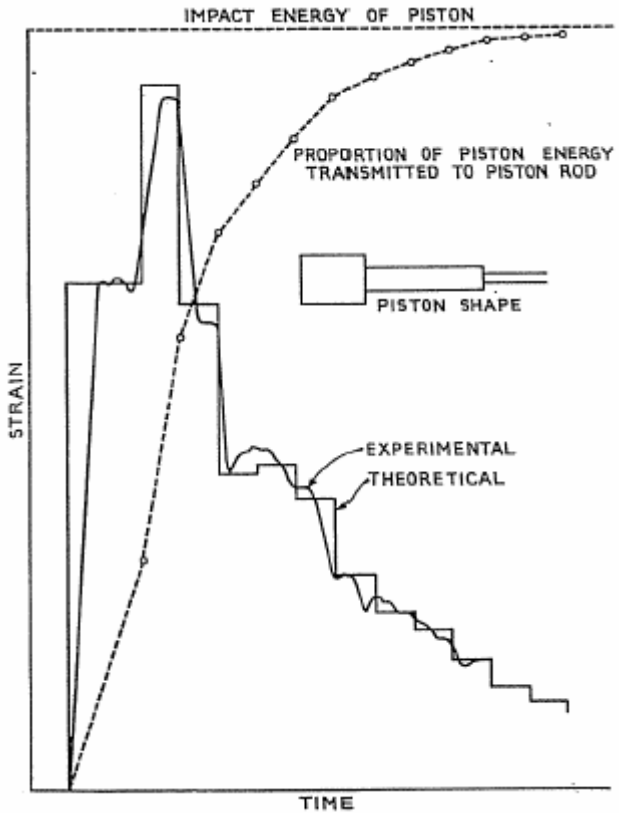

Figure 2.4 Theoretical and experimental strain curves for a rod impacted by a shank piston [1].

A characteristic feature of a waveform generated by a shank piston is that the peak strain occurs at the second step. Interestingly, that peak strain value is greater than the peak value of a wave created by a uniform piston with a diameter equal to the larger diameter of the shank piston [1].

In 1968, Dutta [11] writes a computer code to make the calculations to determine waveforms easier. He calculates waveforms for various piston designs, some of which are given in Figure 2.5.

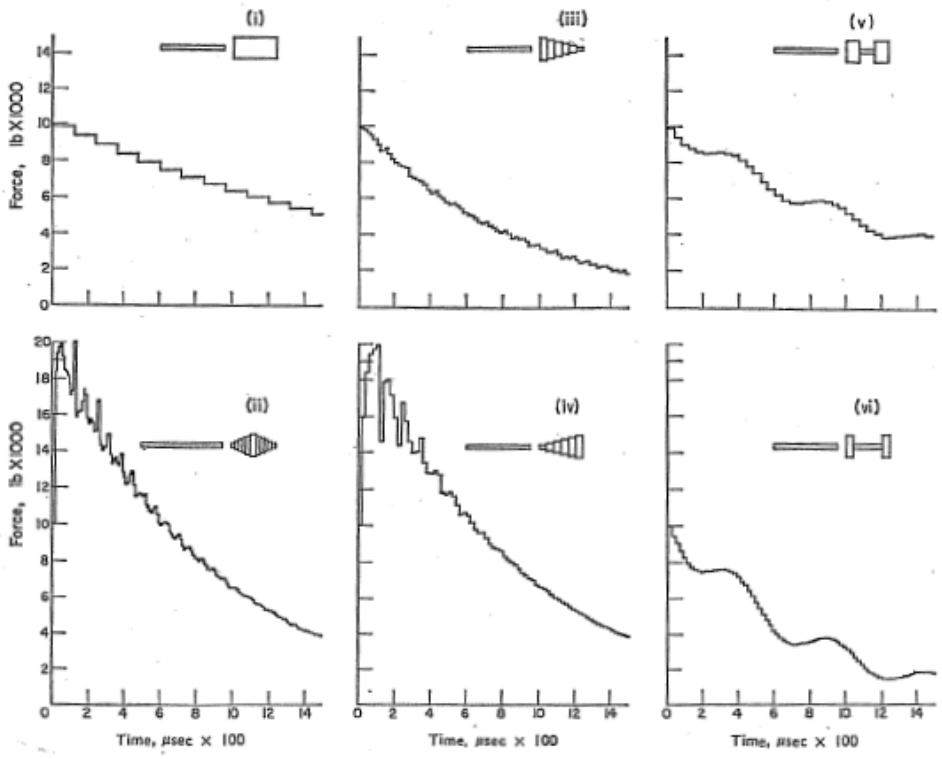

Figure 2.5 Stress waveforms computed for six pistons of different geometries. Drill rod diameter 1 in., maximum piston diameter 6 in., and length 12 in. [11].

Although the form of the stress wave can be determined from the geometry of the piston, it is generally much more difficult to design the geometry of the piston to produce a desired waveform. In 1998, Liu and Li [12] developed the "Impact Discrete Inverse Method" to solve such a problem. Lok et al. [13] used this method to obtain a half-sine waveform (Figure 2.6).

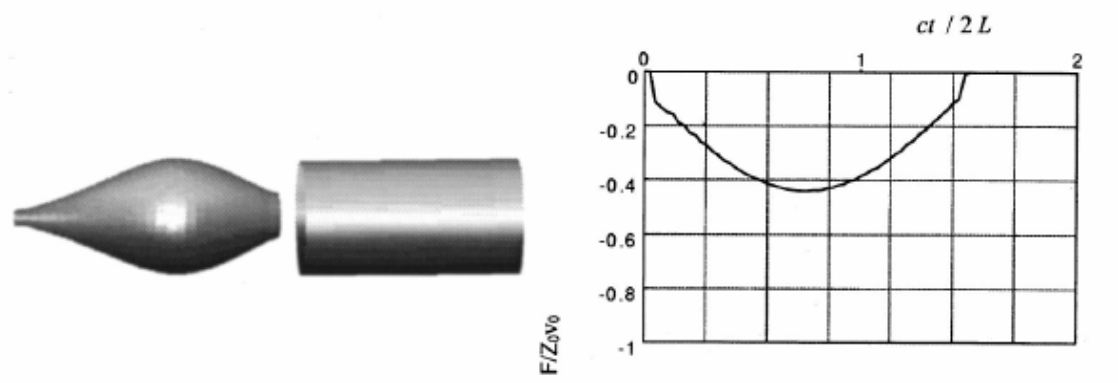

Figure 2.6 Designed profile of impacting piston and the resulting waveform [13].

2.3 Characterization of the Workpiece

In percussive drilling, as a result of the piston impact, a compressive stress wave hits the drill bit-workpiece interface, and a net penetration of the drill bit occurs into the workpiece. In this section, the studies that are aiming to determine the force-penetration (*F*-*P*) characteristic of the workpiece under percussive loading are going to be summarized.

Because of the difficulty of accurately measuring instantaneous penetration during impact, Fairhurst [1] benefits from the fact that the resultant force on the drill head must equal the force *F* on the workpiece, that is

$$A \cdot (\sigma_i + \sigma_r) = F \,, \tag{1}$$

where A is the cross-sectional area of the bit, and σ_i and σ_r are the incident and reflected stress waves, respectively.

Besides that, the well-known relationship between the stress amplitude, σ, and the particle velocity, v, of a one dimensional (1-D) stress pulse is:

$$v = \frac{c \cdot \sigma}{E} \qquad \text{or} \qquad \sigma = \rho \cdot c \cdot v \quad , \tag{2}$$

where E is the elastic modulus, ρ is the density of the media and $c = \sqrt{\frac{E}{\rho}}$ (elastic wave speed). Benefiting from Equation 2, the penetration velocity can be derived by assuming the bit initially stationary:

$$\frac{c}{E} \cdot (\sigma_i - \sigma_r) = v_c \quad , \tag{3}$$

where v_c is the velocity of the bit to the workpiece, or equally, the penetration velocity. Here it must be noted that the compressive stresses are taken to be positive and *vice versa*, in the calculations.

Utilizing Equation 1, Equation 3 and the known time variations of the incident and reflected stress waves, one can find the force and velocity variations of the bit, which can yield the *F-P* relationship easily.

The author measures the incident and reflected waveforms on a hammer drilling system by strain gauges, and derives the force-displacement characteristic of an 18 in. rock cube for a single piston impact. A 2 ft. long, 1 in. diameter piston is used to strike a 10 ft. long, 1 in. diameter rod in the measurement. The resulting *F-P* curve can be seen in Figure 2.7.

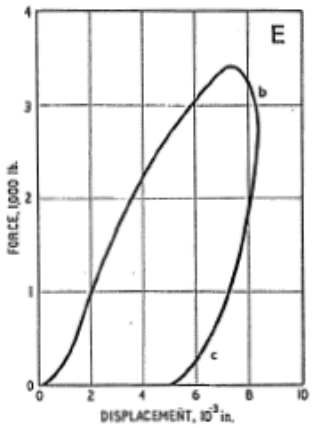

Figure 2.7 *F-P* characteristic of rock [1].

Hustrulid and Fairhurst [14] conduct dynamic tests and direct determination technique to determine the *F-P* characteristic of rock. They use a drop tester in which the bit is attached to a heavy mass and allowed to free fall onto the rock. The *F-P* results of 16 successive drops are given in Figure 2.8.

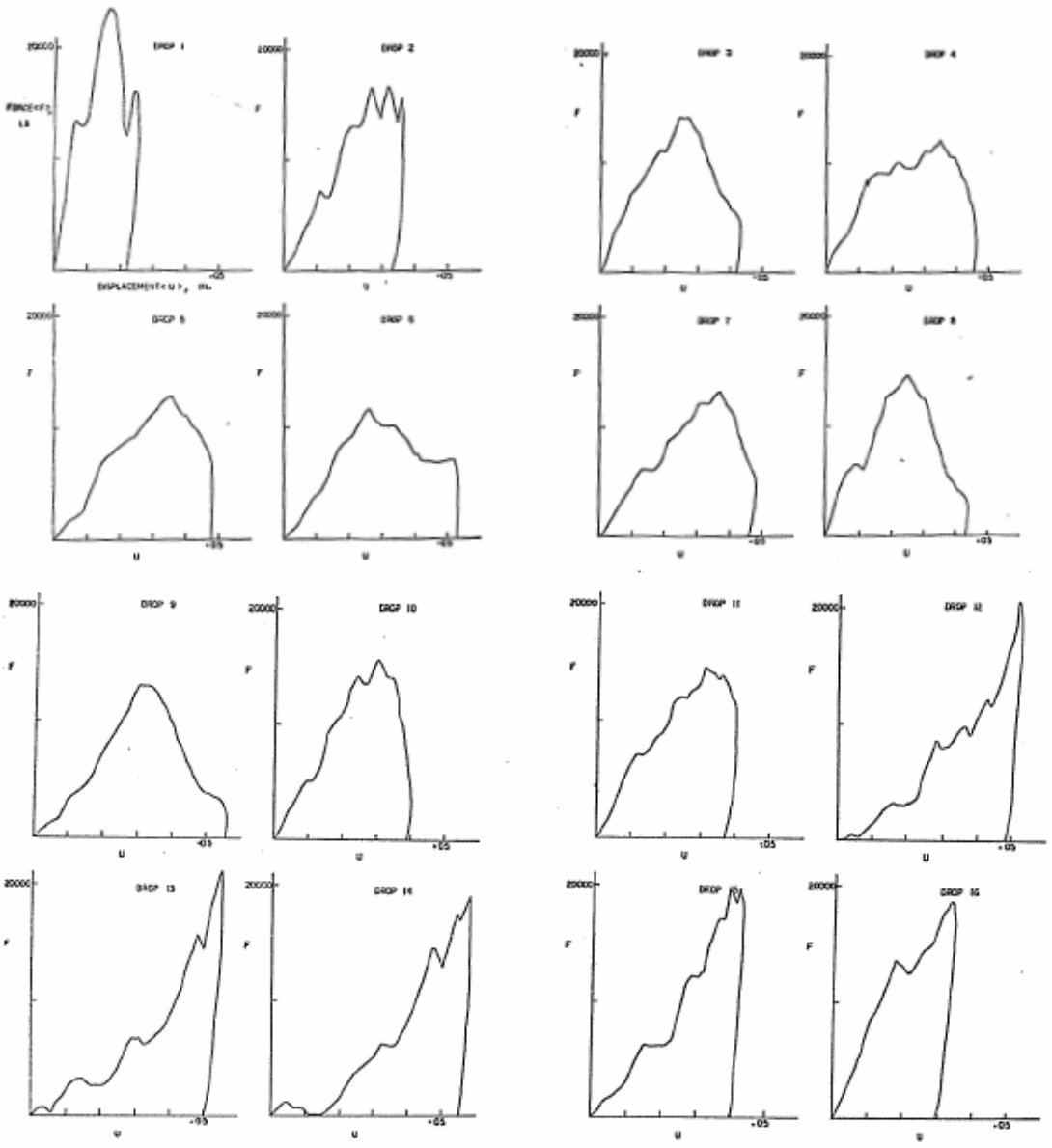

Figure 2.8 Dynamic *F*-*P* curves of granite for 16 successive drops [14].

In 1977, Lundberg and Henchoz [15] improve the methodology used by Fairhurst [1]. When the strain is measured at one cross-section only, like Fairhurst does, there is a minimum requirement for the length of the drill bit. This is because waves traveling in different directions must not overlap at the point of strain measurement. That restriction disappears when the strain is measured at two cross-sections: The waves do not need to be separated while measuring, since they are separated in the analysis of the measured strains. The method is called two-point strain measurement method.

The first version of the method was able to be used in rods with uniform cross-section [15]. In 1990, Lundberg et al. [16] modify the method to include non-uniform rods.

Carlsson et al. [17] use the method to measure the *F-P* curve in a DTH drilling system. The results can be seen in Figure 2.9.

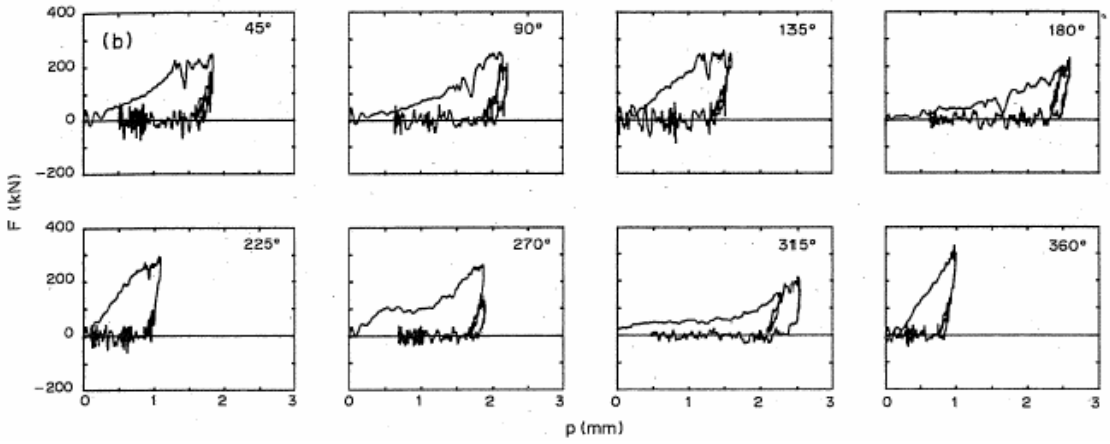

Figure 2.9 *F-P* relations obtained for 8 hits by two-point strain measurement [17].

Figure 2.9, and other studies that are mentioned up to this point reveal a general shape for the *F-P* behavior of stones under percussive drilling. A typical one is given in Figure 2.10.

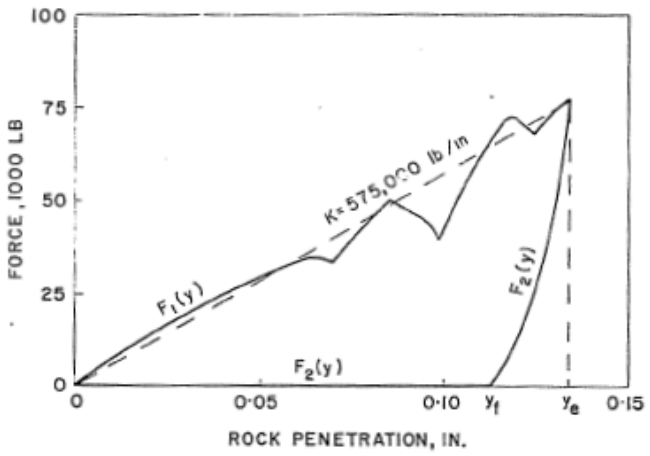

Figure 2.10 A typical workpiece *F-P* curve in stone percussive drilling [18].

It can be seen in Figure 2.10 that F(y) represents a closed hysteresis loop in the positive quadrant of the force-penetration plane [18]. During $F_1(y)$, elastic deformation and crushing of the workpiece is represented by the curves of positive slope and regions of chip formation or sudden fractures by those of negative slope. The quantity y_e is the peak penetration of the bit, while y_f is the final penetration. Because of the elastic expansion of the stone, which is represented by $F_2(y)$, the y_e is less then y_f by the amount of this elastic expansion [14].

The slopes in *F-P* curve of any drilling system depends on numerous factors like the stone type (hardness, brittleness, homogeneity, elastic behavior), bit head geometry

(wedge angle), fluids used in the drill hole, and the amount of stone debris at the bottom of the hole [1, 14].

For practical considerations, the typical *F-P* relationship is generally represented by a bilinear curve with loading and unloading phases, which can be seen in Figure 2.11.

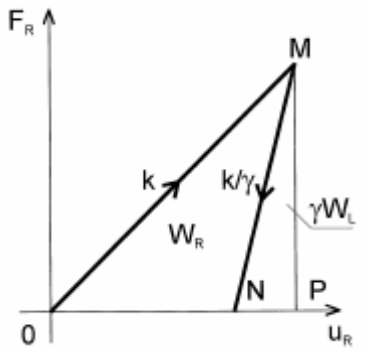

Figure 2.11 Bilinear *F-P* relationship [3].

In Figure 2.11, line OM represents the loading phase characterized by the penetration resistance k, and line MN represents the unloading phase. The slope in the unloading phase depends on γ, which is generally called the unloading parameter. γ takes values between 0 and 1, which makes the workpiece perfectly inelastic or perfectly elastic, respectively. After the loading and unloading phases, the total work done on the workpiece (W_R) can be calculated by

$$W_R = W_L - W_U \,, \tag{4}$$

where W_L is the work done during the loading phase, and W_U is the energy returned to the drill during the unloading phase. W_U can be found by

$$W_U = \gamma \, . \, W_L \, . \tag{5}$$

In workpiece modeling by a bilinear curve, in case of a force reduction during force application along line OM, the unloading will take place along line MN. In case of a second force increase (*e.g.* repeated piston impact, or a decrease and then an increase in the incoming stress wave), the force value at point M must be exceeded for further inelastic deformation take place.

This way of workpiece modeling neglects chipping and sudden fractures that prevents penetration resistance increase infinitely, however, leads quite acceptable approximations as it is going to be revealed later by Lundberg [19].

In 2004, Chiang [4] criticizes the method of two-point strain measurement because of its noise sensitivity. He claims that the noise cannot be eliminated by using filtering techniques because signals (strain waves) have themselves significant high frequency components due to wave reflection occurring in the elastic bodies. He proposes a new method to obtain *F-P* curves based on parameter adjustment. Although it does not give exact curves, this method has the advantage of being very robust and requiring minimum experimental setup.

In the mentioned method, a 1-D computer model of the experimental setup is prepared using the computer simulation program developed by the author. The program can give the theoretical stress time-history at any section of the drill. The next step is to assume a tentative *F-P* curve such as the one in Figure 2.11.

According to the author, for a given drilling system, the theoretical stress time history at any section is dependent on two major parameters, which are the impact velocity, and the slope k of the loading phase of the *F-P* curve. The author calculates the

theoretical stress time-history and compares the results with experiments. Knowing the impact velocity, the parameter k can be adjusted to fit the theoretical stress response at an arbitrary section to the experimental measurements at the same section.

The adjustment, which is done by a bisection iterative scheme, finally gives the parameter k that best represents the response of the workpiece.

2.4 Efficiency

For 100% efficiency, the energy carried by the incident stress wave must be transmitted to the workpiece completely. According to Fairhurst [1], the efficiency of energy transfer from the drill bit to the workpiece is determined by the boundary conditions at the bit-rock interface: Complete transmission can occur only if the penetration impedance of the rock matches the characteristic impedance of the bit.

The characteristic impedance of the bit is given by (see Appendix A):

$$z_b = \rho_b \cdot c_b \cdot A_b \quad . \tag{6}$$

The penetration impedance of the rock is the ratio of the instantaneous bit force to the instantaneous bit penetration velocity. Like *F-P* characteristic, this is not a unique property of rock, being dependent on many parameters of workpiece and bit [1].

According to Fairhurst [1], observation of the typical *F-P* curves in percussive drilling (see Section 2.3) indicates immediately that it is impossible to completely match the rod impedance to the penetration impedance at all times during penetration, since the latter approaches zero at the start of penetration (lowest force, maximum rate of penetration) and becomes infinite at the end when the force is a maximum and the rate

of penetration is zero. This mismatch of the impedances results in reflection of energy back into the drill bit in the form of a stress wave.

Simon [18] derives equations for the efficiency computation of conversion of stress wave energy into work done on the workpiece.

Starting points for the derivations are the Equation 1 and Equation 3 in the following forms, respectively:

$$F = A \cdot \left[\sigma_i(t) + \sigma_r(t)\right] + F_0\,, \tag{7}$$

$$\frac{dy}{dt} = \frac{1}{\rho \cdot c} \cdot \left[\sigma_i(t) - \sigma_r(t)\right] + v_0\,, \tag{8}$$

where F is the instantaneous force between the bit and the rock, dy/dt is the velocity of the bit into the rock, and algebraic sign of y is positive for displacement toward the rock. F_0 and v_0 stand for any force that may exist between the bit and the rock and any velocity that the bit may have, prior to the arrival of stress wave. It is also to be noted that compressive stresses are taken to be positive and tensile stresses negative in calculations for convenience.

Equations 7 and 8 can be combined by eliminating $\sigma_r(t)$ to obtain:

$$\frac{dy}{dt} + \frac{1}{A \cdot \rho \cdot c} \cdot \left[F(y) - F(y_0)\right] = \frac{2}{\rho \cdot c} \cdot \sigma_i(t) + v_0\,, \tag{9}$$

writing $F(y)$-$F(y_0)$ for F-F_0. This means assuming one-to-one correspondence between F and y. "This correspondence presumes the absence of any appreciable rate of loading effects for the range of loading involved in percussion drilling [18]."

The function *F(y)* is the *F-P* characteristic. The author assumes a bilinear one like the one given in Figure 2.11, taking the slope of the loading line as *K* and neglecting the elastic re-expansion (unloading) phase. So,

$$F(y) = K \cdot y \,. \tag{10}$$

For the convenience in computations, the mathematical expression

$$\sigma_i(t) = \sigma_m (t / n\tau)^n \cdot \exp\left[n - (t/\tau)\right] \tag{11}$$

is employed for the incident stress waveform. This function, which has a maximum value of σ_m at $t = n\tau$, is illustrated in Figure 2.12 for n = 0, 1 and 2.

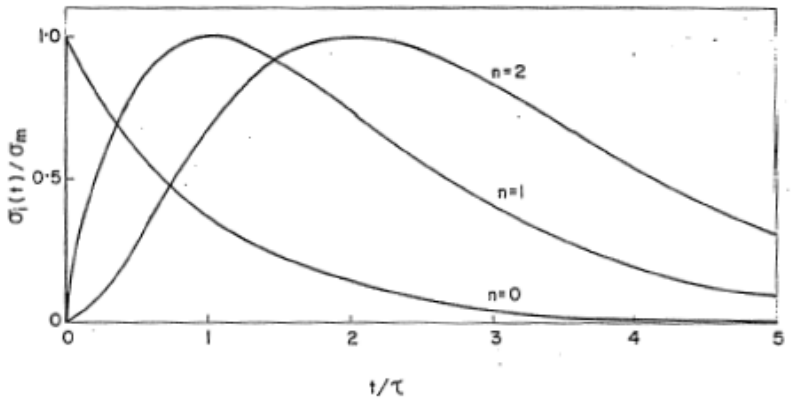

Figure 2.12 Incident stress waveforms used in the computations, as given by Equation 11 [18].

Substituting Equations 10 and 11 into Equation 9 for the case of $v_0 = 0$ and $F_0 = 0$ results in:

$$\frac{d\xi}{d\theta} + \Pi_1 \cdot \xi = 2 \cdot \left(\frac{\theta}{n}\right)^n \cdot \exp(n - \theta) \quad , \tag{12}$$

where $\xi \equiv (\rho \cdot c / \sigma_m \cdot \tau) \cdot y$ is the dimensionless displacement, $\theta \equiv t / \tau$ is the dimensionless time, and $\Pi_1 \equiv K \cdot \tau / A \cdot \rho \cdot c$ is a dimensionless parameter that incorporates the *F-P* characteristic (*K*), characteristic of the stress waveform (τ), and the properties of the drill rod (ρ, *c* and *A*).

If y_{max} is the maximum penetration of the bit, the energy output to the workpiece, E_0, is given by:

$$E_0 = \int_{y_0}^{y_{max}} F(y) \cdot dy \quad , \tag{13}$$

and the energy in the incident stress wave is given by:

$$E_i = (A / \rho \cdot c) \cdot \int_0^{\infty} [\sigma_i(t)]^2 \cdot dt \quad , \tag{14}$$

As *F(y)* and $\sigma_i(t)$ are known from equations 10 and 11, y_{max} is the missing parameter for the efficiency E_0 / E_i to be computed. Solutions of Equation 12 for the initial conditions of $\xi = 0$ when $\theta = 0$ can be obtained for *n* = 0, 1, and 2. From these solutions the values of $\xi_{max} \equiv (\rho \cdot c / \sigma_m \cdot \tau) \cdot y_{max}$ are found for which $d\xi / d\theta = 0$. The efficiency is then given by

$$Eff. = \Pi_1 \cdot {\xi_{\max}}^2 / 2 \cdot \int_0^{\infty} (\theta / n)^{2n} \cdot \exp\left[2 \cdot (n - \theta)\right] \cdot d\theta \quad . \tag{15}$$

Equation 15 is important as it reveals the factors effective on the efficiency of energy transmission between bit and rock. It can be seen that the efficiency is a function of the two dimensionless parameters Π_1 and n. These two parameters represent the incident waveform, the *F-P* characteristic of the workpiece and the material properties of the bit [18].

Figure 2.13 shows the efficiency with respect to Π_1 for n = 0, 1 and 2.

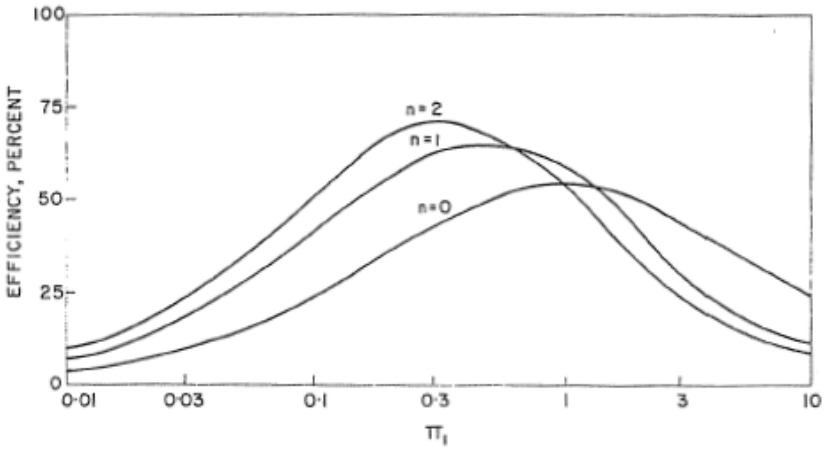

Figure 2.13 Efficiency of energy transfer to the workpiece [18].

As can be seen in Figure 2.13, the stress waveforms in the higher order are superior to the lower order ones in terms of efficiency.

The author performs the efficiency calculations also for the rectangular incident waveform given by

$$\sigma=\sigma_m,\ 0<t<\tau$$
$$\sigma=0,\ t\geq\tau \text{ and } t\leq 0 \quad . \tag{14}$$

The result is given in Figure 2.14 by the solid line. It can be seen that the ≥50% efficiency region is larger than the curves in Figure 2.13, and the peak efficiency is as high as 82%.

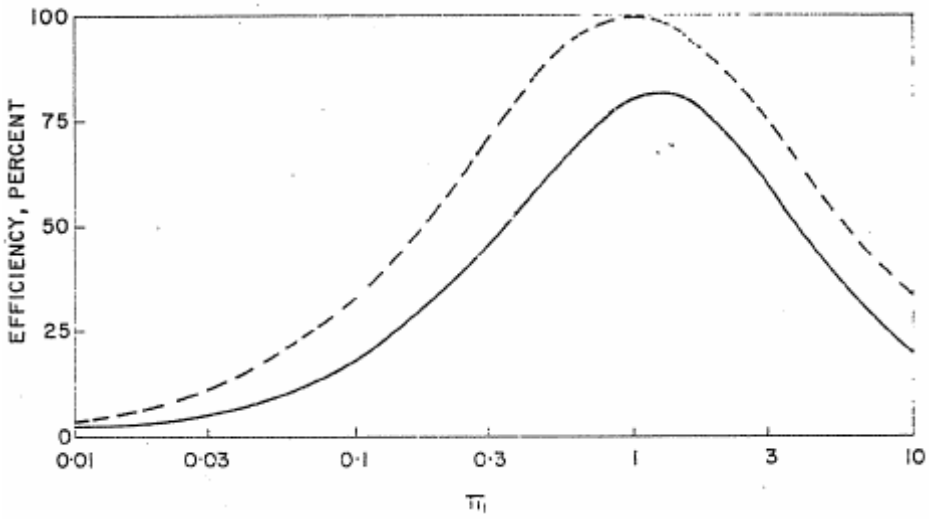

Figure 2.14 Efficiency of energy transfer to the workpiece [18].

Figure 2.14 also includes the efficiency curve for the exponentially increasing function given by:

$$\sigma_i(t) = \sigma_m \cdot \exp(+t/\tau) \quad . \tag{15}$$

It can be seen in Figure 2.14 that the efficiency for this case reaches 100% at Π_I=1.

The author then investigates the possibility of reaching 100% efficiency with some combination of the waveforms in Equation 11 with an *F-P* characteristic that is non-linear in the loading region. Since the condition of 100% energy transfer means no energy reflection, assuming $\sigma_r = 0$ yields

$$F = A \cdot \sigma_i(t) \tag{16}$$

$$y = (1/\rho \cdot c) \cdot \int_0^t \sigma_i(t) \cdot dt \quad , \tag{17}$$

when $y_0 = F_0 = v_0 = 0$.

Equations 16 and 17 make it possible to compute F as a function of y, using t as the computational parameter. The results are given in dimensionless form of $F/\sigma_m A$ as a function of dimensionless displacement $(\rho \cdot c/\sigma_m \cdot \tau) \cdot y$ in Figure 2.15.

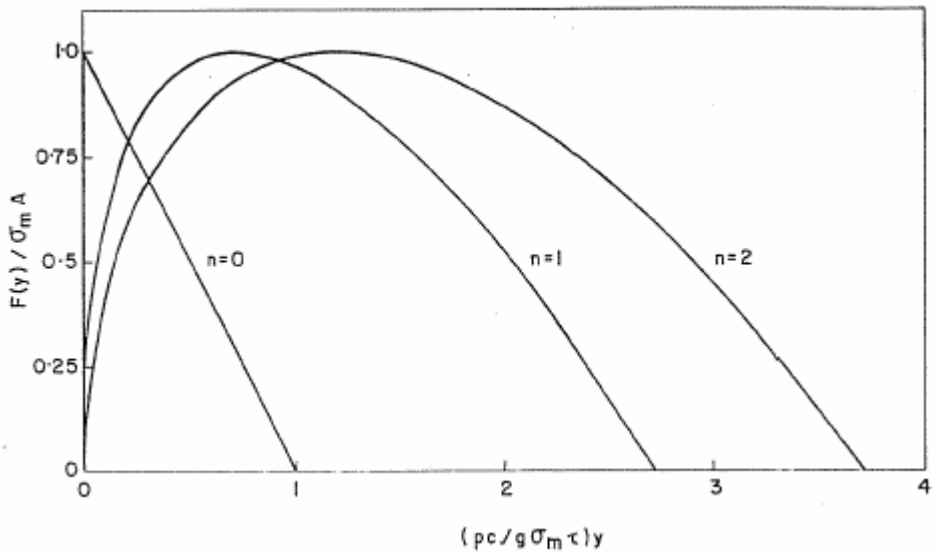

Figure 2.15 *F-P* curves for 100% efficiency with incident waveforms of Equation 11 [18].

According to Simon [18], it would seem to be virtually impossible to obtain a decreasing force between a bit and a rock with increasing dept of penetration such as presented in Figure 2.15. Rapid temporary decreases in force with increasing penetration may occur momentarily due to rock fractures (see Figure 2.10); however, it is apparently not feasible to obtain a decrease in the average force with increasing penetration.

In 1973, Lundberg [19], like Simon [18], calculates the efficiency of the energy transfer between the drill and the workpiece based on assumed forms of incoming stress wave and *F-P* relationship. Unlike Simon, Lundberg does not neglect the unloading phase, and includes the dimensionless unloading parameter, γ (see Figure 2.11).

While E is the elastic modulus, A is the cross-sectional area of the drill bit, c is the elastic wave speed in the drill bit, σ_i and σ_r are the incident and the reflected stress waves and t is the time, the author uses the dimensionless time

$$\tau = t / t_0 \ , \tag{18}$$

where

$$t_0 = A \cdot E / k \cdot c \ \ , \tag{19}$$

and dimensionless stresses

$$s_i = \sigma_i / \sigma_0 \tag{20}$$

and

$$s_r = \sigma_r / \sigma_0 \ , \tag{21}$$

where σ_0 is a nominal stress.

First, the efficiency calculations are made with a triangular incident stress waveform that is illustrated in Figure 2.16

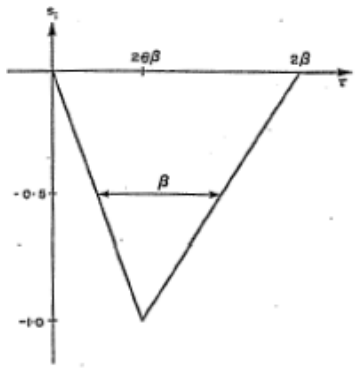

Figure 2.16 Incident stress wave [19].

β is the non-dimensional half-width of $s_i(\tau)$ and θ ($0 \leq \theta \leq 1$) determines the position of the peak amplitude along the time-axis. Thus, β and θ represent the width and shape of the incident stress wave, respectively.

The efficiency (η) results for the triangular stress wave are given in Figure 2.17.

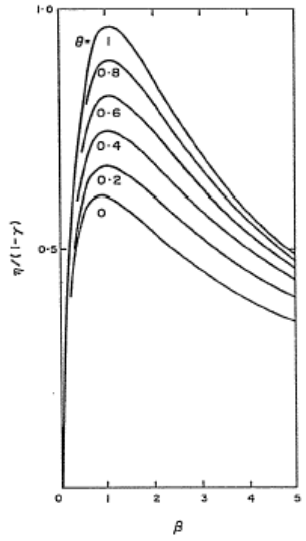

Figure 2.17 $\eta/(1-\gamma)$ vs. β for different values of θ [19].

As can be seen in Figure 2.17, when the other variables are constant, the efficiency is an increasing function of θ. This result reveals that a stress wave with low amplitude at the beginning and high amplitude at the end leads to a higher efficiency than one with the opposite properties. According to the author, this is because with such a stress wave, the amplitude follows, more or less, the increase in force on the penetrating bit. Recall that, it was shown by Simon [18] that a stress wave with exponentially increasing magnitude leads to 100% efficiency.

Second, the author selects the stress waveform given in Figure 2.18 for the efficiency calculations. That is selected because it is the waveform generated by a cylindrical hammer with characteristic impedance greater than or equal to the impedance of the rod, as was given in Section 2.2 in Figure 2.3.

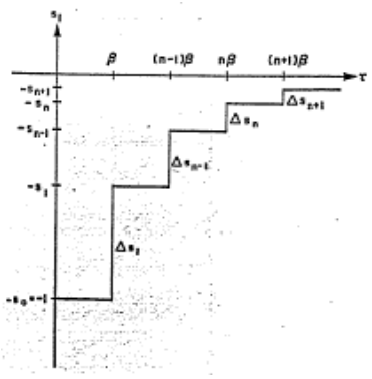

Figure 2.18 Incident stress wave [19].

β is the non-dimensional width of each constant amplitude segment of the stress wave, which is equal to the time for the stress wave travel the hammer back and forth:

$$\beta = t_p / t_0 \ , \tag{22}$$

where

$$t_p = 2 \cdot L_H / c_H \ , \tag{23}$$

and L_H and c_H are the length and the elastic wave speed of the hammer (t_0 is given in Equation 19).

R determines the ratio q of the amplitudes of two successive segments of the stress wave according to the equation:

$$q = (R-1)/(R+1) \ , \tag{24}$$

Thus, β and R represent the width and shape of the incident stress wave, respectively. When R=1, the incident wave is a square pulse with magnitude -1 and length β. When R is greater than 1, a tail is added to that square pulse. As R increases, the tail gets greater: When R=2, tail is made of successive square segments with magnitudes 1/3, 1/9, etc., and when R=5, with magnitudes 2/3, 4/9, 16/81, etc.

The efficiency results for such a stress wave with respect to R and β are given in Figure 2.19.

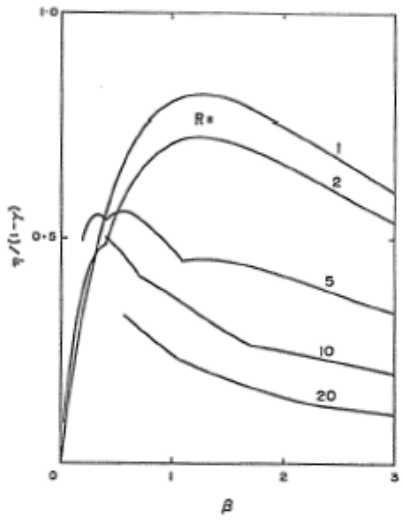

Figure 2.19 $\eta/(1-\gamma)$ vs. β for different values of R [19].

Figure 2.19 indicates that waves with larger tails generally lead to lower efficiencies than waves with smaller tails. A wave with a larger tail stores more energy, but it is evident that a great portion of energy stored in the tail is reflected by the workpiece, after the penetration resistance of the workpiece increase substantially. Adding a tail to the wave increases the efficiency for small β values, i.e. for short incident waves. So

the energy of the tail can be transmitted the workpiece before the penetration resistance reach high values.

After evaluating triangular and stepped stress waves with a bilinear *F-P* characteristic, the author evaluates a rectangular stress wave with non-linear *F-P* characteristics. First, the non-linear *F-P* relationship

$$F = k \cdot (1 + x / d) \cdot x \tag{25}$$

is going to be considered. This is an *F-P* relationship, in which the force increases non-linearly with displacement (Figure 2.20).

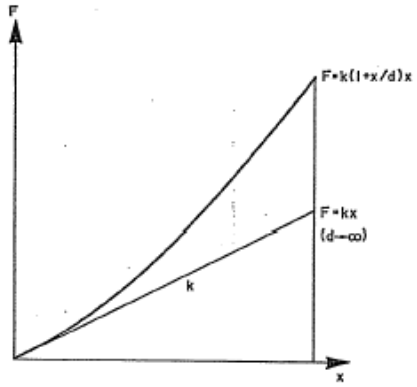

Figure 2.20 *F-P* relationship with a parabolic loading region [19].

As can be seen in Figure 2.20, the author neglects the elastic re-expansion of the workpiece. Parameter *d* is a measure of the non-linearity of the curve. Dimensionless parameter ε is going to be used instead of *d*, being

$$\varepsilon = x_0 / d \quad (\geq 0)\,, \tag{26}$$

where

$$x_0 = 2 \cdot A \cdot \sigma_0 / k \ . \tag{27}$$

The results are given in Figure 2.21.

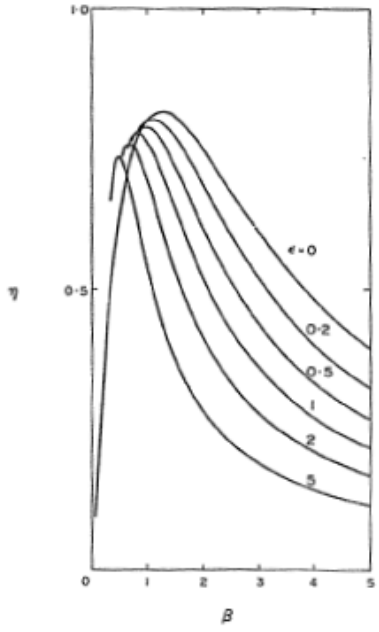

Figure 2.21 η vs. β for different values of ε [19].

As can be seen in Figure 2.21, efficiency decreases with the non-linearity of the *F-P* curve. This is an expected result, because it is known that, for high efficiency, the increase in the magnitude of the incident stress wave should match the increase in the force of the *F-P* characteristic. It was also revealed before that only an incident

waveform with exponentially increasing stress is capable of matching the increase in a linear *F-P* relationship.

However, the assumed waveform is rectangular for the current calculations, which cannot match even the linear increase in the *F-P* curve. It is obvious that using a non-linearly increasing *F-P* curve instead of a linear one will increase the mismatch, and decrease the efficiency.

Lastly, the author uses an *F-P* relationship with a piecewise linear loading region. The aim is to represent the sudden decreases in the force when a major stone fracture occurs (Figure 2.22).

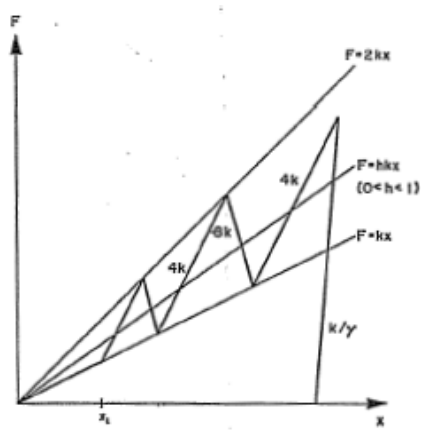

Figure 2.22 *F-P* relationship with piecewise linear loading region [19].

The *F-P* curve consists of linear segments that start and end on the straight lines $F=kx$ and $F=2kx$. The first segment is the $F=kx$ in the interval $0 \leq x \leq x_1$ and the remaining segments have slopes *4k, -8k, 4k, -8k,*…. When the displacement velocity becomes negative the unloading curve is linear with slope k/γ.

According to the results, in the specific example, the efficiency is a function of the amplitude of the incoming stress wave. The dimensionless parameter δ is used to represent the length x_1 of the first segment of the *F-P* curve and the incident stress wave amplitude σ_0 :

$$\delta = k \cdot x_1 / A \cdot \sigma_0 \ , \tag{28}$$

δ is closely connected with the number of segments of the *F-P* curve that are run through. For example, it can be shown that if δ>4, for any value of β, the first segment is not completely run through. This means that the efficiency becomes the same as for the case of a linear loading phase $F=kx$. So the efficiency depends on the incoming stress wave amplitude with a piece-wise linear *F-P* characteristic, unlike with the other types.

According to the author, the results also reveal that the efficiency results have the same general features when the *F-P* relationship is linear or piece-wise linear. Thus, linear approximations of the non-linear *F-P* relationships may lead to quite acceptable approximations of the efficiencies.

2.5 Stress Wave Interactions

As it was described in Section 2.4, the efficiency of the energy transfer during the impact of a certain stress waveform onto the bit-workpiece interface is dependent on the form and magnitude of the incident stress wave, *F-P* characteristic of the workpiece, and the properties of the drill bit.

However, when dealing with the efficiency of the whole drilling process, we also have to take the wave interactions in the drill bit into consideration, as they decide on the

forms of the stress waves to hit the workpiece. Depending on the wave interactions, some of the energy taken from the hammer may not even reach the workpiece, or some reflected by the workpiece may be sent back for another chance.

In order to consider all these effects, the efficiency of a drilling process is defined as the ratio of the work done on the workpiece to the initial kinetic energy of the hammer [20]. Thus, any wave interaction in the drill steel or between the parts of the percussive system can contribute to the efficiency. In this section of the literature review, studies and efficiency calculations taking wave interactions into account are going to be summarized.

Throughout this section, the compressive waves are assumed to be positive, the tensile waves are assumed to be negative.

Theory predicts that a compressive wave approaching a free boundary will be reflected as a tensile wave and *vice versa* without any loss of energy. A compressive wave approaching a rigid boundary or a sudden infinite increase in cross-sectional area will be reflected as a compressive wave. A tensile wave approaching an interface with a rigid body or one of infinite cross-sectional area will tend to part the two bodies and will, therefore, be reflected as a free face [21].

In 1961, Hawkes et al. [21] observes the travel of the waves in a hammer drilling system by using strain gauges. The drill steel does not have any cross-section changes.

In the measurements made without a workpiece (bit end free) the initial compressive wave is reflected as a tensile wave from the free end, and oscillates up and down the drill steel alternately in tension and compression until it is damped out. The records at Figure 2.23 are taken from a point that is 2.74 ft. from the shank end on a drum camera rotated at two different speeds.

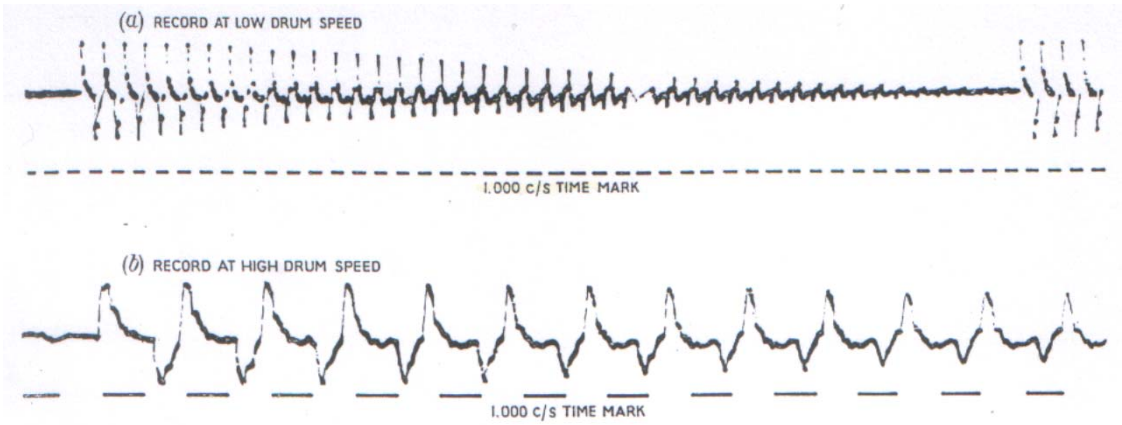

Figure 2.23 Complete waveforms in drill steel with bit end free [21].

In the measurements made by using a large steel block as a workpiece, the block acts nearly like a rigid body and the wave is reflected as a compressive wave from the bit end. When the shank end of the drill is totally free, the reflected wave is going to be reflected by the free end as a tensile wave. The first four waves for that case can be seen in Figure 2.24.

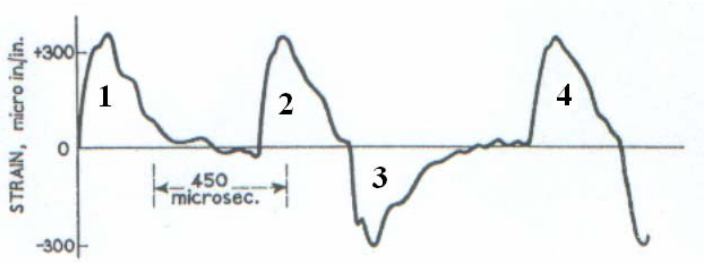

Figure 2.24 Initial wave and three reflections [21].

However, in the real case, the wave with number 2 in Figure 2.24 is not reflected by a totally free end because of the contact developed between the drill and the piston for the second time. Benefiting from the contact, the compressive wave can transmit some of its energy to the piston. The first three waves in that case can be seen in Figure 2.25.

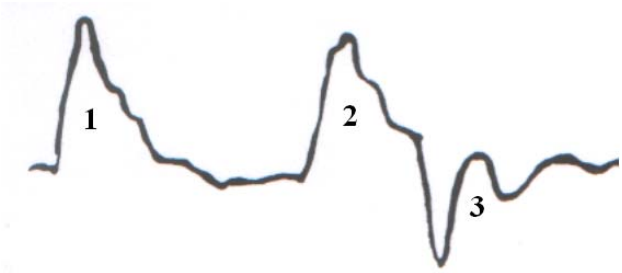

Figure 2.25 Initial wave and two reflections [21].

When sandstone is used as the workpiece, it is observed that the first part of the reflected wave is in tension (2-T in Figure 2.26) which then changes to compression (2-C in Figure 2.26).

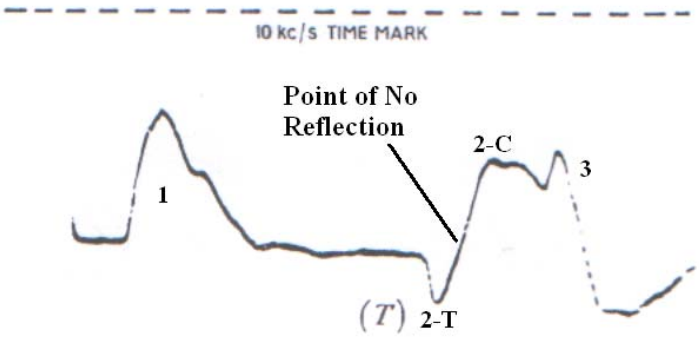

Figure 2.26 Initial wave and two reflections [21].

The reason for such a reflection is the impedance mismatch between the drill and the workpiece which was first described in Section 2.4:

At the instant the initial compression wave reaches the stone, the stone penetration resistance is very low. Thus, it behaves more like a free end, and reflects most of the incoming compressive wave as a tensile wave (2-T). As the end penetrates, however, the stone penetration resistance increases until the reflected wave comes back to zero. At that point, between tension and compression components of the reflected wave, all the energy of the incident compressive wave passes to the stone. That point is shown as the "Point of No Reflection" in Figure 2.26. As the drill steel moves further, however, the resistance builds up until all the energy in the initial wave is reflected as a compressive wave (2-C).

As a note, the small compression wave superimposed onto the end of the reflected wave, which is denoted by "3" in Figure 2.26, is the reflection of 2-T from the shank end.

The author emphasizes that the tensile portion of the first reflected wave is going to be reflected as a compressive wave from the shank end. This means, it has the possibility of making additional work on the stone. However, the remaining energy, in the form of a compressive wave, cannot be passed to the rock because it will always travel back down to the bit end as a tension wave, which is not capable of passing energy across an unbonded surface.

Hustrulid and Fairhurst [14] focus more on the reflection of the first reflected wave from the shank end: The second incident wave. Typically, the shape of the first reflected wave σ_r is shown in Figure 2.27.

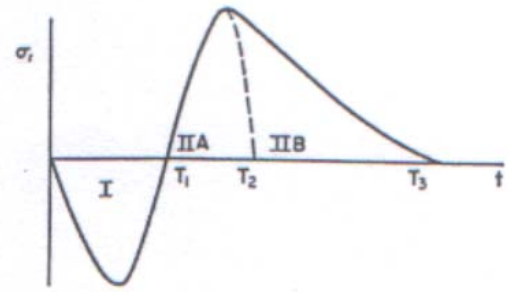

Figure 2.27 First reflected wave [14].

The wave consists of an initial tensile portion (I) and a following compressive tail (II), which is for convenience divided into two parts, IIA and IIB. The tensile portion (I) is going to be reflected from the shank end changing into a compressive wave. During reflection, Portion I produces a net displacement (u_a) of the end of the drill steel away from the piston. The compressive tail (II) produces a displacement of the end of the drill steel (u_b) back toward the piston.

If $u_b \geq u_a$ then the drill steel and piston reconnect. The second incident wave σ_{2i} at time T_2 (reconnection time) would then appear as shown below:

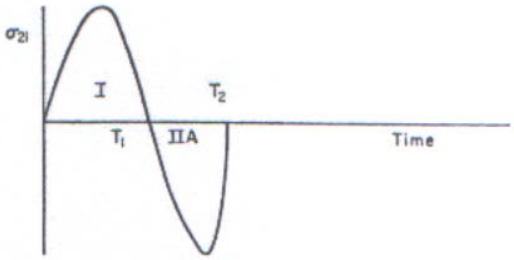

Figure 2.28 Second incident wave until time T_2 [14].

The form of the second incident wave now depends on the geometries and properties of the drill steel and piston. If the piston has the same cross-sectional area and material as the drill steel, all the energy of the drill steel starts to pass to the piston after time T_2. Then the drill bit-piston contact ends when that passed energy, which is in compressive wave form, turns back to the interface after changing sign at the free end of the piston.

If that happens at or after time T_3 (see Figure 2.27), the final form of the second incident wave is going to be the same with the one in Figure 2.28. If that happens before time T_3 (at time T_4), the energy from the bit cannot pass to the piston after time T_4, but it returns back to the drill bit as a tensile wave. In this case, the second incident wave takes the form in Figure 2.29.

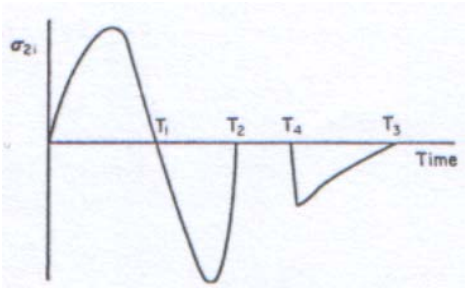

Figure 2.29 Second incident wave [14].

Generally, the piston does not have the same material and cross-section with the drill steel, so the second incident wave takes the general shape in Figure 2.30.

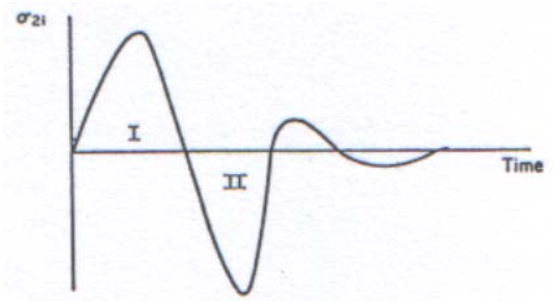

Figure 2.30 Second incident wave [14].

Knowing the material properties and dimensions of the piston and the bit, the amount of energy that is going to be trapped in the piston can be calculated for a given form of first reflected wave.

Lundberg [19] contributes the discussion by focusing on the energy transfer to the workpiece by the second incident wave. He states that, smaller energy is transferred to the workpiece by the second incident stress wave as the rock gets harder. This can be understood from the fact that the tensile part of the first reflected stress wave, and consequently the compressive part of the second incident stress wave shrinks as the rock stiffens.

Stress wave reflections and transmissions do not take place only between the different bodies of the system, any characteristic impedance change in the model results in wave reflections.

In 1982, Lundberg [22] writes a computer code to make stress wave interaction calculations according to 1-D stress wave theory easier. In the method used by the author, the elastic bodies in the drilling system are divided into uniform segments with

equal lengths (if the elastic wave speed is the same for all bodies). Then the stress value at each segment is calculated according to:

$$s(x,t) = p(x,t) + n(x,t) \ , \tag{29}$$

where the functions p and n represent elastic waves traveling in positive and negative directions on the segment, respectively, and s gives the resulting stress. x represents the segment being considered, t denotes the time. The functions s, p and n are constant in each uniform segment, since the analysis is simplified by considering only the discrete times $t = 0, h, 2h, \ldots$ where h is the time required for the elastic wave to travel along one segment.

In order to determine p and n at any segment at time $t+h$, known p and n values from time t are used. First, based on the characteristic impedance ratios, reflection and transmission coefficients are determined for the interfaces between the segments. Then the transmissions and reflections of the old p's and n's are calculated to obtain new p's and n's.

By means of reflection and transmission coefficients, all the cross-sections between segments in the model, including the one between the bit and the workpiece, are treated as bonded. If tensile forces develop at a cross-section between separate bodies, the simulation terminates.

The boundary conditions are also represented in terms of reflection coefficients. Particularly, for a free end, reflection coefficient is -1, and for a fixed end, reflection coefficient is 1. The determination of the boundary condition for the bit-workpiece interface is based on an approximation of the bilinear *F-P* relationship.

The author uses the code to evaluate the efficiency of different drill bit head designs (seen in Figure 2.31). Only the first incident wave is considered, and the typical waveform of a shank piston is selected. The results reveal that there is a strong effect of bit head mass on the efficiency, while the shape has a weak effect.

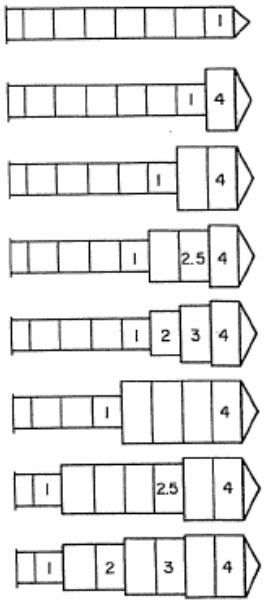

Figure 2.31 Drill bit heads used in the simulations [22].

In 1985, Lundberg [23] improves the code in order to include repeated separations and renewed contacts between the parts. He uses the code to solve a real hammer drilling system: Atlas Copco COP 1038 HD. The system consists of a hammer, anvil and a long drill bit. Only the first incident wave is considered: the waves reflected by the workpiece are deleted after reaching the drill rod. As a result of the application, the author obtains the efficiency of the drilling process vs. the parameter β (Figure 2.32).

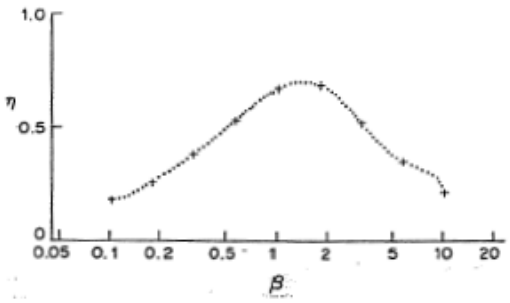

Figure 2.32 Efficiency η vs. β for Atlas Copco COP 1038 HD [23].

The parameter β is a dimensionless parameter representing the stiffness of the rock, and it is given by:

$$\beta = k / k' \ , \tag{30}$$

where k is the slope of the loading phase of the *F-P* relationship, and k' represents the stiffness of a part of the drill rod with the length of the incident wave:

$$k' = A \cdot E / 2 \cdot L_H \ . \tag{31}$$

In Equation 31, A, E and L_H represent the area, elastic modulus and length of the hammer, respectively. As a result, $\beta << 1$ can be considered to represent soft rock and $\beta >> 1$ hard rock.

In 1987, Lundberg [24] uses the code to see the effects of extension rods on efficiency. Extension rods are used in hammer drilling of holes to greater depth than the length of a single rod. Generally, the extension rods are threaded at their ends and are screwed

into cylindrical coupling sleeves in end-to-end contact. These sleeves create section changes in the drill rod.

When the waves in the drill encounter the section changes, they are partially reflected and transmitted. This modifies the energy and the form of the waves, and may also create tensile stresses in certain parts of the drill. The reflections due to the section changes at the sleeves also affect the relationship between the hammer, anvil and the drill bit.

The author states that the incident wave on the workpiece becomes longer and smoother and has lower amplitude than it would have otherwise. It also carries less energy, as the joints are going to disperse the stress wave energy into the various parts of the drill bit. Although it cannot be modeled in the computer simulation, loss of energy due to friction and slip within the joints is another contribution to the reduction of energy carried by the stress waves.

In the computer model, the author represents the joints as sudden cross-section changes. The model can be seen in Figure 2.33.

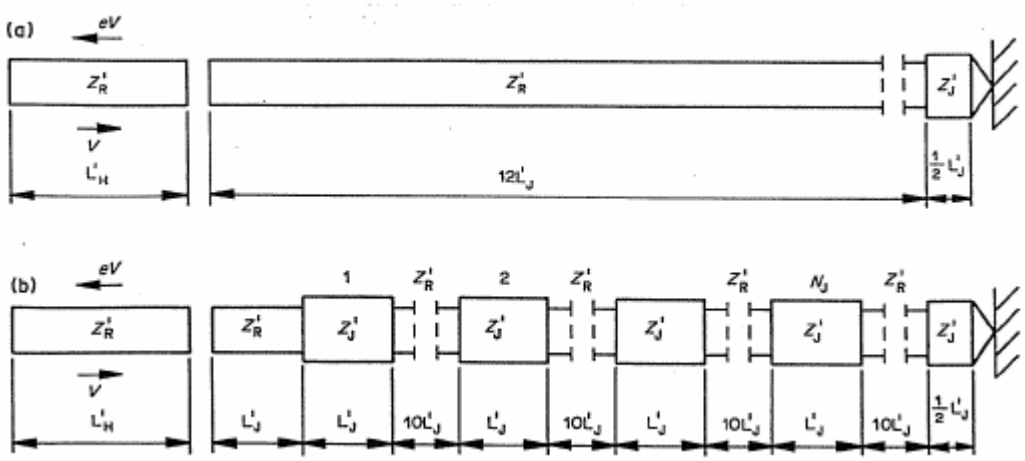

Figure 2.33 Percussive drill models. (a) Uniform rod configuration. (b) Extension rod configuration [24].

The model is dependent on two variables: the number of the joints: N_j, and the ratio of the length of a joint to the length of the hammer: λ_j. The efficiency of the drilling process for varying β (given in Equation 30) is calculated depending on these two parameters. The results can be seen in Figure 2.34.

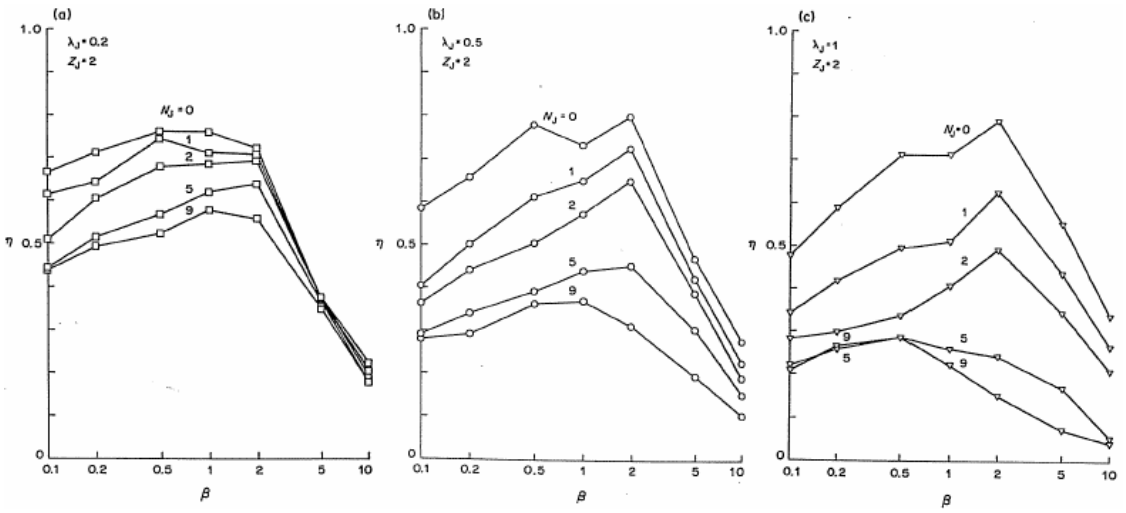

Figure 2.34 Efficiency η vs. β for different N_j and λ_j values [24].

As can be seen in Figure 2.34, the efficiency first increases and then decreases with β, as it also does in Figure 2.32. According to the author, the efficiency is low for soft and hard workpieces, since the incident wave is reflected mainly as a tensile wave in the former case, while it is reflected mainly as a compressive wave in the letter case.

It is also evident from Figure 2.34 that the main effect of adding joints is to decrease the efficiency, as expected. This decrease is more severe for large values of the joint-to-hammer length ratio λ_j than for low values.

Another effect of the joints is the removal of the maximum for η to lower values of β. According to the author, this reveals that the longer incident stress waves created by the effects of joints are more appropriate for softer rocks.

In 2000, Chiang et al. [25] propose an alternative 1-D method to the one used by Lundberg and his co-workers [22, 23, 24]. The authors model the impact between solid

bodies in terms of the impulse-momentum principle. The 1-D elastic bodies are discretized into nodes and equal size elements, and the corresponding impulse-momentum equations are applied iteratively at each node and at each element assuming constant wave speed. Modeling of the bit interaction with the workpiece is done by the same scheme used by Lundberg. The authors believe that this method makes it easier to study the interaction of many bodies during impact under a variety of boundary conditions.

Chiang [2] compares the results with the Finite Element Method (FEM). A 1-D model composed of truss elements, and a three-dimensional (3-D) model with 8-node brick elements are used for comparison. The results show a good agreement, as can be seen in Figure 2.35.

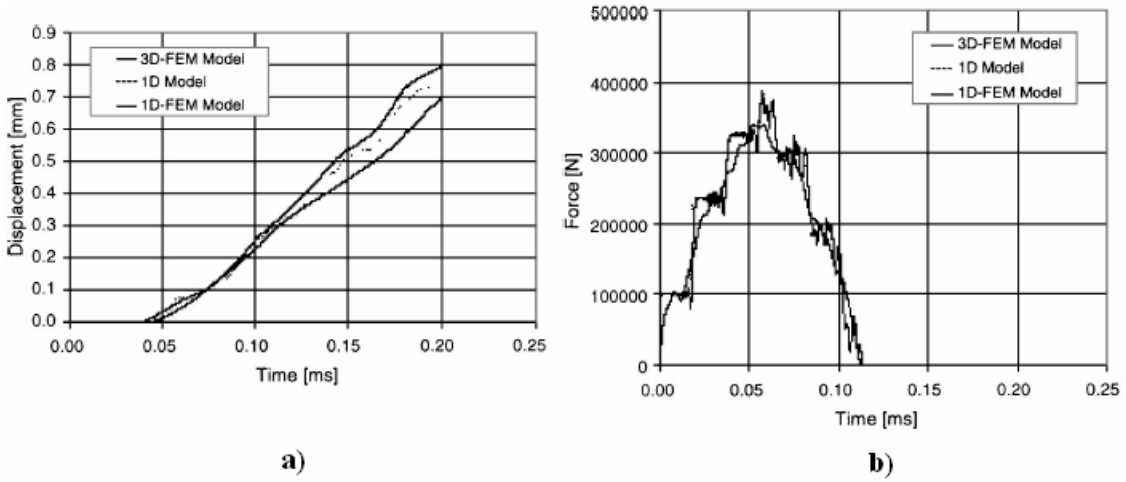

Figure 2.35 (a) Bit penetration vs. time. (b) Force vs. time at piston-bit interface [2].

The proposed method is used to analyze down-the-hole drilling process on different kinds of rock, which are differentiated by the *F-P* curves. The rocks modeled are

mortar, andesite and granite from the softer to the harder. According to the results, the remained energy in the piston after the hit is independent of rock being impacted. Only for the case of rigid rock, there is significantly more energy remained, as can be seen in Figure 2.36. According to the author, it reveals that the piston separates from the drill bit before the rock can reflect any stress wave back into the piston [25].

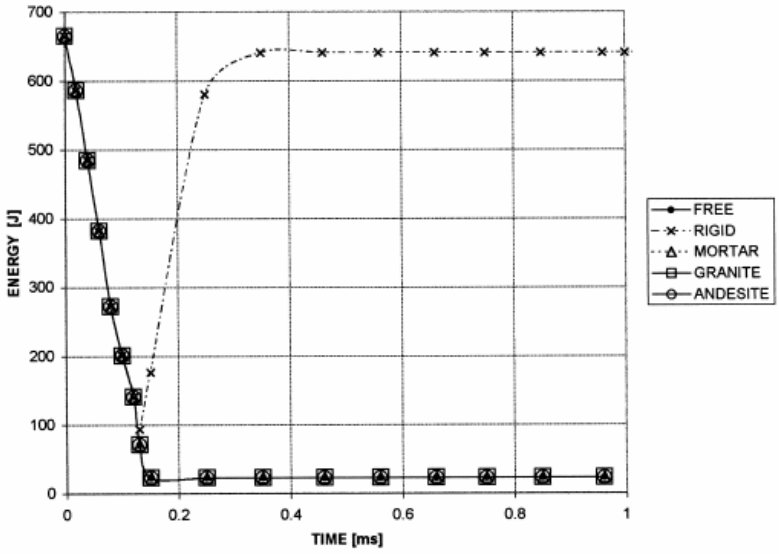

Figure 2.36 Energy time history of the piston for DTH drilling [25].

This can be explained as follows: It was mentioned before that when a rigid body is used as the workpiece, the first reflected wave is a compressive wave, which can transmit energy to the piston. However, when rock is used, the first reflected wave has a tensile leading portion [21]. The tensile portion, when reached the piston interface, pulls the end of the bit away from the piston [14]. If the following compressive tail cannot maintain the contact again, no energy can be transmitted to the piston, which is the case for the three rock types in Figure 2.36.

The author also notices that for different rock types, the energy absorbed by the rock is similar, and is a large portion of the initial piston energy for DTH drilling as can be seen in Figure 2.37. The main difference is the time that the rock takes to absorb the energy, as well as the penetration depth [25].

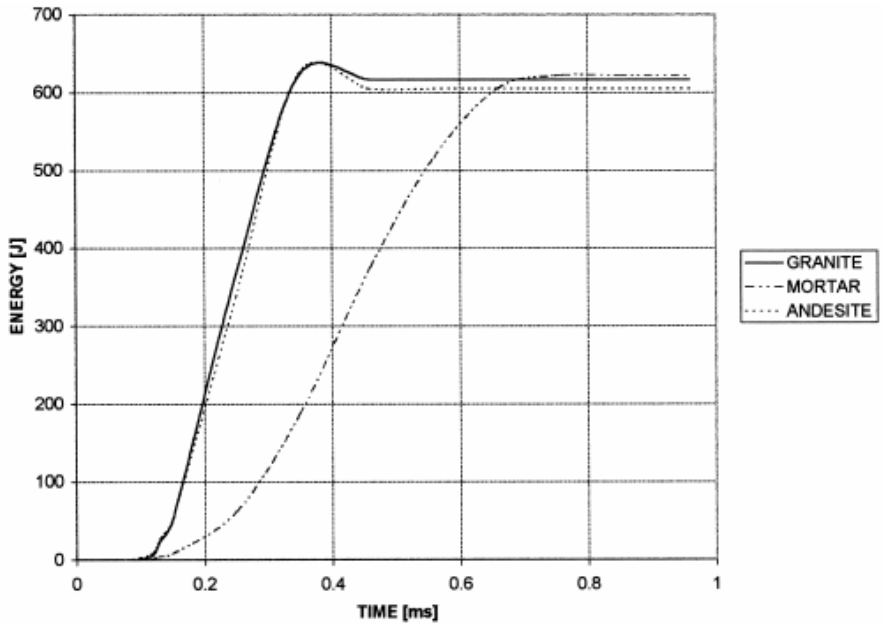

Figure 2.37 Rock energy absorption in DTH drilling [25].

According to Lundberg, the increased efficiency in DTH drilling with respect to hammer drilling is due to the short drill steel. The second incident wave hits the workpiece immediately after the first incident wave, and causes additional work to be performed on the rock [3].

In 2001, Lundberg et al. [3] check the validity of 1-D stress wave assumption used in percussive drilling calculations by the help of FEM for three types of percussive

drilling (DTH, churn and hammer drilling). The authors use hollow drill rods, in which the 3-D effects are expected to be more effective.

1-D results are obtained from exact solutions (given in Section 2.4), 3-D results are obtained from an axisymmetric finite element (FE) model. In the FE model, the hammer is not included, but the initial stress wave is created by a pressure application to the bit from the shank end.

Furthermore, the *F-P* characteristic of the workpiece is considered by means of elastic springs. Only the loading phase of the process is simulated, and the energy loss at the unloading phase of the process is calculated manually benefiting from Equation 5. (see Figure 2.11)

According to the results, the relative difference between the efficiencies obtained from 1-D and 3-D analyses is 4% for hammer drilling, 1% for DTH drilling and negligible in churn drilling. According to the author, the 3-D effects which are more effective in hammer drilling than other processes tend to decrease the efficiency of the drilling process.

In 2006, Lundberg et al. [26] models churn drilling with axisymmetric FEM. The model can be seen in Figure 2.38.

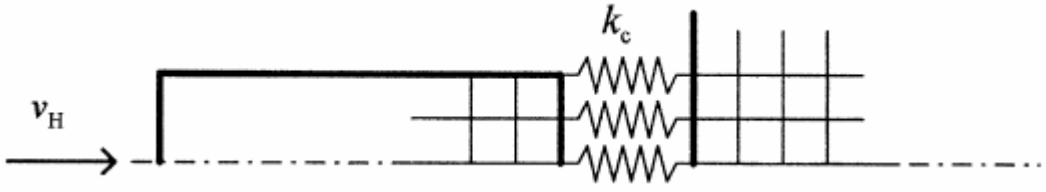

Figure 2.38 3-D model of churn drilling [26].

Unlike the previous model [3], the springs are not elastic, but perfectly inelastic. So the unloading phase can also be modeled with the springs. However, since it is numerically impossible to use the unloading parameter $\gamma = 0$, very small values are used instead. (see Figure 2.11)

As indicated in Figure 2.38, the springs are attached to the nodes. Because of this, at the end of the unloading phase, the unloading springs have to be disconnected one by one at the instants when the load tends to change from compression to tension. The springs are also attached to the rock nodes.

The rock is modeled as a half space with a linear elastic or rigid material model. The author observes the effect of the elastic response of the rock by switching between rigid and non-rigid models of the rock.

2.6 Studies on Hand-type Hammer Drilling

For the fastening of anchors, bolts and dowels, or any other construction application, holes have to be drilled into rock, concrete or other hard brittle materials. In order to produce a hole, a rotary hammer drill machine creates stress waves which are transmitted through a special drill bit to the drill head [27].

In the drill head, the wave is transmitted from the steel to the tungsten carbide insert by a soldering layer. This junction is stressed very strongly because materials with different mechanical impedances are involved [27].

In 1992, Stöck and Shad [27] predicts analytically the displacements and stresses in a drill head with tungsten carbide insert. The authors simplify the drill head geometry

for convenience. Typical drill head geometry and its simplified form are seen in Figure 2.39.

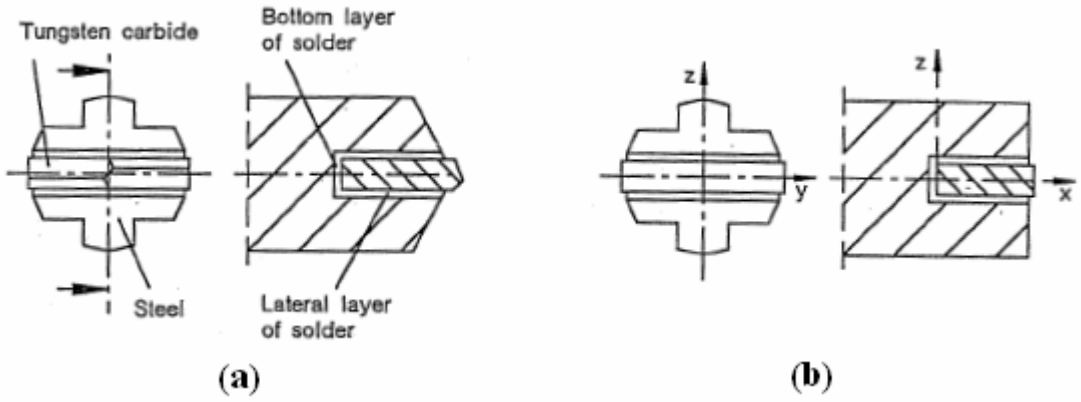

Figure 2.39 (a) Typical drill head, (b) Simplified drill head geometry [27].

In Figure 2.39, the longitudinal direction of the drill is the *x*-direction. The authors want to find the displacement and stress distribution at the drill head on the *x*-*z* plane (seen in Figure 2.39b), which is assumed to remain plane during deformation. Figure 2.39b also shows the origin of the coordinate axes.

As the main load of the stress wave is in the *x*-direction, the displacements and strains in *z* direction are neglected. The stresses in z and y directions are also omitted, and uniaxial stress state is assumed. Moreover, the displacement in the *x*-direction is assumed to be not dependent on *z*.

Static solution is taken by assuming that the sum of the forces on the steel and tungsten carbide at x=0 is equal to the force calculated from the maximum amplitude of the

incident stress wave. Besides, the displacement at the rightmost surface of the tungsten carbide is assumed to be zero (see Figure 2.39b).

As a result of the calculations, the displacements and stresses in the *x*-direction with respect to *x* are calculated for steel and carbide, and the shear stresses τ_{zx} with respect to *x* are calculated for the lateral layer of solder. The lateral layer of the solder is indicated in Figure 2.39a. The stress results can be seen in Figure 2.40.

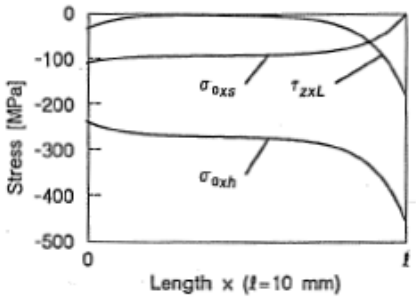

Figure 2.40 Stress distribution in the drill head with respect to *x*. $\sigma_{0xs}(x)$ is the mean stress in the steel, $\sigma_{0xh}(x)$ is the mean stress in tungsten carbide and $\tau_{zxL}(x)$ is the shear stress in the lateral layer of solder, respectively.

The displacement results are compared measurements. The experimental displacement results can be seen in Figure 2.41.

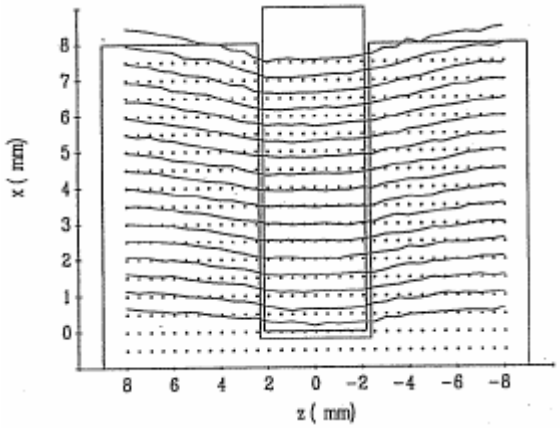

Figure 2.41 Measured displacements magnified by a factor of 500. The deformed configuration (—), and the unloaded configuration (with dots).

As can be seen in Figure 2.41, for tungsten carbide, the displacements are not changing extensively with *z*. This corresponds with the assumption made in the calculations, so a very good agreement occurs between the calculated and measured mean displacements in the tungsten carbide (see Figure 2.42).

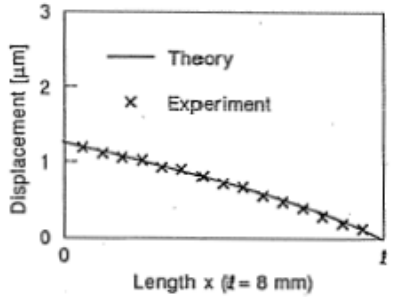

Figure 2.42 Theoretical and experimental mean displacements of tungsten carbide with respect to *x* [27].

However, the *z*-dependency in the measured displacements of the steel is obvious (see Figure 2.41). As a result, the calculated and measured mean displacements ($w_{0xs}(x)$) do not coincide well, as can be seen in Figure 2.43. When the mean displacement of the steel at $z = \pm a_s$ ($w_{xs}(x, a_s)$) is calculated, where a_s is the quarter steel thickness, the results coincide better. (see Figure 2.43)

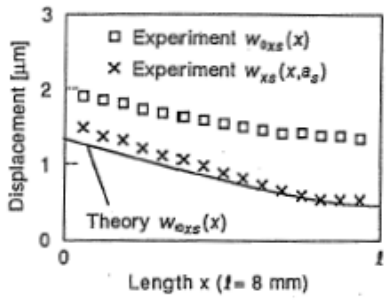

Figure 2.43 Theoretical and experimental mean displacements of steel as a function of *x* [27].

In 1988, Muro [6] conducts experiments to clarify the relations between rock characteristics, drill bit diameter and drilling rate. He uses a hand-type hammer drill machine applying 2800 blows on the drill bit with the blow energy of 22.5 N.m/blow. Drill bits with 505 mm length and six different diameters, 16, 19, 22, 25, 28 and 32 mm are used.

The tests made with different kinds of rock revealed that the drilling rate decreases as the diameter of the drill increases (see Figure 2.44).

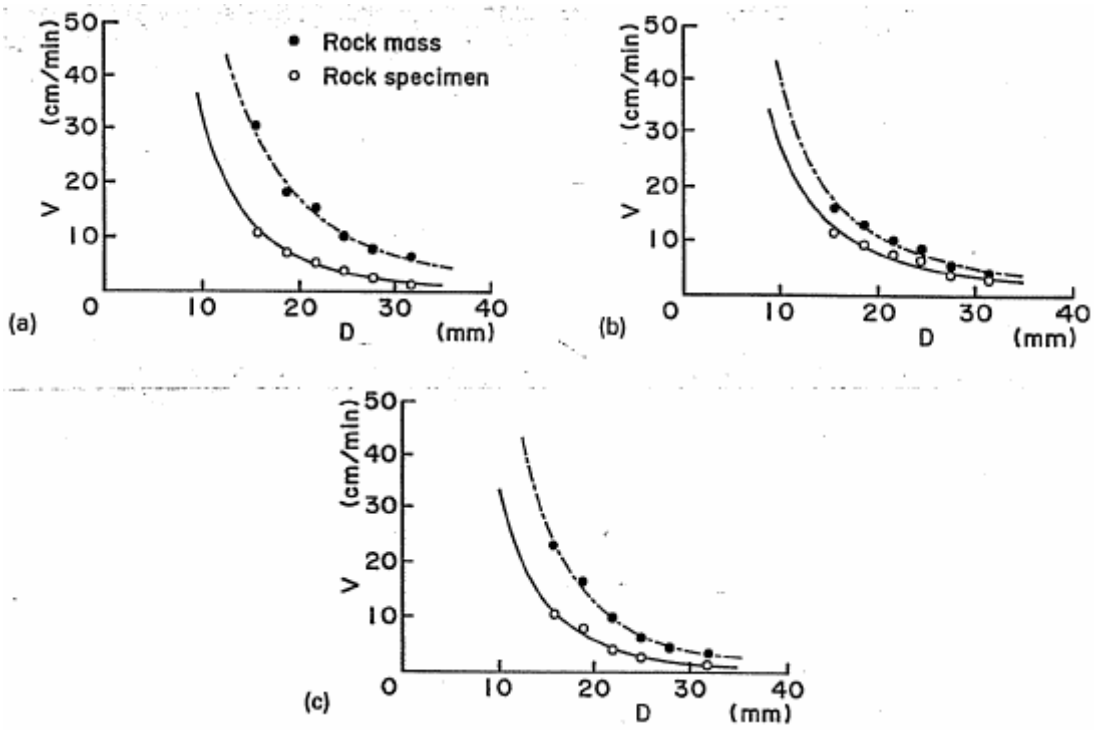

Figure 2.44 Relations between drilling rate V and diameter of the drill bit D. In (a), (b) and (c), the rock types are different [6].

According to the results in Figure 2.44, the author derives that the drilling rate changes with the drill bit diameter according to the following relationship:

$$V_F = C \cdot D^{-1.82} \ , \tag{32}$$

where C is a constant determined by other parameters of drilling process.

CHAPTER 3

EFFICIENCY OF DRILLING PROCESS WITH RESPECT TO DRILL BIT DIMENSIONS

3.1 Introduction

For the largest and deepest holes that can be drilled with a hand-type hammer drilling machine, SDS-max drill shanks are used [28]. These shanks have standard dimensions given in Figure 3.1. Drill bits using SDS-max shanks are used to drill holes with diameters from 12 mm to 52 mm, and with lengths up to 1 m. While the shank is constant, the diameter and the length of the drill rod change according to the hole dimensions.

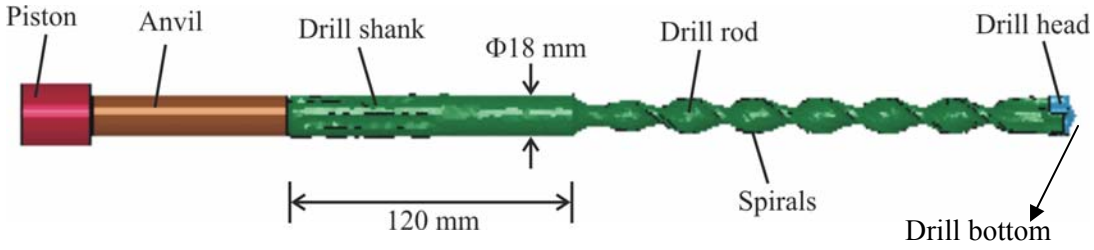

Figure 3.1 The parts of a hammer drilling system.

The drill shank diameter being Φ18 mm, drill bits with a larger diameter have a cross-section increase, and the bits with a smaller diameter have a cross-section reduction between the drill shank and the drill rod.

The axial compressive stress wave created by the piston impact, which is going to be called the initial stress wave, enters the drill bit from the drill shank. During its travel in the bit, all the geometry and material discontinuities divide it into axial transmitted and reflected portions. The workpiece, too, is going to reflect some portion of the stress waves. Consequently, the drill bit creates series of axial stress waves to hit the workpiece, which are going to be called the incident stress waves.

The properties of the incident stress waves and their application on the workpiece determine the efficiency of the drilling process. Besides, production of these waves and their effect on the workpiece are regulated by the dimensions of the drill rod and the characteristic of the workpiece.

In this chapter, efficiency of the drilling process is evaluated in regard to the length and diameter of the drill rod and the characteristic of the workpiece.

Axisymmetric dynamic explicit finite element (FE) simulations performed with the commercial code LS-DYNA are used for the evaluation. Basic impact mechanics principles and equations that are explained in Appendix A are used for verification and interpretation of the simulation results, whenever possible.

In order to obtain an axisymmetric model of hammer drilling, several details of the model like the clamping grooves in the shank, spirals, and the special shape of the drill head are neglected, as can be seen in Figure 3.2.

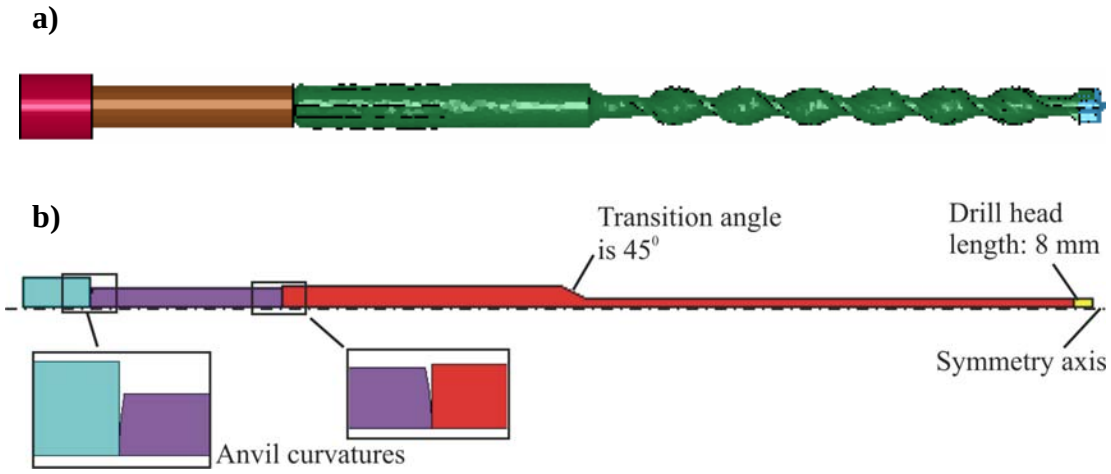

Figure 3.2 3-D (a) and axisymmetric (b) models of piston, anvil and drill bit.

Throughout the study, it is assumed that the effects of the neglected details of the drill bit and the rotational motion are minor. Besides, the stress waves are assumed to die out until the next piston hit, so, only a single piston hit is simulated.

For the characterization of the workpiece, an inelastic spring with a bilinear force-displacement relationship is used (see Figure 3.3).

In Figure 3.3, the slope of the loading paths A-B and B-D is K, while the slope of the unloading or repeated loading paths C-B and E-D is k, which is given by:

$$k = 50 \cdot K \,. \tag{3.1}$$

Throughout the studies presented in this chapter, the parameter K is varied between $2\text{x}10^4$ N/mm and $6\text{x}10^8$ N/mm in order to account for soft and stiff workpieces.

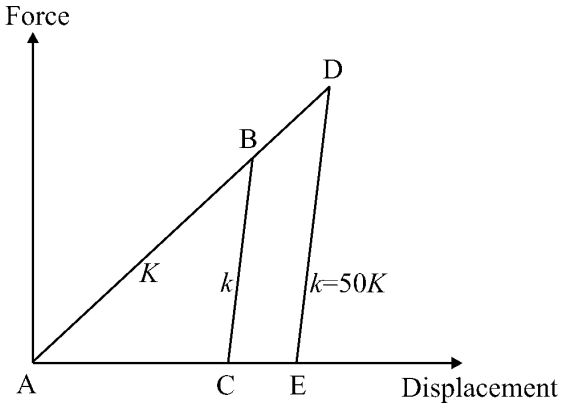

Figure 3.3 Force-penetration characteristic of the workpiece.

In case of a force reduction during force application along line AB, the unloading will take place along line BC. In case of a second force increase (*e.g.* an increase in incoming stress wave), the force at point B must be exceeded for further plastic deformation take place.

Throughout the chapter, (+) denotes compressive stress, (-) denotes tensile stress, for convenience. Conventionally, the workpiece is called as rock. Conventionally again, the stiffness of the rock is called the rock hardness, and the rock is called to be soft, medium and hard as the stiffness K increases.

3.2 Initial Stress Wave

The initial stress wave, which is denoted by $\sigma_{initial}$ is the input given to the drill bit for the creation of incident axial stress wave series. In this section, the FEM results for $\sigma_{initial}$ are compared with the theoretical calculations. Appendix B can be seen for more comments.

Dimensions of the piston and the anvil are given in Figure 3.4.

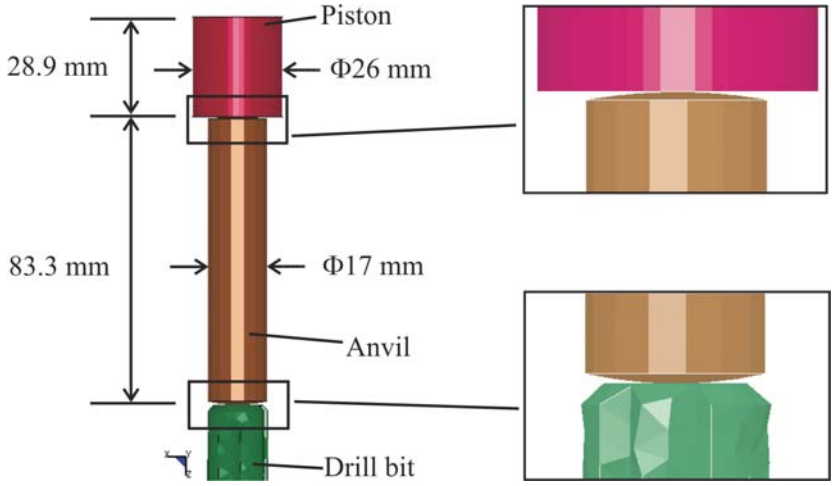

Figure 3.4 The piston, anvil and the drill bit.

As it can be seen in Figure 3.4, the anvil has curvatures at both ends, while the piston and the top of the drill bit do not have. For convenience, the curvatures of the anvil are not taken into consideration in the theoretical calculations. The calculated and simulated $\sigma_{initial}$ waveforms are given in Figure 3.5.

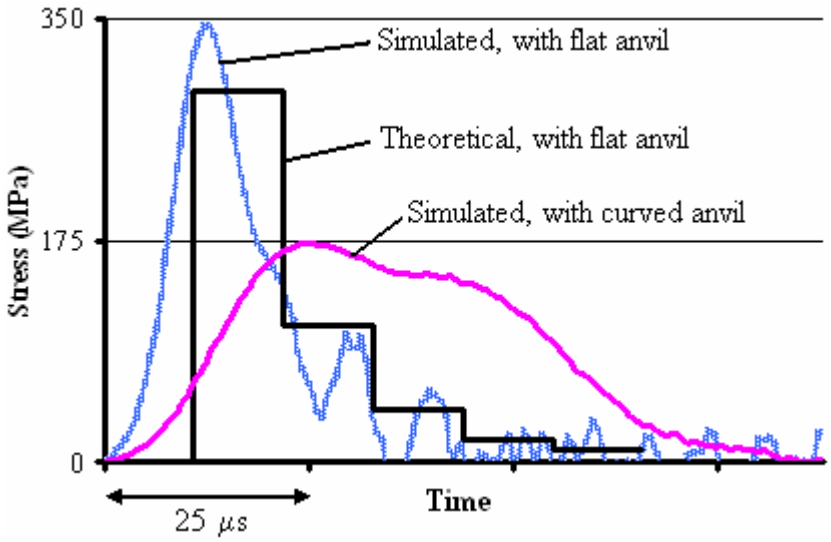

Figure 3.5 Theoretical and simulated $\sigma_{initial}$ waveforms.

The theoretical and simulated results with flat anvil are similar except fluctuations resulting from the penalty contact algorithm used by LS-DYNA. When the curvatures are included in the FE model, the magnitude of $\sigma_{initial}$ reduces, while the width increases.

The curvatures also cause some of the energy turn back to the piston and the anvil and be trapped there. As a result, the waveform in case of a curved anvil holds slightly less energy than the flat anvil case: Nearly all of the initial piston energy is transmitted to the bit with a flat anvil, while %95 is transmitted with curvatures.

Although only the results are given here, the production of $\sigma_{initial}$, and the effect of the curvatures on it are explained in detail in Appendix B.

3.3 First Incident Waves

After entering the drill bit, the first obstacle on the way of $\sigma_{initial}$ is the cross-section change (if there is).

In case of a cross-section reduction (Figure 3.6a), a portion of $\sigma_{initial}$ is transmitted to the drill rod as $\sigma_{i11}>\sigma_{initial}$, while another portion is reflected as a tensile wave (Figure 3.6b). The reflected tensile wave is going to hit the free end of the shank and turn back to the cross-section reduction as a compressive wave (Figure 3.6c). That compressive wave, when hits the cross-section reduction, generates $\sigma_{i12}<\sigma_{i11}$ to follow σ_{i11} and a tensile reflected wave (Figure 3.6d). The tensile wave, in turn, is going to create the third peak to follow σ_{i11} and σ_{i12}.

The consequence of that loop is successive compressive stress waves σ_{i11}, σ_{i12}, σ_{i13},… with decreasing amplitudes. These waves are the first waves to hit the rock, called the first incident stress waves, and denoted by σ_1.

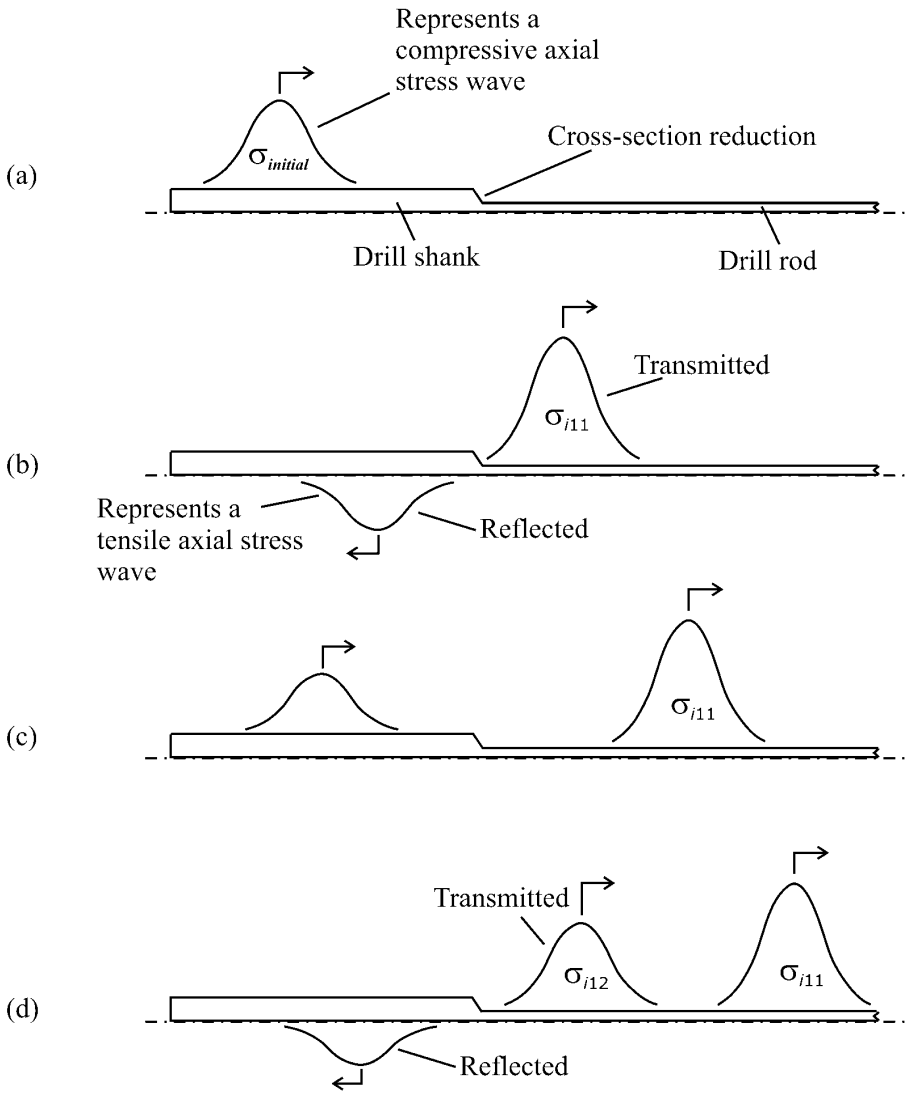

Figure 3.6 The conversion of $\sigma_{initial}$ to σ_1.

In Figure 3.7, the waveforms obtained for σ_1 from theory and FEM with flat and curved anvil are compared.

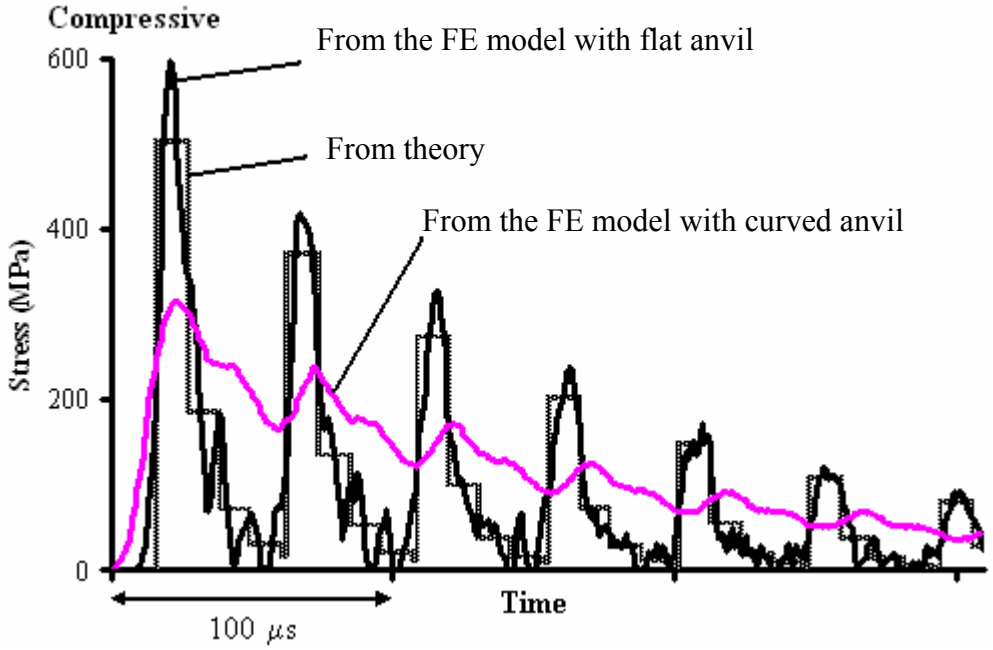

Figure 3.7 σ_1 for 7 mm drill rod diameter.

As can be seen in Figure 3.7, the theoretical and simulated results are parallel except the overshoots due to the fluctuations investigated in Appendix B.

In the model with the curved anvil, because of the differences in $\sigma_{initial}$, the peaks of σ_1 are smaller in magnitude, but larger in width. That also leads the intersection of the peaks and creates a continuous σ_1.

According to the theory, in case of cross-section reduction, the magnitudes of the members of σ_1 decrease with the increasing diameter of the drill rod. That is approved

by FEM as it can be seen in Figure 3.8, when the waveforms in Φ7 mm, Φ11 mm and Φ15 mm drill rods are compared.

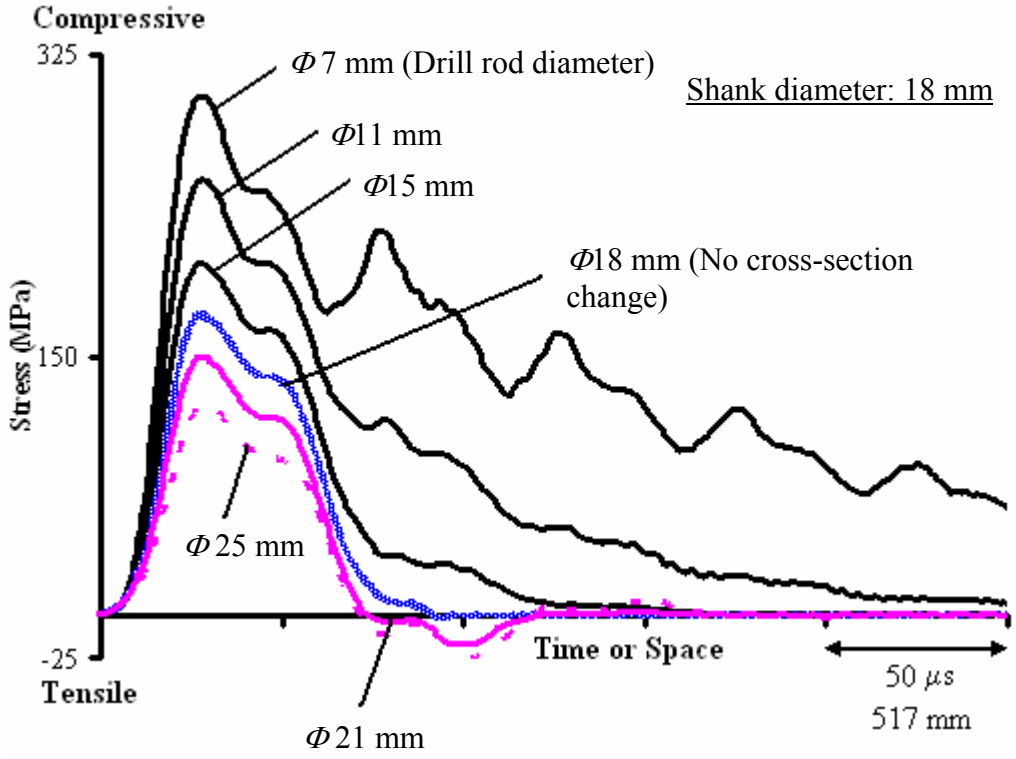

Figure 3.8 σ_1 with respect to drill rod diameter.

In case of cross-section increase, it can be calculated that σ_1 is going to have a tensile portion following the compressive one. The compressive part shrinks, and the tensile part enlarges when the diameter of the rod increases. This is approved by FEM as it can be seen in Figure 3.8, when the waveforms in Φ21 mm, Φ25 mm drill rods are compared.

It is obvious that, all the waveforms seen in Figure 3.8 hold the same amount of energy, which is equal to the energy of the initial stress wave. However, they apply that energy on the rock in different ways:

In case of a cross-section reduction, the energy is applied by successive stress peaks in a longer duration. The width of σ_1 increases with the decreasing drill rod diameter. In case of a cross-section increase, some of the energy cannot be applied on the rock, being converted to a tensile stress wave. The amount of wasted energy increases with the drill rod diameter.

3.4 Efficiency of the First Incident Waves

When incident on rock, a certain portion of the energy carried by σ_1 is transmitted to the rock and some portion is reflected back in terms of tensile or compressive stress waves. The efficiency of σ_1, which is denoted by η_1, is defined as the ratio of energy transmitted to the rock by σ_1 to the initial piston energy.

For increased efficiency, the amount of reflected energy must be minimized. The factors affecting the amount and form of the reflection are the rock stiffness and the incident stress waveform (*i.e.* the drill rod diameter).

As explained in section 2.4, the theory predicts that, the impedance of the rod and the penetration impedance of the workpiece behaving like an inelastic spring cannot match at all times during the wave impact on the rock, so a portion of the incident wave is reflected back to the workpiece. It was also revealed that, for a workpiece behaving like an inelastic spring, the reflection of a compressive stress wave is a tensile-and-then-compressive wave.

In Figure 3.9, reflected waveforms are given for varying K in a drill bit with a 7 mm drill rod diameter (Φ7 mm drill bit).

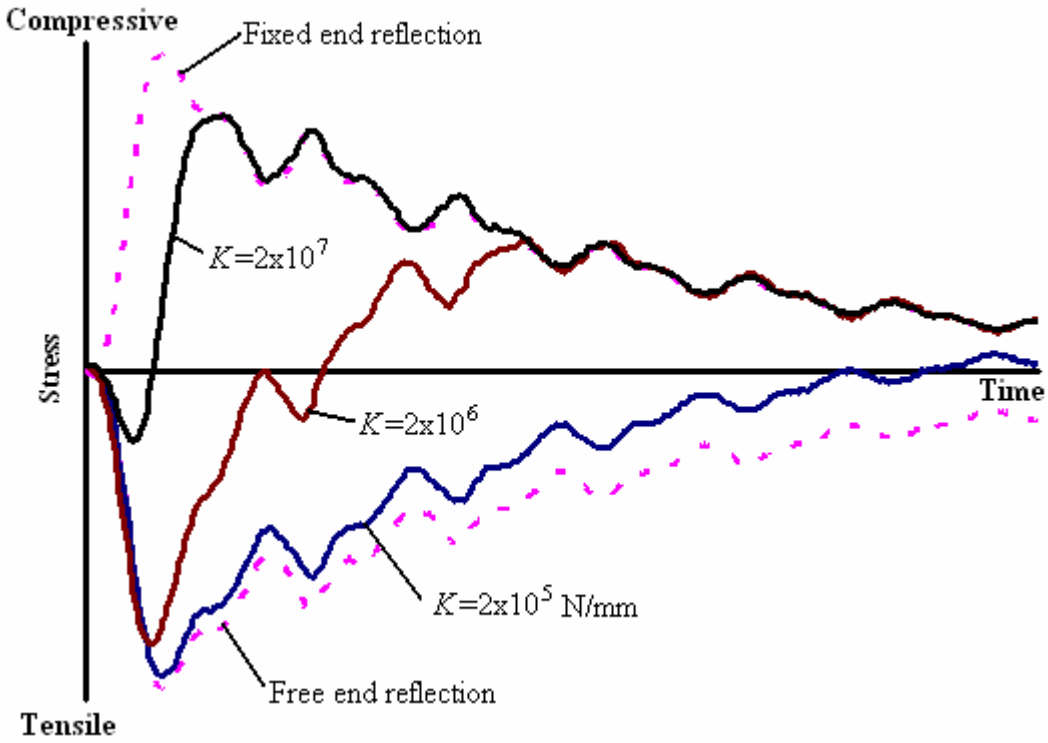

Figure 3.9 Reflection of σ_1 with respect to K in a Φ7 mm drill bit.

If the rock has infinite or zero stiffness (fixed-end or free-end reflection), the entire incident energy is going to be reflected back to the drill bit in compressive or tensile stress waveform, respectively. Those two cases are indicated by dashed lines in Figure 3.9.

In moderate cases, the ratio of the compressive portion to the tensile portion increases with rock hardness. That is, the wave is reflected mostly as a tensile wave for soft

rock, as a compressive wave for hard rock. The efficiency of energy transmission is low for both cases. Increased transmission can be reached in case of medium rock hardness.

However, the definitions of hard, soft and medium hardness differ with respect to drill rod diameter. A thicker drill bit applies all of the impact energy and force to the rock suddenly, while a thinner one applies it in a longer time. Therefore, a hard rock for a thinner drill bit may behave like a soft rock for a thicker drill bit. This phenomenon can be seen in Figure 3.10.

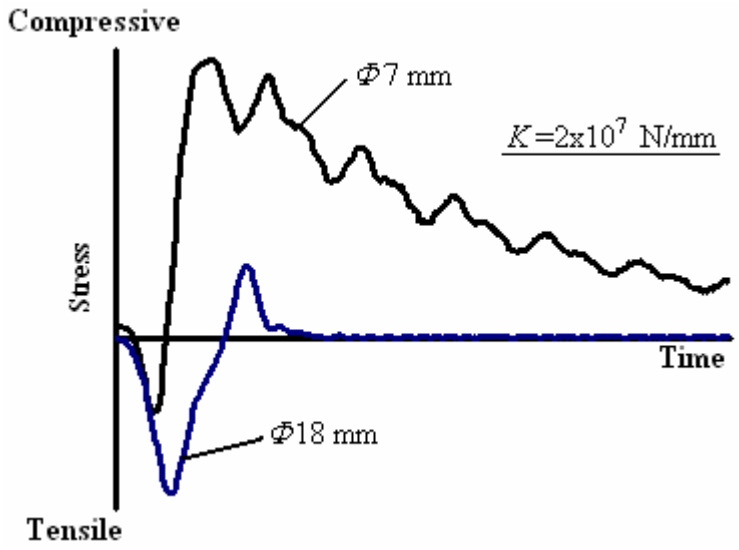

Figure 3.10 Reflection of σ_1 with respect to diameter (K=2x10^7 N/mm).

As can be seen in Figure 3.10, for K=2x10^7 N/mm, the reflected waveform is mostly compressive for a Φ7 mm drill bit (hard rock case), while it is mostly tensile for a Φ18 mm drill bit (soft rock case).

In Figure 3.11, η_1 is given with respect to drill rod diameter and rock hardness.

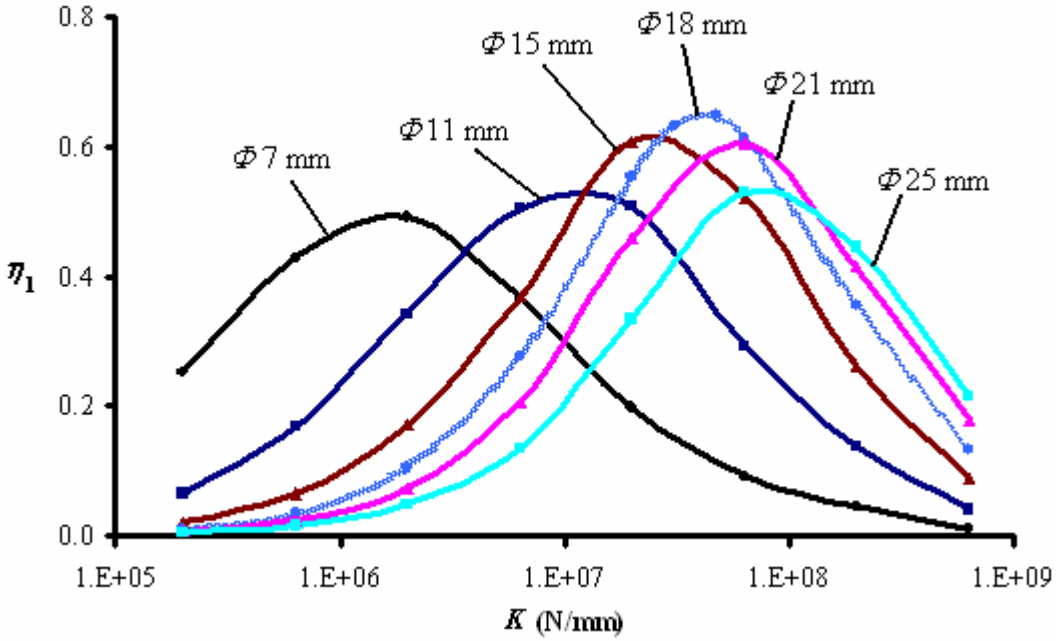

Figure 3.11 η_1 vs. K for varying drill rod diameter.

As can be seen in Figure 3.11, for each drill rod diameter, η_1 is low for soft and hard rock, while it is higher for medium rock. As explained before, the ranges of hard, soft and medium rock vary with respect to the drill rod diameter. It can be concluded as a general rule that, considering σ_1, thinner drill bits are more efficient in softer rocks.

3.5 Successive Incident Waves

The reflected portion of σ_1, which is moving towards the shank end of the drill bit in the form of a tensile-and-then-compressive wave, is going to be reflected back to the rock by the cross-section change (if there is) and by the free end of the drill bit. That

reflection is going to create the second incident waves on the rock, which are denoted by σ_2.

In case of a uniform cross-section drill bit, the free end reflection simply changes the sign of the incoming wave series (Figure 3.13a).

In case of a cross-section reduction, first, a simpler case, in which the incoming wave is fully compressive or tensile, is going to be investigated. Then, the real case is going to be interpreted using the results.

If the reflected portion of σ_1 is assumed to be fully compressive, σ_2 is a compressive-and-then-tensile wave, as described in Figure 3.12.

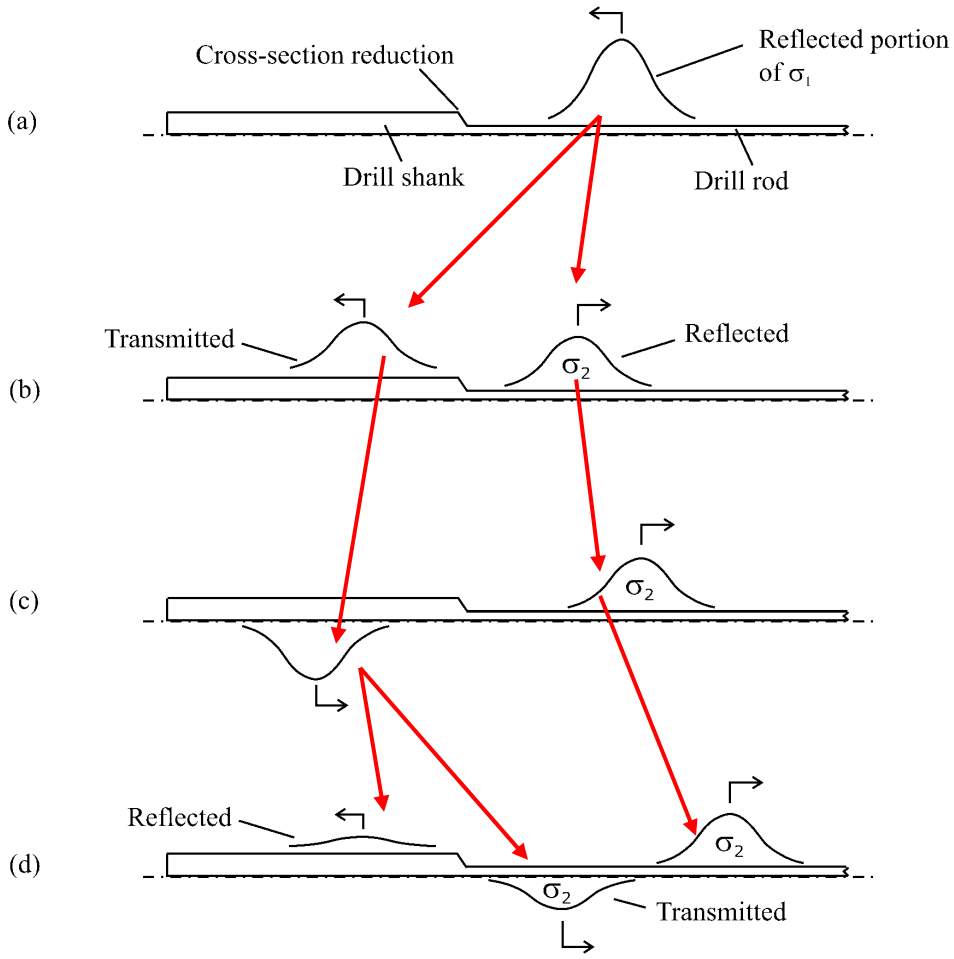

Figure 3.12 The conversion of the reflected portion of σ_1 to σ_2.

The reflected portion of σ_1 hits the cross-section reduction and is separated into reflected and transmitted portions (Figure 3.12a and 3.12b). The sign and moving direction of the transmitted portion is reversed by the free end of the drill bit; as a result, a tensile wave approaches the cross-section reduction (Figure 3.12c). A portion of that tensile wave is transmitted to the drill rod to follow the compressive leading portion of σ_2 (Figure 3.12d).

The described mechanism creates a compressive-and-then-tensile wave from a compressive wave, or a tensile-and-then-compressive wave from a tensile wave, by increasing the width of it.

In the real case, the reflected portion of σ_1 is not fully compressive or tensile, but a tensile-and-then-compressive wave. As described in Figure 3.12, the leading tensile portion will be reflected as a tensile-and-then-compressive wave, and the following compressive portion will be reflected as a compressive-and-then-tensile wave. The resulting σ_2 becomes in tensile-compressive-tensile waveform (Figure 3.13b).

A similar analysis can be made for the cross-section increase case, which results in a compressive-tensile-compressive waveform given in Figure 3.13c.

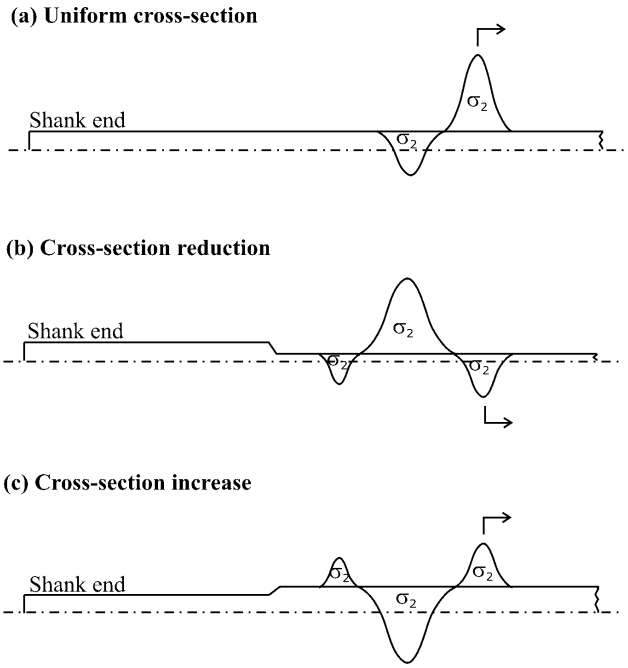

Figure 3.13 Waveforms of σ_2.

With the mechanism creating σ_2 from σ_1, the drill bit keeps creating σ_{n+1} from σ_n, where n is a positive integer. For a given σ_n, the ratio between the compressive and tensile parts of σ_{n+1} is determined by the drill rod diameter and rock hardness. Unless the cross-section of the drill bit is uniform, Equation 3.2 holds for all n:

$$(\text{width of})\ \sigma_{n+1} > (\text{width of})\ \sigma_n \quad . \tag{3.2}$$

3.6 Efficiency of the Successive Incident Wave Series

Efficiency of σ_n, which is denoted by η_n, is defined as the ratio of energy transmitted to the rock by σ_n to the initial piston energy.

Figure 3.14 gives η_1, η_2 and η_3 for different drill rod diameters.

As can be seen in Figure 3.14, when the rock is sufficiently hard, σ_{n+1} cannot make any work on the rock. This can be explained as follows:

When the rock gets harder, σ_1 is reflected back with a smaller tensile portion. However, this is the portion that is going to hit the free edge of the bit and turn back as a compressive wave for the next hit. So, for hard rock case, the compressive portion of σ_2 shrinks and cannot exceed the spring forces reached by σ_1 to make additional work. This is valid for every σ_n and σ_{n+1}, as can be seen in Figure 3.14.

As another output of Figure 3.14, it can be seen that, like σ_1, when we consider σ_n, thinner drill bits are more efficient in softer rock conditions.

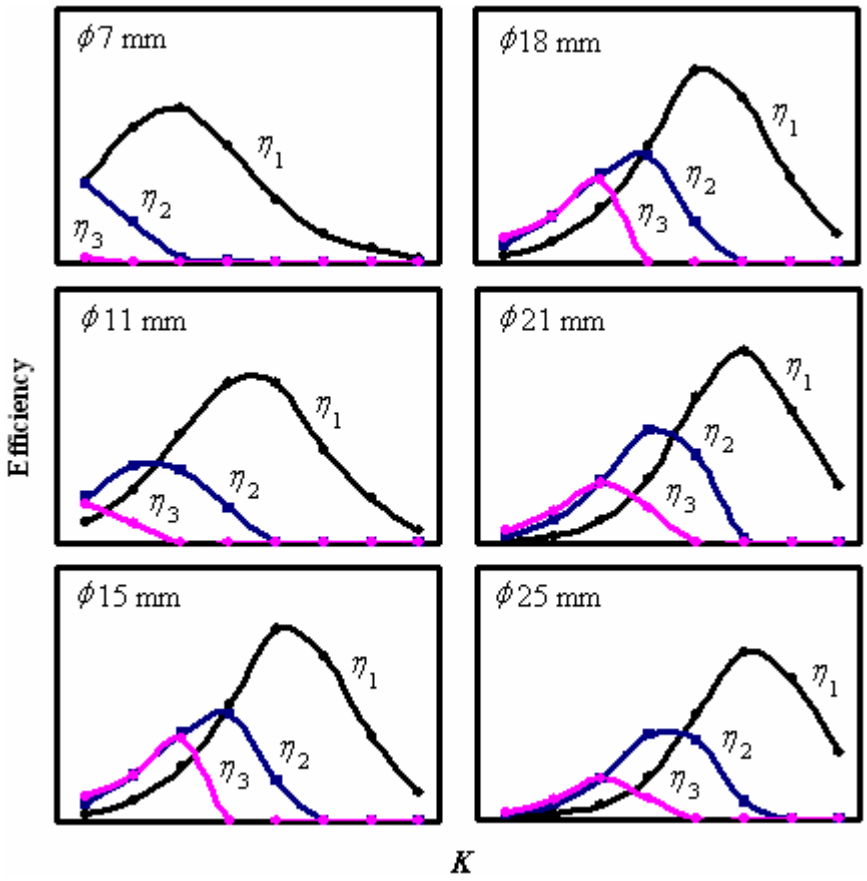

Figure 3.14 η_1, η_2 and η_3 vs. K for varying bit diameter.

The efficiency results presented in Figure 3.14 are obtained by preventing σ_n's affect each other during application on the rock. When the length of the drill bit is sufficiently small, the relationships between successive incident waves can change η_n results. Therefore, actually, the results in Figure 3.14 are also dependent on the drill bit length, which is going to be considered in the next section.

3.7 Efficiency of the Drilling Process

The efficiency of the drilling process, which is denoted by η, is defined as the ratio of work done on the rock to the initial piston energy. As stated before, work is done by σ_n; so,

$$\eta=\eta_1+\eta_2+\eta_3+\dots \quad . \tag{3.3}$$

In Figure 3.15, the efficiency results of a drill bit without a cross-section change (Φ18 mm drill bit) are given. In the figure, four different bits exist with different lengths.

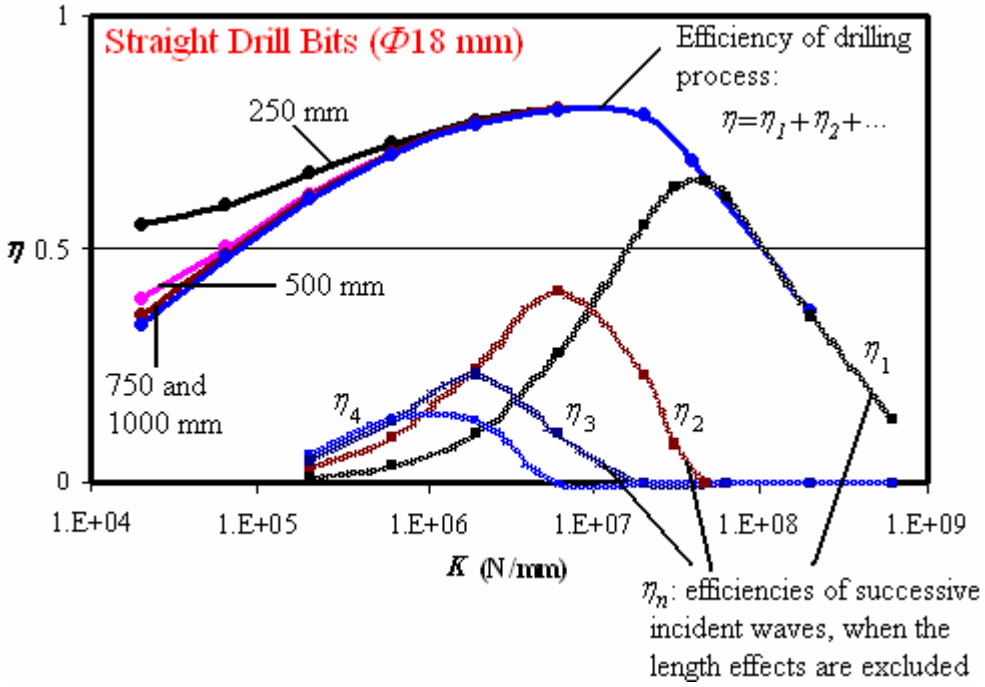

Figure 3.15 η vs. K in Φ18 mm drill bits with varying length.

As can be seen in Figure 3.15, when the rock is hard, $\eta=\eta_1$ (η_2, η_3… are zero). Then, as the rock softens, increasing number of σ_n's start to contribute to the efficiency. Because of that, η does not fall down drastically like η_1 or η_2 with the softening rock.

It can also be seen in Figure 3.15 that, the softening rock creates efficiency differences between short and long drill bits. This can be explained as follows:

After the application of σ_n on the rock (inelastic spring), the spring force reduces to zero. The time that it takes for the reduction is dependent on the spring force and the unloading spring stiffness k (see Figure 3.3). As the spring force and k decrease, the reduction time increases. This can be seen in Figure 3.16.

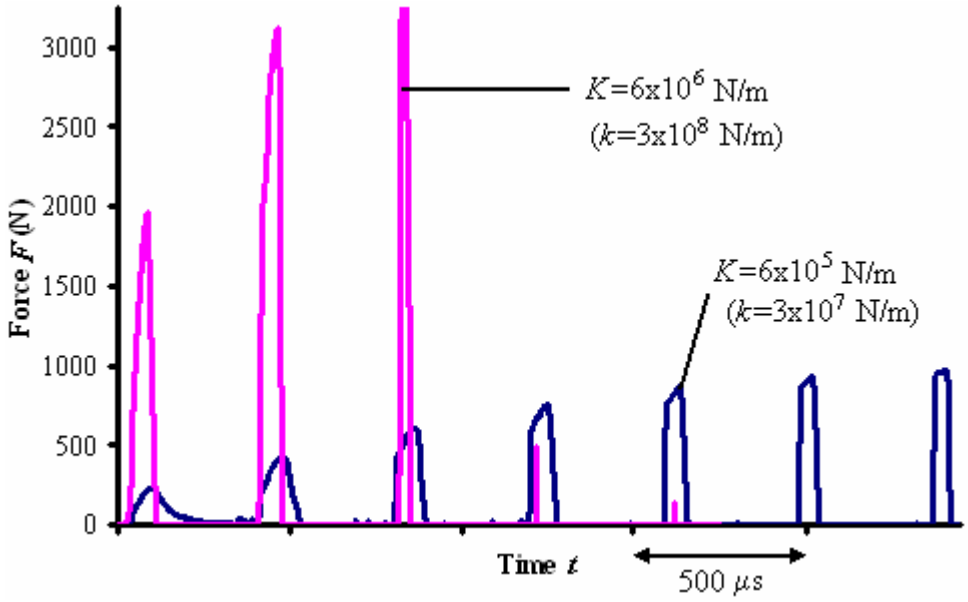

Figure 3.16 Force time history of the rock with respect to K (Φ18 mm, 1000 mm).

As can be seen in Figure 3.16, $|dF/dt|$ during force reduction is low when k or F is low, that is, in case of soft rock. If the rock is sufficiently soft and the bit is sufficiently short, the force cannot drop back to zero after σ_n, before the arrival of σ_{n+1}. This increases the efficiency, because, if the force is zero when σ_{n+1} reach the rock, all the energy is reflected back like a free end reflection at the instant of arrival. But if it is not zero, some of the energy is transmitted, so, η_{n+1} increases.

In short, this phenomenon creates differences between short and long drill bits in case of soft rock, as can also be seen in Figure 3.15. However, this is not the only mechanism differentiating short and long drills. A more important one is explained below:

When the drill bit is long, σ_n are applied on the rock without disturbing each other. However, when the drill bit is short enough, or the stress waves are long enough, the leading portion of σ_{n+1} can reach the rock before the tail of σ_n leaves, and the two portions superpose. If the superposing portions are both compressive, this can lead higher efficiencies (η_n) than the case that σ_n are applied separately. The superposing portions can be both compressive when n>2, and they can superpose only if the rock is sufficiently soft.

In Figure 3.13b, the waveform of σ_2 in a drill bit with a cross-section reduction has been given to be tensile-compressive-tensile. When n>2, the form of σ_n modifies with the inclusion of a compressive leading portion, as it is shown in Figure 3.17 using σ_5.

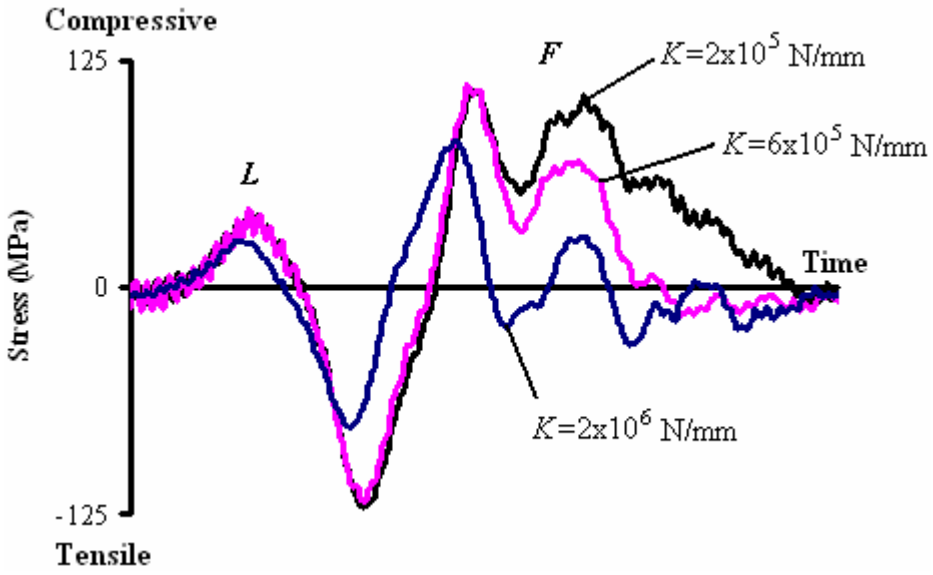

Figure 3.17 Waveform of σ_5 with respect to K (Φ15 mm drill bit).

In Figure 3.17, the wave has two major compressive parts: the leading one denoted by L and the following one denoted by F. The width of F increases as the rock softens. When the width of F is sufficiently long, L of σ_{n+1} can reach the rock before F of σ_n leaves.

For a drill bit without a cross-section change (Φ18) mm, σ_n has a width smaller than 500 mm (see Figure 3.8). Then, it is impossible for σ_{n+1} catch the tail of σ_n, even for the 250 mm drill bit.

On the other hand, the intersection is possible for the bits with a cross-section change: the width of σ_n is greater; more importantly, the width keeps getting wider as n increases (see Equation 3.2). This is approved by the results of Φ15 mm drill bit given in Figure 3.18.

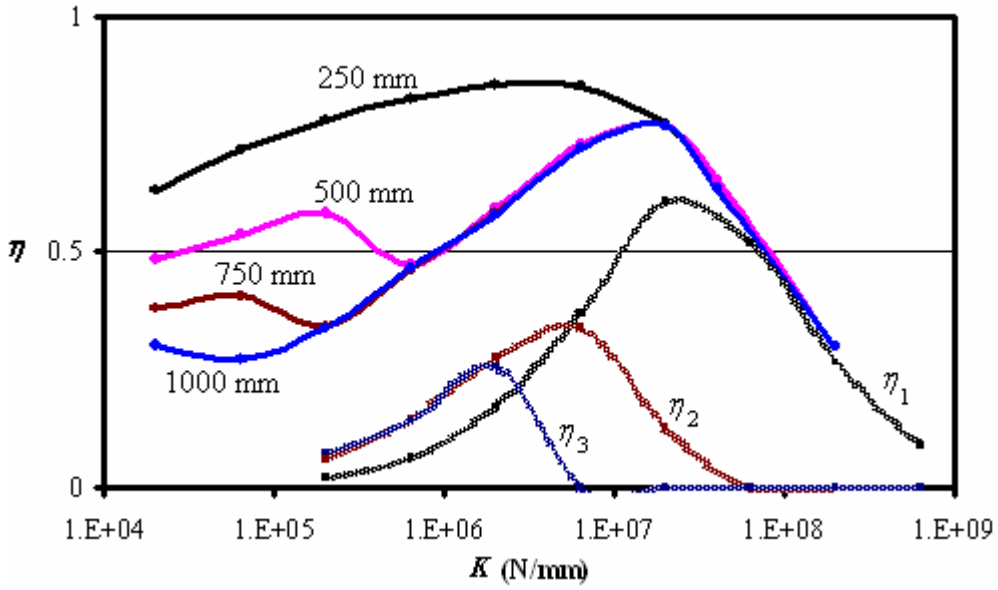

Figure 3.18 η vs. K in Φ15 mm drill bits with varying length.

If the η results of the 500 mm drill bit are investigated, it is seen that the efficiency has two maxima. The one at the right is created by η_1 and η_2 (given in the figure), when the rock is hard. The second maximum is created by the collective application of compressive peaks of successive waves, when the rock gets sufficiently soft.

When the drill bit gets longer, the second maximum occurs at a lower K, because, for overlapping of successive waves in a longer drill bit, F of σ_n (see Figure 3.17) has to be wider. For the 250 mm case, the two maxima are so close to each other that they cannot be distinguished. This coincidence makes a significant positive effect on efficiency.

The location of second maxima changes according to the thickness, too. σ_n, and thus, F of σ_n are wider for a thinner drill bit. This makes overlapping easier, so it can happen in harder rock conditions. That is, when the drill bit gets thinner, the second maximum

occurs at a higher K. This is approved in Figure 3.19, in which the efficiency results of Φ11 and Φ15 mm drill bits are given together. The second maximum points are displayed in squares.

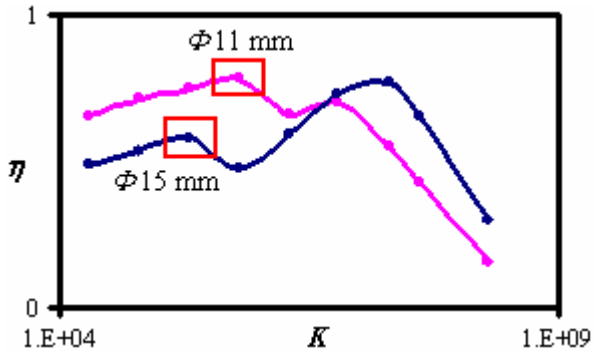

Figure 3.19 η vs. K in 500 mm drill bits with varying thickness.

In Figure 3.19, the first peak in efficiency regime occurs at a softer rock for the thinner drill bit, because incident stress waves in thinner drill bits are more appropriate for softer rocks, as it was stated before (see Figure 3.14).

In Figure 3.20, the efficiency results of Φ11 and Φ7 mm drill bits are given.

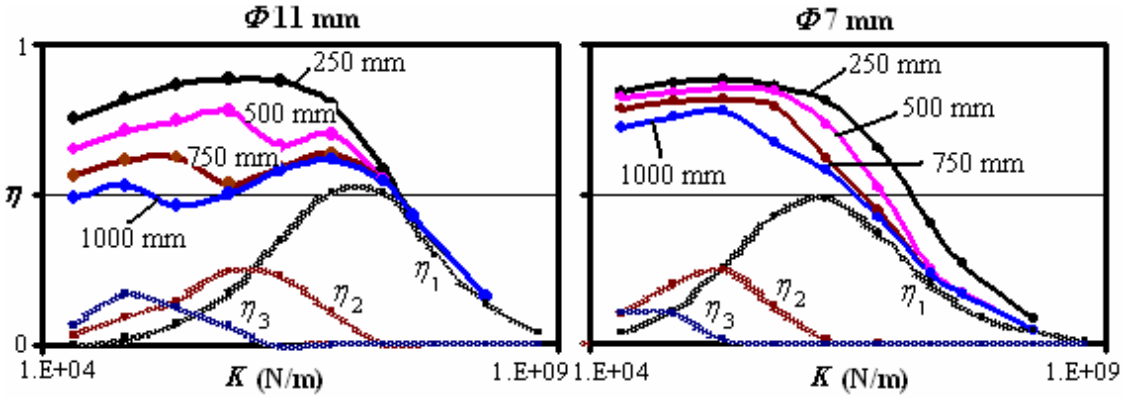

Figure 3.20 η vs. K in Φ11 and Φ7 mm drill bits with varying length.

When the diameter of the drill rod reduces, the wave interactions have a greater positive effect on η_n, and thus on η, as can also be seen in Figure 3.20.

In Figure 3.21, the efficiency results of drill bits with cross-section increase are given.

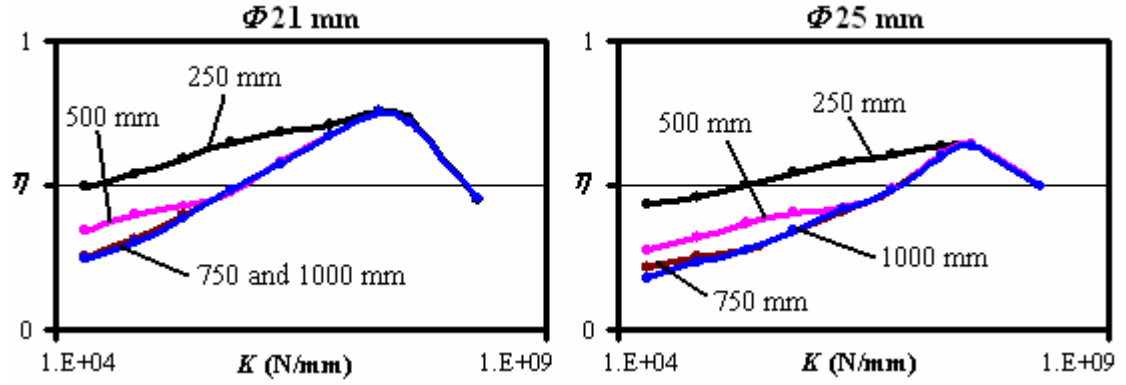

Figure 3.21 η vs. K in Φ21 mm and Φ25 mm drill bits for varying length.

In case of cross-section increase, the wave interactions have a greater positive effect as the drill bit gets thinner, because the width of η_n is greater for a thinner drill bit.

It can be concluded from Figures 3.15 to 3.21 that, the shorter drills are more efficient than the longer ones regardless of the drill bit diameter, mainly because of the intersections of the successive incident stress waves. The intersections cannot be seen in drill bits without a cross-section reduction, so the efficiency is less dependent on length in such drill bits. The length effects increase with softening rock, in addition, the efficiency is not dependent on the length, if the rock is sufficiently hard.

A drill bit design has two local maxima of efficiency with respect to rock hardness. One occurs when the rock is harder, while lower number of incident waves is contributing to the work done on the rock; the other occurs as the number of contributing incident waves increase and they start to intersect with each other. Any of the local maxima can be the global maximum dependent on the length and diameter of the drill bit.

The distance (in rock hardness) between the two maxima increases as the drill bit gets thicker and longer. So, the two maxima cannot be observed separately if the drill bit is very short or thin.

3.8 Summary

The efficiency of a drill bit without a cross-section change has been given before in the literature. This result is given in Figures 3.22 and 3.23 for different lengths (Φ18 mm drill bits). Besides, drill bits with a cross-section reduction, and the drill bits with a cross-section increase are given in Figures 3.22 and 3.23, respectively.

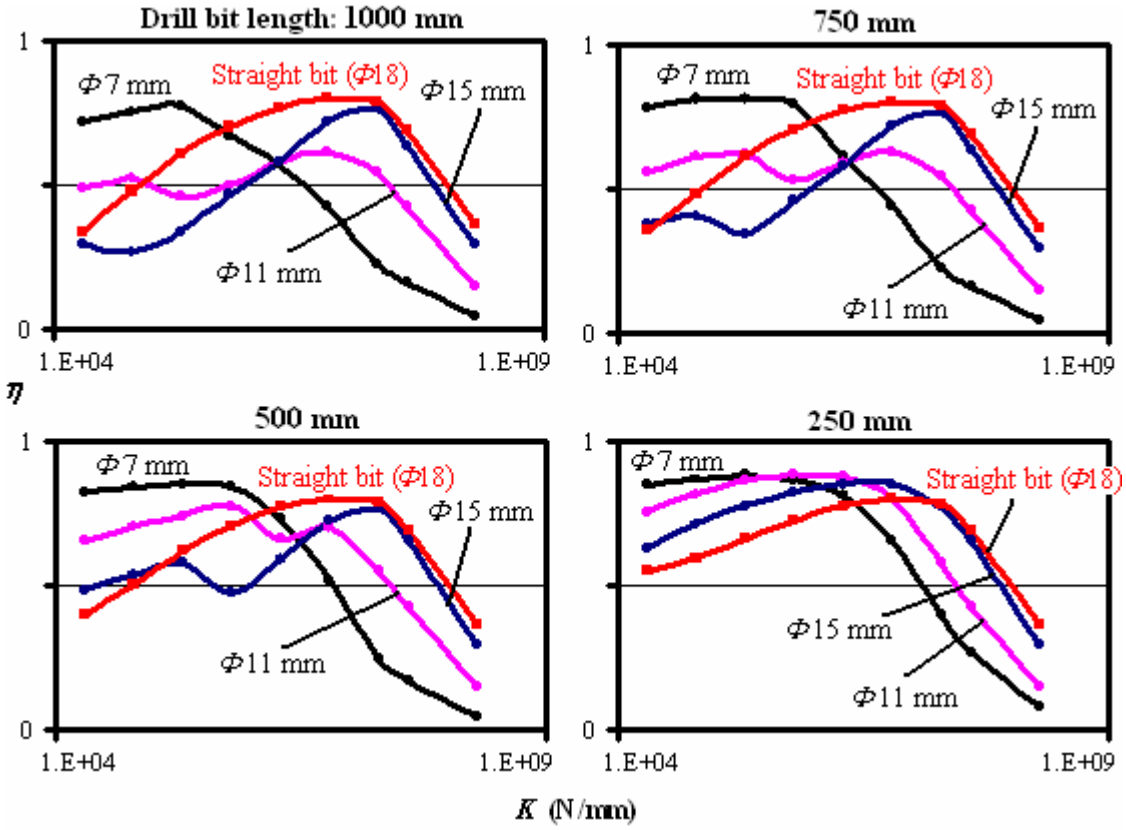

Figure 3.22 η vs. K for the drill bits with a cross-section reduction.

In Figure 3.22, it can be seen that the efficiency of a straight drill bit is better than one with a cross-section reduction for hard and medium rock. However, for soft rock, especially with the help of length effects, the thinner drill bits get more efficient. The efficiency of thinner drill bits increase as the drill bit gets shorter.

When only the drill bits with a cross-section reduction are observed, the conclusion drawn is, thinner drill bits are more efficient for softer rock, while thicker drill bits are more efficient for harder rock. This is because, as stated before in sections 3.4 and 3.6, thinner drill bits produce stress waves which are more suitable for soft rock. The dependency on thickness decreases for medium rock.

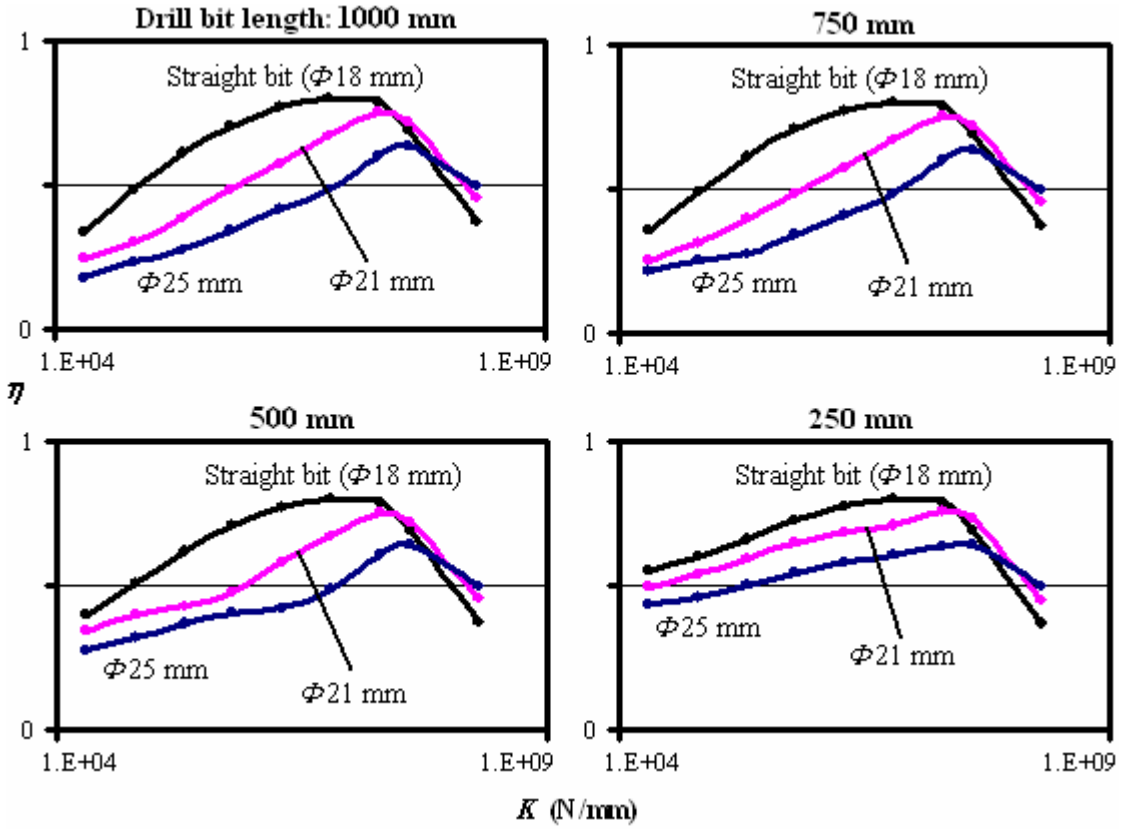

Figure 3.23 η vs. K for the drill bits without a cross-section reduction.

When it comes to drill bits with a cross-section increase, the length effects are not so efficient in those bits; hence, although their efficiencies increase as the drill bit shortens, they cannot be more effective than Φ18 mm drill bit, even in soft rock case.

In Figure 3.23, thicker drill bits are more efficient in hard rock, while Φ18 mm drill bit is more efficient in medium and soft rock.

When the results of Figure 3.22 and Figure 3.23 are combined, following guidelines can be obtained:

Thinner drill bits are more efficient in softer rock (especially because of length effects), while the thicker drill bits are more efficient in harder rock. In medium rock hardness (around K=2x10^6 N/m), for cross-section reduction case, the efficiency is not dependent on thickness. When the straight drill bit is observed in medium rock hardness, it can be noticed that the efficiency of it is higher than the thinner ones.

Decreasing length increases the efficiency for bits with a cross-section change, especially for the ones with a cross-section reduction. As a result, for the shortest drill bits (250 mm), the thinner drill bits are more efficient than Φ18 mm even in medium rock.

CHAPTER 4

STRESSES IN DRILL BITS WITH RESPECT TO DRILL BIT DIMENSIONS

4.1 Introduction

During a single hit of the hammer drilling process, the initial kinetic energy of the piston is transferred to the drill bit in terms of an axial stress wave called the initial stress wave. The task of the drill bit is to convert the initial stress wave into successive incident waves to hit the rock. Some of the energy carried by the incident waves is transmitted to the rock, while some is reflected back in terms of reflected stress waves. The energy transmission to the rock continues until the contact between the bit and the rock ceases. After the contact, the remaining energy keeps traveling back and forth in the bit in terms of stress waves, which are weakened by damping while the drill bit waits for the next piston hit.

In Figure 4.1, the axial stress time history of a point that is on the axis and 56 mm away from the bottom (see Figure 3.1) in a 500 mm long, Φ7 mm drill bit is given. The rock hardness is $2x10^6$ N/m, and stiffness damping is applied on the model with a coefficient of $1x10^{-4}$.

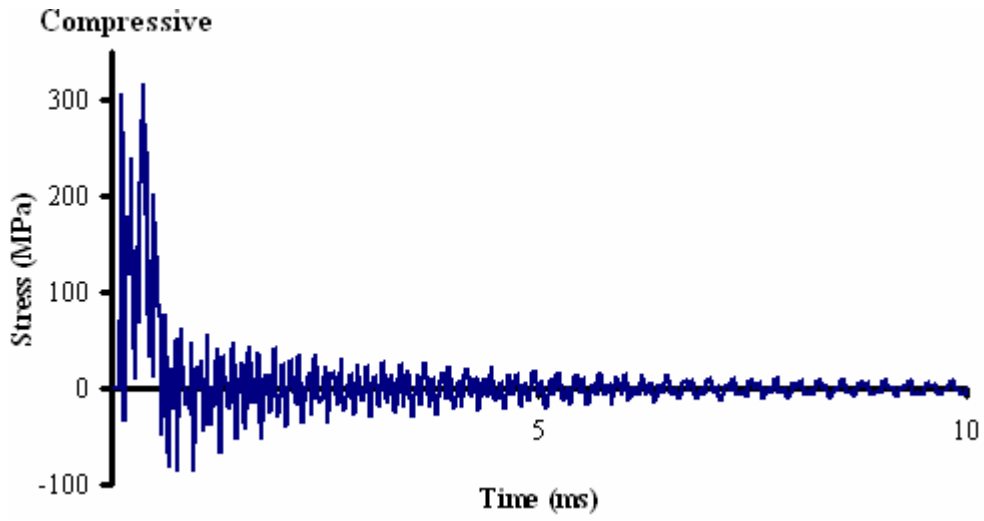

Figure 4.1 Stress time history of a point for 10 ms.

Stress data given in Figure 4.1 reveals the general stress behavior of a point in a drill rod during a single hit of the impact drilling: The point experiences the maximum compressive and tensile stress values before the stress waves weaken by transmitting their energy to the rock or as a result of damping. After the maximum values, the point keeps experiencing compressive and tensile stresses with the effect of the energy that could not be transmitted to the rock. Damping reduces the magnitude of these stresses by time.

As stated before, the effect of the stress waves that do not die out until the next hit is neglected in this study. This is a logical assumption with the modern drilling machines creating 2000-3000 hits per minute.

In this chapter, stress time histories of points along drill bits are investigated during one hit of the piston with respect to drill bit dimensions taking rock hardness into

consideration. Maximum tensile and compressive stress values reached are used for comparison.

Because of the high length-thickness ratio of the bits, the stress waves behave like one-dimensional stress waves, and the radial and circumferential stresses created by the waves are very low with respect to axial stresses. In this section, only the axial stress results are given. Besides, because of the one-dimensional waves again, axial stresses do not change in a section depending on distance to the central axis. Thus, throughout the chapter, data taken from the axis is assumed to represent the section.

For convenience, the incident stress waves are going to be called σ_{in} (it was σ_n in the previous chapter), where n is a positive integer; in addition, their reflections from the drill bottom are going to be called σ_{rn}. All other conventions used in Chapter 3 are valid in Chapter 4.

4.2 Maximum Tensile Stress

The piston impact introduces a compressive wave to the drill bit. However, during reflections from the cross-section (c-s) change and the two ends of the bit, incident and reflected stress waves with tensile portions can be produced. A point in a drill bit can experience high tensile stresses under the single or common effect of these tensile portions.

At the points near the drill bit bottom, σ_{in} hits the bottom and is reflected back as σ_{rn}. During this process, the points are under the collective effect of σ_{in} and σ_{rn}. On the other hand, at the points near the drill shank, σ_{rn} hits the c-s change and is reflected back as σ_{in+1}. During this process, the points are under the collective effect of σ_{rn} and σ_{in+1}. The waves can apply individually only at the points that are far away enough from the drill bit ends.

The lengths of regions under the effect of wave intersections are dependent on the widths of the intersecting waves. In a drill bit with a c-s change, the width of σ_{in} increases with n (See Chapter 3). As a result, the region of σ_{in+1} - σ_{rn+1} superposition is longer than the region of σ_{in} - σ_{rn} superposition.

In the regions of superposition, the tensile portions of σ_{in} and σ_{rn} can cooperate, leading higher tensile stresses than the ones that the waves could create separately, or, on the contrary, a compressive portion of a wave can reduce the effect of a tensile peak. Knowing the forms of the incident and reflected waves in a drill bit, the maximum tensile stresses along it can be interpreted.

Below, first, maximum tensile stresses in 3000 mm drill bits are going to be investigated with respect to data point, diameter of the drill rod and rock hardness, successively. Then, the stresses in 250, 500, 750 and 1000 mm long drill bits, which is in the main scope of this study, are going to be interpreted benefiting from the 3000 mm results.

4.2.1 Effect of Location

In this section, maximum tensile stresses along a 3000 mm long, Φ7 mm drill bit are given when K=2x10^4 N/m (soft rock case).

The maximum tensile stresses are not generally created by σ_{in} where n>3, because of three main reasons: first, the waves lose energy to the rock in every hit, second, the c-s change divides σ_{in} into parts in every pass reducing the maximum magnitude, and third, damping.

In Figure 4.2, the first three incident and reflected waves are given in space domain together for a Φ7 mm drill bit in case of soft rock The results of the thicker drill bits also exist, which are going to be referred in the following sections.

As can be seen in Figure 4.2.b, σ_{r1} is fully tensile because of the very soft rock, and the peak point of it, which is denoted by R_1 in the figure, is the greatest tensile stress reached by the first three incident and reflected stress waves. Naturally, R_1 can be expected to create the maximum tensile stresses along the drill bit.

The results in Figure 4.2 are given in order to be used in interpreting the maximum stress results in the drill bits. The maximum stress results are obtained from successive points along the axis of the drill rod selected to have 8 mm gap between.

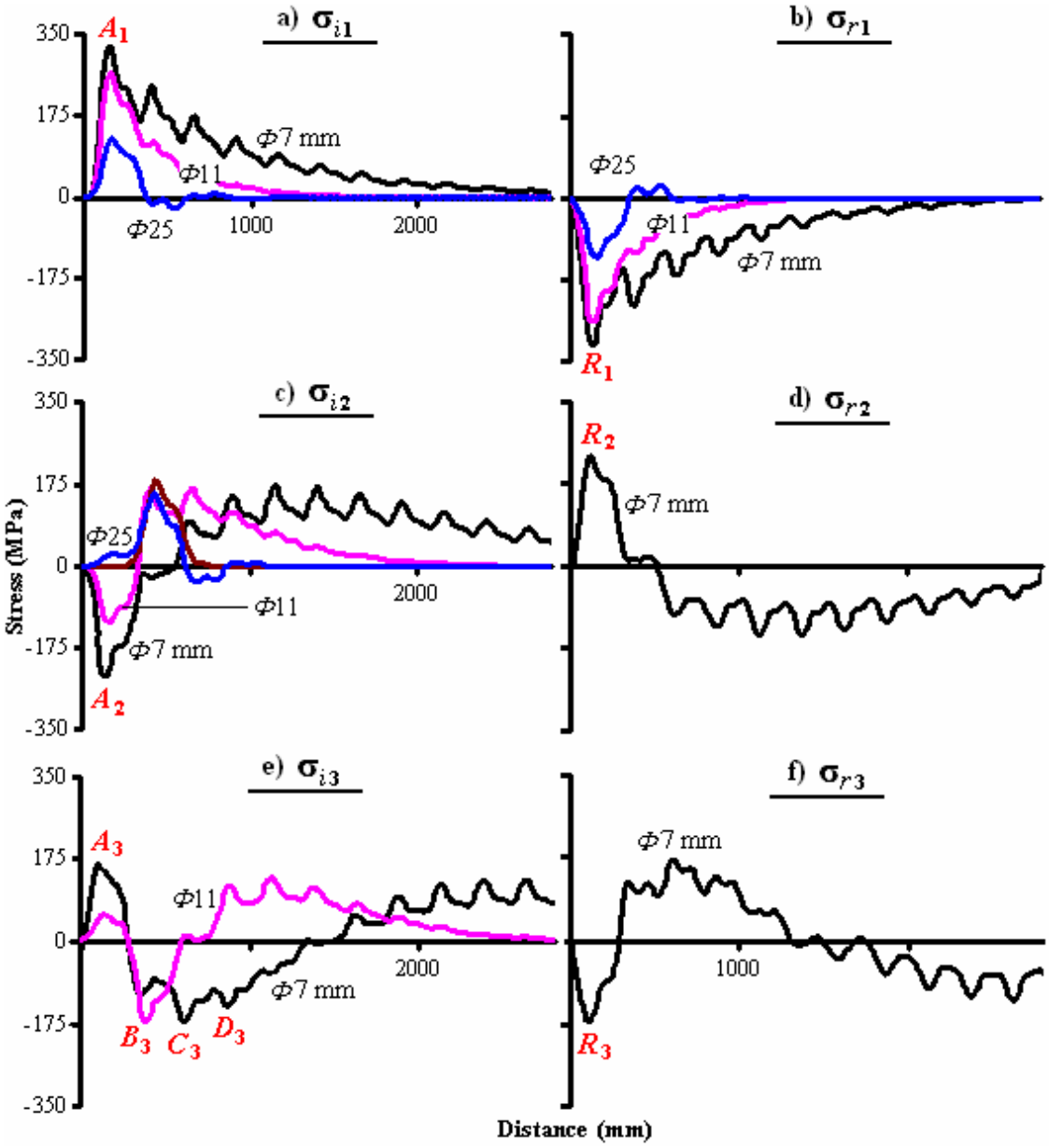

Figure 4.2 σ_{i1}, σ_{i2}, σ_{i2}, σ_{r1}, σ_{r2} and σ_{r3} when K=2x10^4 N/m.

In Figure 4.3, the maximum tensile stress values reached by those points are plotted. The abscissa axis, *d*, is the distance from the drill bit bottom, where the bit touches the rock.

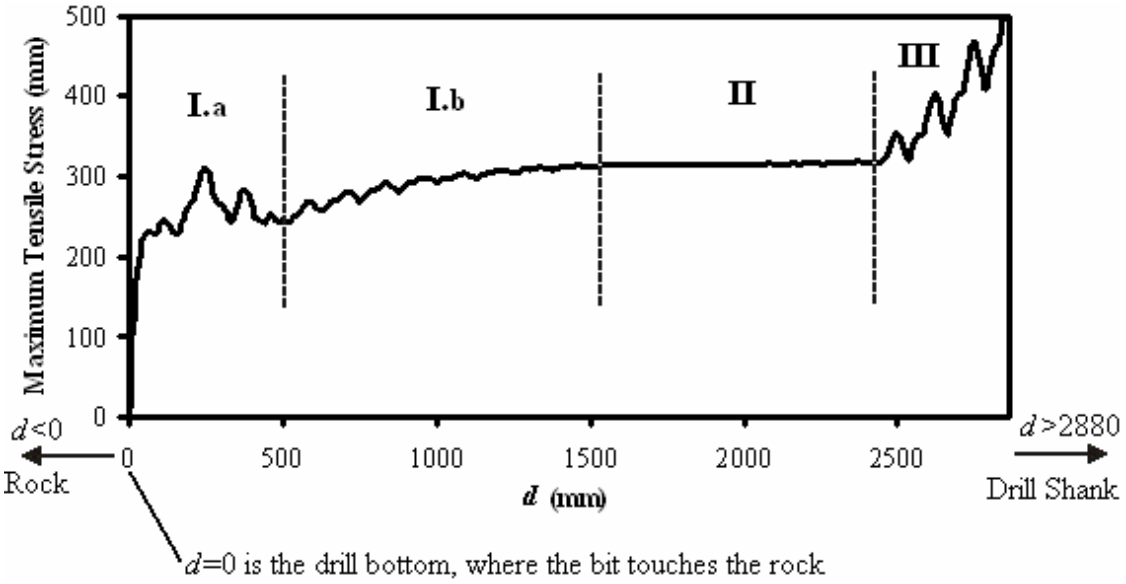

Figure 4.3 Maximum tensile stresses when K=2x10^4 N/m (3000 mm long, Φ7 mm).

As designated in Figure 4.3, the results can be divided into four regions. In Region II, R_1 creates the maximum tensile stresses individually, without superposing with other tensile or compressive waves. As a consequence, the maximum tensile stresses are stable in this region with a magnitude that is equal to the magnitude of R_1.

In Region I, R_1, which is moving towards the drill shank, coincides with the compressive peaks of σ_{i1}, which are moving towards the rock. One can easily show that the length of Region I equals to the half-width of σ_{i1}.

As d decreases, R_1 coincides with a greater compressive peak of σ_{i1}; as a result, in Region I.b, the maximum tensile stresses decrease towards the drill bottom, with a zigzag appearance. When it comes to Region I.a, the stresses created by the $\sigma_{r3} - \sigma_{i3}$ superposition exceeds the stresses created by the $\sigma_{r1} - \sigma_{i1}$ superposition:

The tensile leading peak of σ_{r3}, which is denoted by R_3 in Figure 4.2.f, coincides with the tensile peaks of σ_{i3}, which are denoted by B_3, C_3 and D_3 in Figure 4.2.e. As d increases, R_3 coincides with A_3, B_3 and C_3, successively. The maximum tensile stress values created by R_3+A_3, R_3+B_3 and R_3+C_3 give its zigzag form to Region I.a. In other words, Region I.a takes its shape from the tensile region of σ_{i3}, like Region I.b taking its zigzag appearance from σ_{i1}.

In Region I.a, stresses created by σ_{i2} - σ_{r2} couple cannot exceed the ones by $\sigma_{i3} - \sigma_{r3}$, because, since it is impossible for the tail of σ_{rn} to catch the head of σ_{in}, the tensile portions of σ_{i2} and σ_{r2}, which can be seen in Figures 4.3.c and 4.3.d, cannot superpose. This situation holds for every σ_{in}, where n is a positive even number.

In Region III, the highest tensile stresses are created by the tensile leading peak of A_2, which is coinciding with the tensile peaks of σ_{r1}. As d increases, A_2 coincides with a greater peak of σ_{r1}; as a result, the maximum tensile stresses increase with d, with a zigzag appearance. The length of Region III is dependent on the width of the tensile portion of σ_{r1} and the magnitudes of the tensile peaks.

4.2.2 Effect of Thickness

The changes in the magnitudes and widths of the incident and reflected waves with respect to thickness give rise to the changes in maximum tensile stresses. In Figure 4.4,

maximum tensile stress results of 3000 mm drill bits with different thicknesses are given together. The results of Φ7 mm and Φ11 mm drill bits are divided into regions.

It may be beneficial to remind that, the drill shank diameter being Φ18 mm, the drill bits with Φ7, Φ11 and Φ15 mm diameter have a c-s reduction, and the bits with Φ21 and Φ25 mm diameter have a c-s increase between the drill shank and the drill rod (See Figure 3.1).

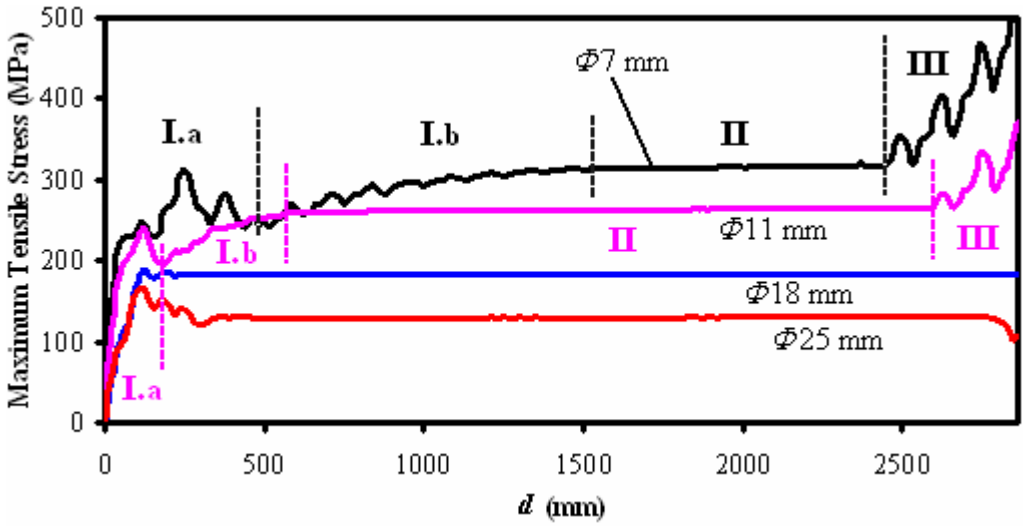

Figure 4.4 Maximum tensile stresses in 3000 mm drill bits when K=2x10^4 N/m.

As can be seen in Figure 4.4, Regions I and III shorten with thickness in case of c-s reduction, take the shortest form for the Φ18 mm drill bit, and elongate with thickness in case of c-s increase. These changes are parallel to the changes in the widths of intersecting waves. The incident and reflected waves in a drill bit are enlarged by the c-s change, especially by the c-s reduction (see Chapter 3).

When we come to the effect of thickness on magnitudes, it is seen in Figure 4.4 that, maximum tensile stresses in Region I.b, II and III decrease with increasing thickness. This is due the decreases in the magnitudes of σ_{r1} and A_2 (reflection of R_1 from the c-s change) that are creating the maximum stresses in those regions. The effect of thickness on σ_{r1} and A_2 can be seen in Figure 4.2.b and Figure 4.2.c, respectively.

Taking its form from the tensile portion of σ_{i3}, the changes in Region I.a arise due to the changes in the form of σ_{i3}. For instance, as can be seen in Figure 4.2.e, tensile portion of σ_{i3} in a Φ7 mm bit is wider with three peaks (B_3, C_3, D_3), unlike that of a Φ11 mm that is narrower with only one peak (B_3). Accordingly, Region I of a Φ7 mm drill bit is wider with three peaks, while that of a Φ11 mm is narrower with one peak, as can be seen in Figure 4.4.

As an important point, in Region III, in case of c-s increase, unlike the case of c-s reduction, R_1 is reflected being a compressive wave, and decreases the maximum stresses in this region, with respect to Region II.

As a detail worth noting, in case of c-s reduction, maximum tensile stresses can be greater for thicker drill bits in some regions of the drill bit, because σ_{i1}, which is a powerful compressive wave, is narrower for thicker drill bits. An example for the case can be seen in Figure 4.4 around d equals 500, between Φ7 mm and Φ11 mm drill bits.

4.2.3 Effect of Rock Hardness

Altering the rock hardness make significant changes on the stress waves which play important roles in creating maximum tensile stresses.

First, when the rock gets harder, the tensile portion of σ_{r1} shrinks, and decreases the magnitude of R_1. In Figure 4.5, the magnitude of R_1 is given with respect to K for drill bits with varying thickness.

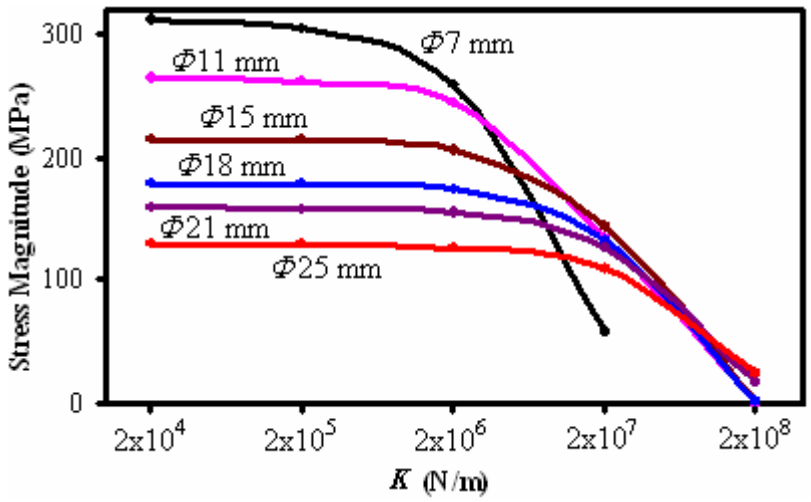

Figure 4.5 The magnitude of R_1 vs. K for varying thickness.

According to the results in Figure 4.5, the magnitude of R_1 falls down as rock hardens, and it is more sensitive to K in thinner drill bits.

Second, when the rock gets harder, the compressive portion of σ_{r1} grows. This large compressive portion hits the free end of the drill bit, and is reflected back as a tensile portion added to the tail of σ_{in} (n>1). When R_1 reduces because of rock hardness, this tensile portion, which grows with thickness, takes the task of creating maximum stresses over.

Maximum tensile stress results when K equals $2x10^4$ N/m were given in Figure 4.4. In Figure 4.6, maximum tensile stresses for harder rock conditions can be seen.

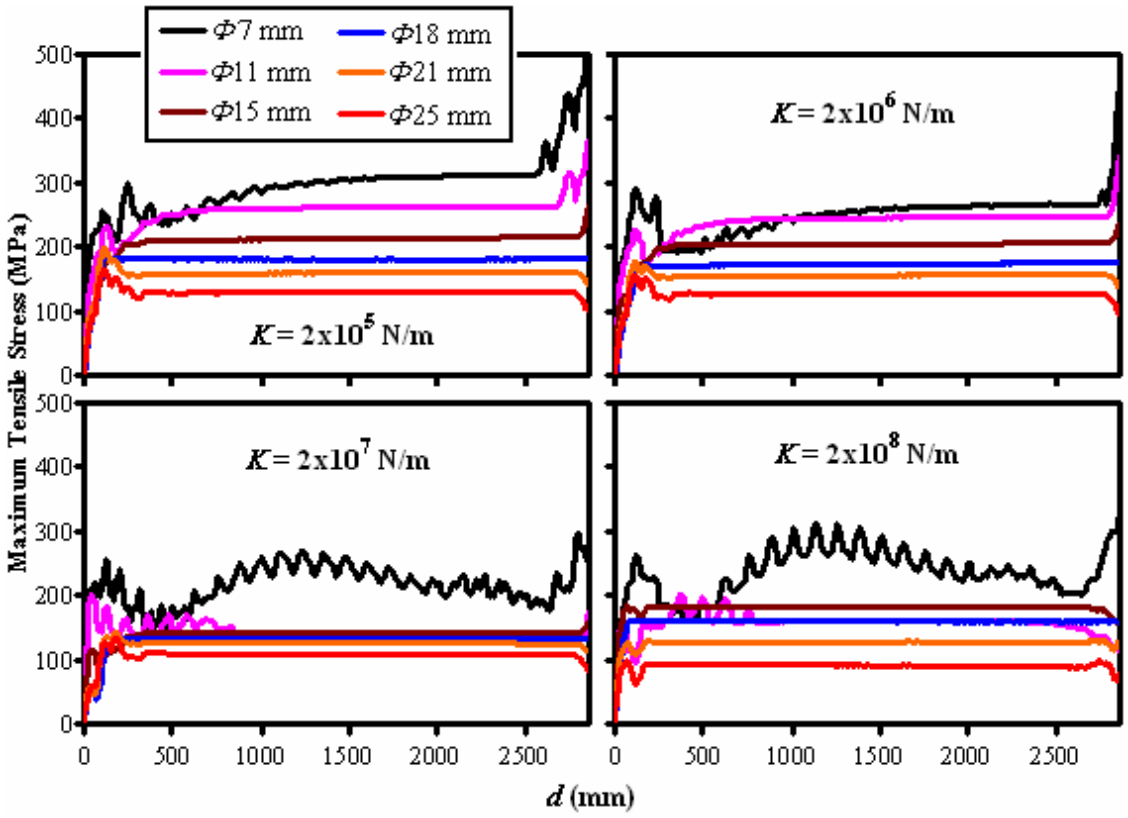

Figure 4.6 Maximum tensile stresses in 3000 mm drill bits for varying K.

As can be seen in Figure 4.5, when K equals $2x10^4$ N/m, R_1 is greater for a thinner drill bit. When K increases to $2x10^5$ N/m and $2x10^6$ N/m, this order does not change; in addition, R_1, in the drill bits other than Φ7 mm, does not undergo a significant decrease. As a result, the general behavior of maximum tensile stress results seen in Figure 4.4 (K=$2x10^4$ N/m) does not change except the fall in Φ7 mm bit.

When K jumps from $2x10^6$ N/m to $2x10^7$ N/m, for the Φ7 mm drill bit, R_1 reduces too much that it cannot create the maximum tensile stresses any more. Instead, R_3, superposing with σ_{i3}, creates the maximum tensile stresses along the entire drill bit.

Accordingly, as can be seen in Figure 4.6, the maximum stresses along the entire bit take the shape of σ_{i3}, the waveform of which is given in Figure 4.7.

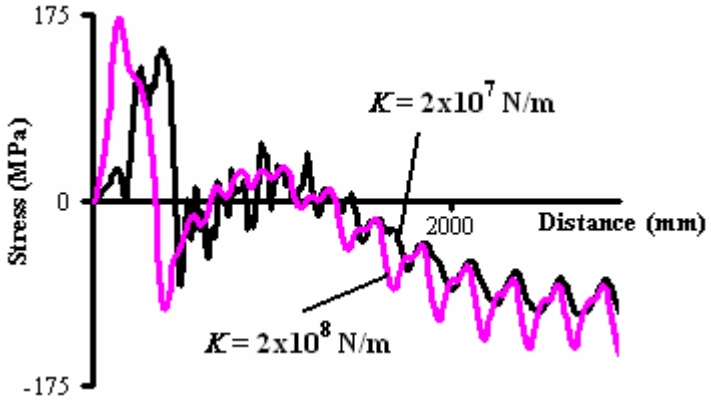

Figure 4.7 σ_{i3} in Φ7 mm drill bit for varying K.

In Φ11 mm drill bit, σ_{i3} is not as wide as it is in Φ7 mm bit, so it cannot change the whole appearance of the results. Other than the zigzag regions in Φ7 and Φ11 mm drill bits, the maximum tensile stress magnitudes are low with the values of R_1 seen in Figure 4.5 for K=2x10^7 N/m.

When K jumps to 2x10^8 N/m, R_1 approaches zero for all drill bits, and the tensile tails of σ_{i2} and σ_{i3} take the task of R_1 over. These tensile tails grow with thickness, and increase the stress values with respect to the case when K equals 2x10^7 N/m.

4.2.4 Effect of Length

The results between short and long drill bits differ because of the superposition of σ_{in} and σ_{in+1}, as it was mentioned in Chapter 3. When the drill bit is long enough, or the

stress waves are not long or high enough, this superposition does not occur, or occurs to a limited extent; and the length effects cannot contribute the maximum stress results.

σ_{i1} is reflected being a tensile wave in case of soft rock, and being a compressive wave in case of hard rock. However, medium rock divides it into compressive and tensile portions, creating two smaller waves from one bigger wave, and thus, reduces the possibility of length effects contribute the results.

In Figure 4.8, results of drill bits with different lengths are given in case of soft rock.

As can be seen in Figure 4.8, if the drill bit is thicker than Φ15 mm, the stress waves are not long enough to intersect and create differences between short and long drill bits, which is not the case for the thinner drill bits. Generally, the stresses tend to increase at the regions of intersection.

Regarding 250, 500, 750 and 1000 mm long drill bits, it can be said that, the points near the drill shank are more critical in case of c-s reduction, while the ones near the bottom are more critical in case of c-s increase. The maximum stresses decrease with thickness. In the most critical case, when the drill bit is the thinnest and the points near the drill shank are considered, the longer drill bits are more critical reaching higher tensile stresses.

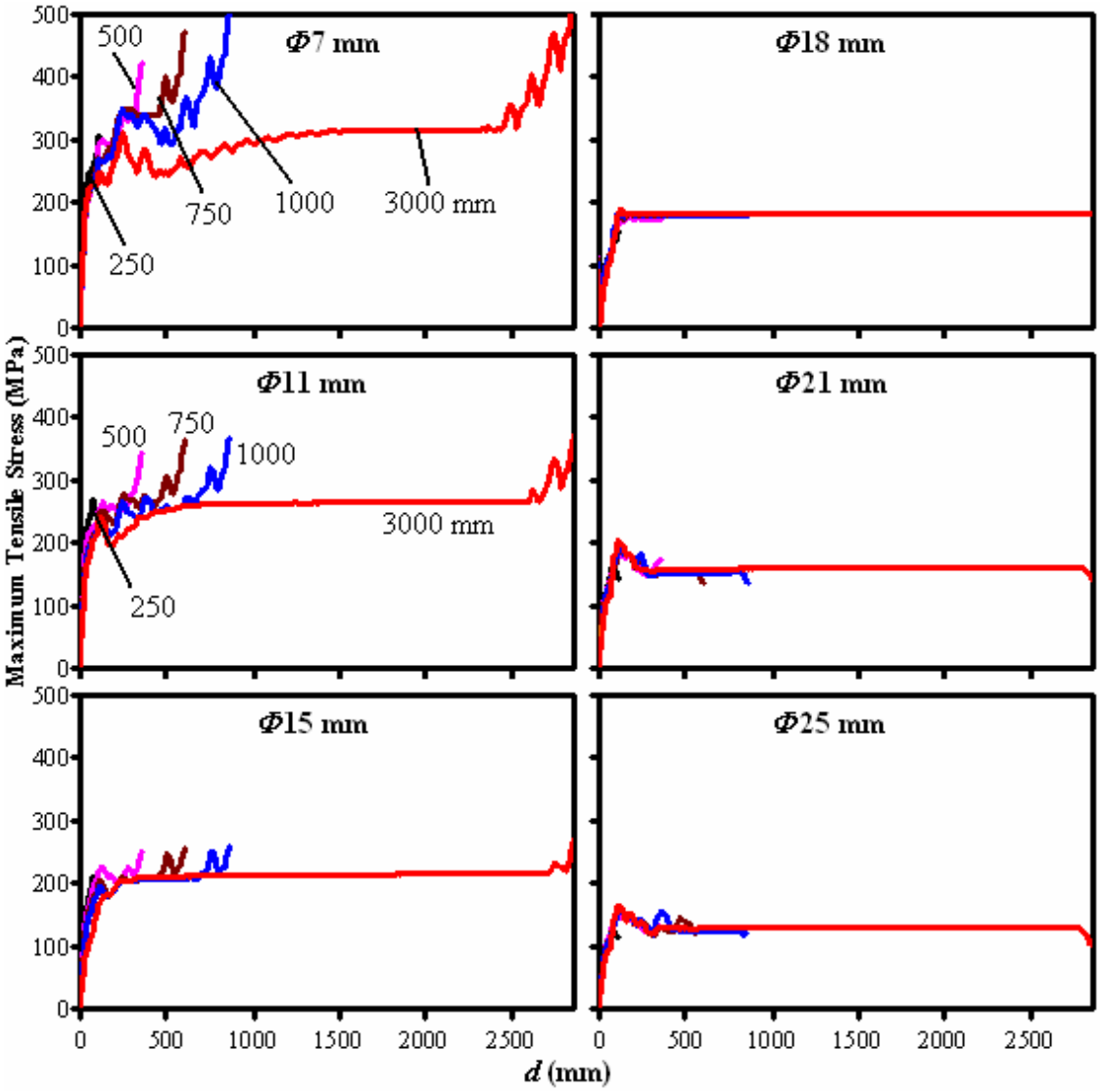

Figure 4.8 Maximum tensile stress vs. d when K=2x10^4 N/m.

The case of medium rock ($K=2x10^7$ N/m) is given in Figure 4.9.

As can be seen in Figure 4.9, in case of medium rock, the results of bits with different lengths cannot be distinguished from each other, except in Φ7 mm drill bits. In other words, length effects cannot contribute to the results except in Φ7 mm drill bits. In 7 mm drill bits, the incident and reflected waves are wider, so they can superpose with each other to a greater extent than they do in thicker drill bits, where the waves are narrower.

Regarding 250, 500, 750 and 1000 mm long drill bits, the stresses are greater in thinner drill bits. In addition, in case of c-s reduction, the proximity of drill bottom is as critical as the proximity of drill shank, which was not the case in soft rock.

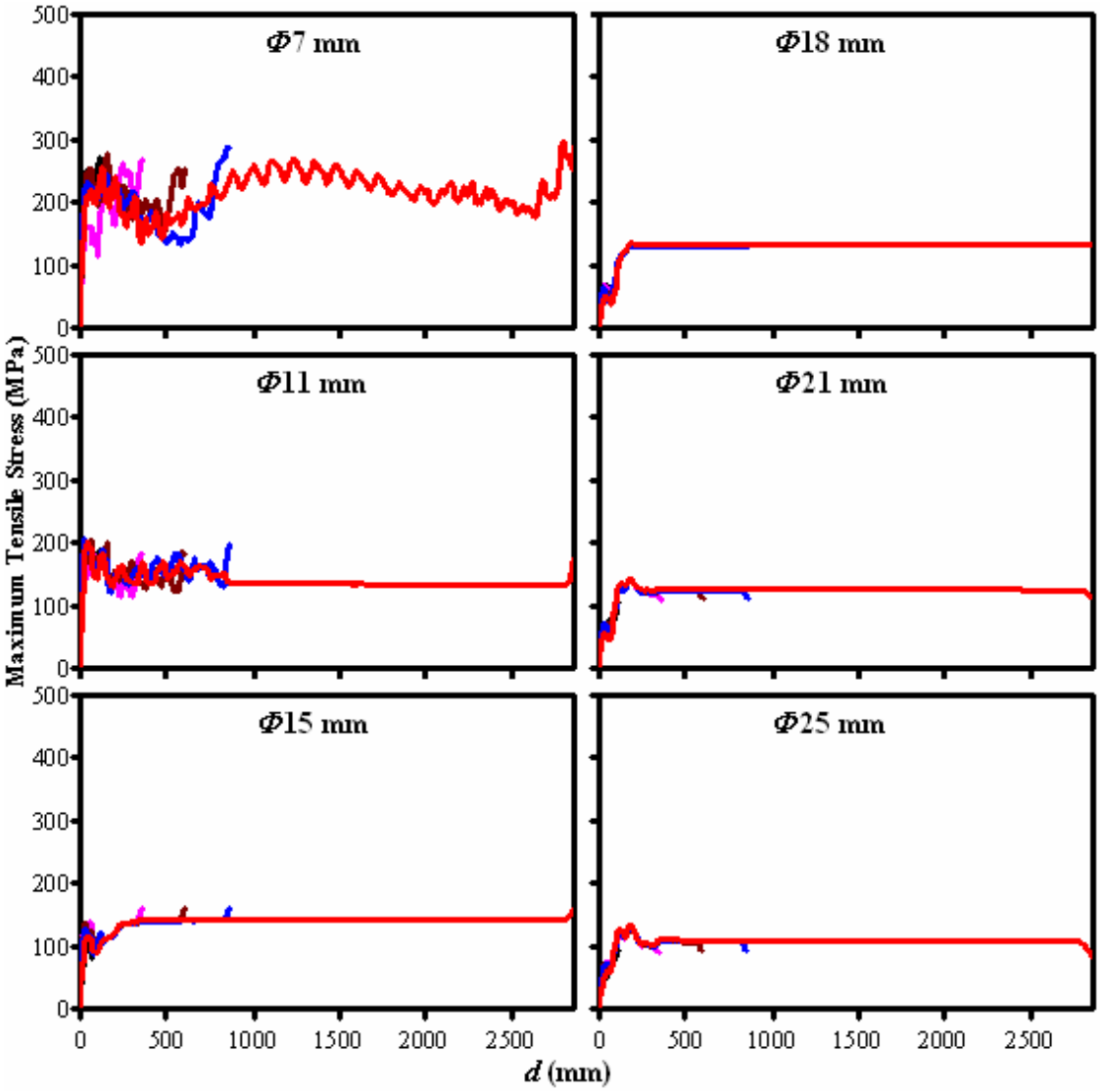

Figure 4.9 Maximum tensile stress vs. d when K=2x10^7 N/m.

The case of hard rock is given in Figure 4.10.

In case of hard rock, the length effects are greater than they are in case of soft rock.

Regarding 250, 500, 750 and 1000 mm long drill bits, it can be said that, shorter drill bits experience higher tensile stresses, and the maximum stresses generally decrease with thickness.

4.3 Maximum Compressive Stresses

When the compressive stresses are concerned, the compressive peak point of σ_{i1}, which is denoted by A_1 in Figure 4.2 is the highest compressive point in the first three incident waves, and is expected to create the greatest compressive stresses along the drill bit.

Like the highest tensile peak R_1, the magnitude of A_1 decreases with thickness, and unlike R_1, A_1 is independent of hardness. Besides, being the leading peak of the first incident wave, A_1 cannot be under the effect of any coinciding wave. Hence, any point on the drill rod must have a maximum compressive stress at least with the magnitude of A_1. Other waves can exceed the value reached by A_1 by superposition.

Naturally, a point can have a higher maximum compressive stress with the help of the wave superposition committed by following incident and reflected waves.

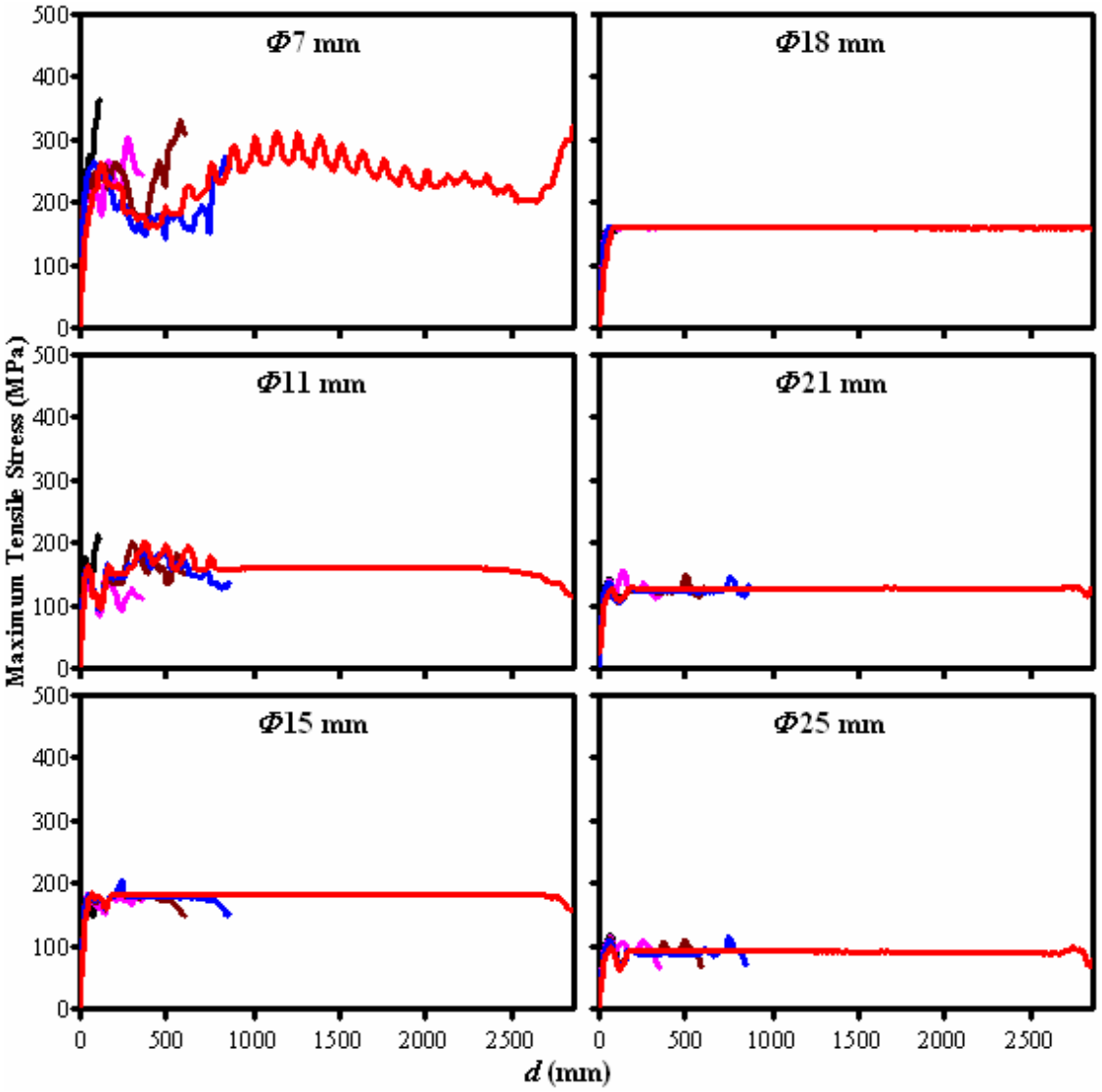

Figure 4.10 Maximum tensile stress vs. d when K=2x10^8 N/m.

4.3.1 Soft Rock Case

The results in case of soft rock are given in Figure 4.11.

In case of soft rock, maximum compressive stresses are created mostly by A_1. When the drill rod diameter is Φ7 mm, R_2 can exceed the stresses created by A_1 between d=340 and d=1050, where it coincides with the greatest peaks of σ_{i2}. As a result, this portion gains a zigzag appearance, which is the waveform of σ_{i2}. With thickness, the width of σ_{i2}, and the magnitude of R_2 decreases, causing the zigzag appearance disappear.

The length effects tend to increase the compressive stresses reached, but cannot be successful in bits thicker than Φ11 mm.

Regarding 250, 500, 750 and 1000 mm long drill bits, it can be said that, the points near the drill shank are compressed more, and the stresses decrease with thickness.

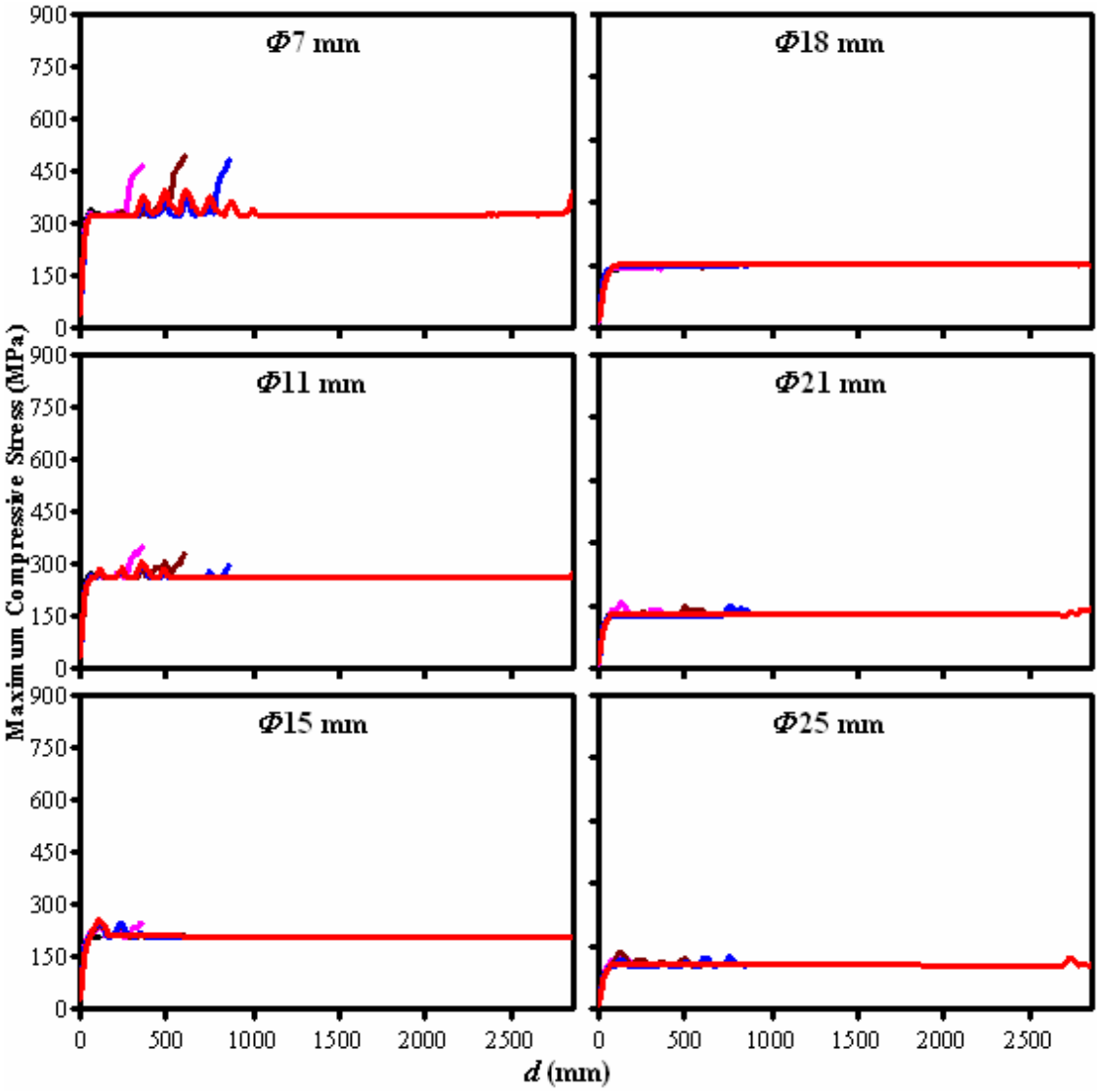

Figure 4.11 Maximum compressive stress vs. d when K=2x10^4 N/m.

4.3.2 Medium Rock Case

The results in case of medium rock are given in Figure 4.12.

When the rock hardens, the compressive portion of σ_{i2} weakens, and cannot create the zigzag regions seen in case of soft rock. When 3000 mm drill bits are concerned, the only difference between soft and medium rock cases is those regions that disappear when the rock hardens. In case of medium rock, wave superposition has minor effect, and the highest compressive stresses along the drill bit are mostly reached by A_1.

That also prevents length effects to have importance, so the results are not dependent on length. Being dependent on A_1, the stresses decrease with thickness.

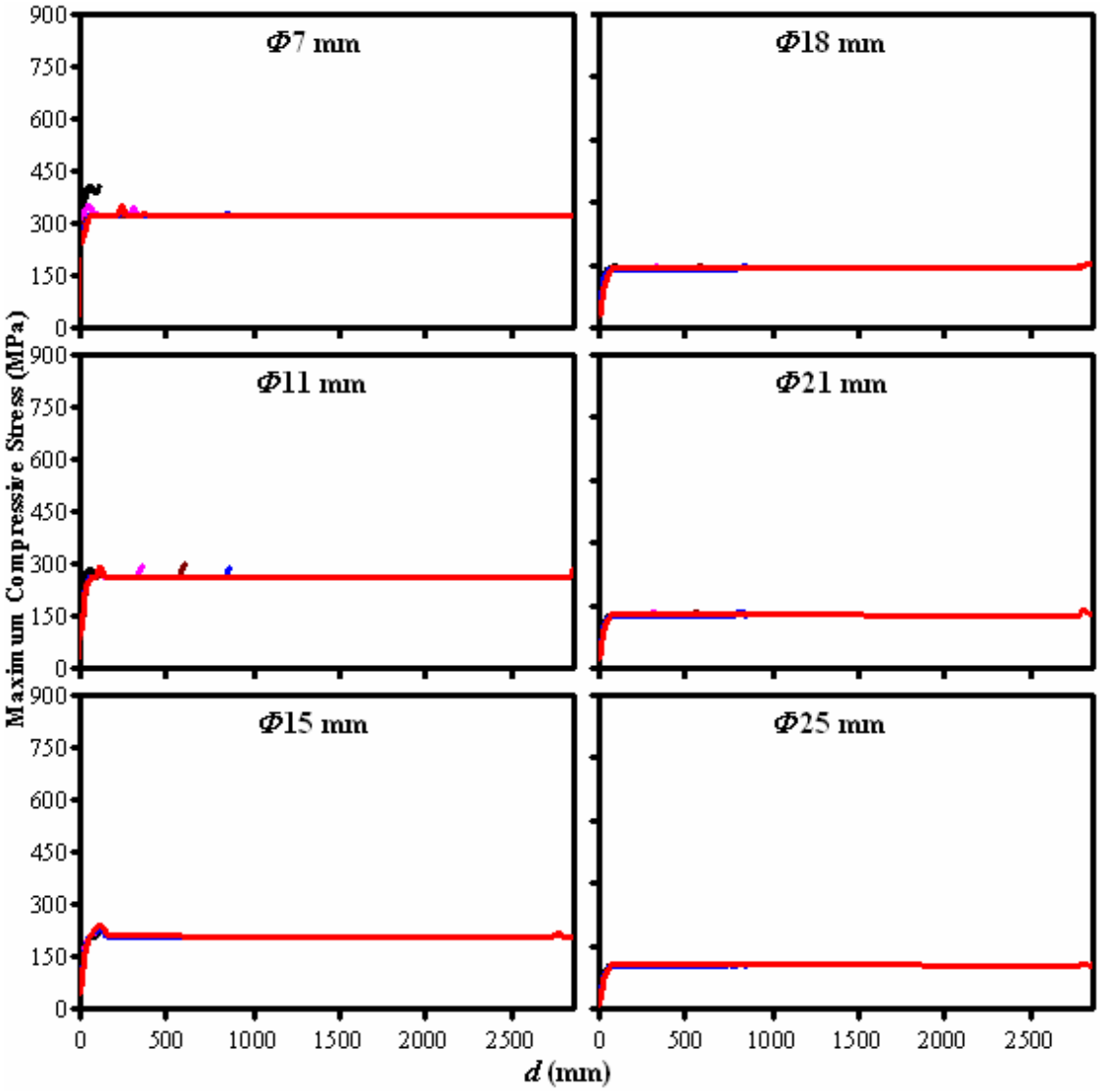

Figure 4.12 Maximum compressive stress vs. d when K=2x10^6 N/m.

4.3.3 Hard Rock Case

The results in case of hard rock are given in Figure 4.13.

When the rock hardens, σ_{i1} is reflected by the rock being mostly compressive. At the proximity of drill bottom, σ_{i1} and its reflection superpose creating higher maximum compressive stresses than A_1 creates individually. The compressive σ_{r1} increases the stresses also in the proximity of drill shank by coinciding with its reflection from the c-s change (A_2). The length and magnitude of those high stress regions, which do not exist in cases of soft and medium rock, reduce as the drill bit gets thicker.

Regarding 250, 500, 750 and 1000 mm long drill bits, it can be said that, the drill bit bottom is the most compressed part of the bit, and the stresses decrease with thickness and length.

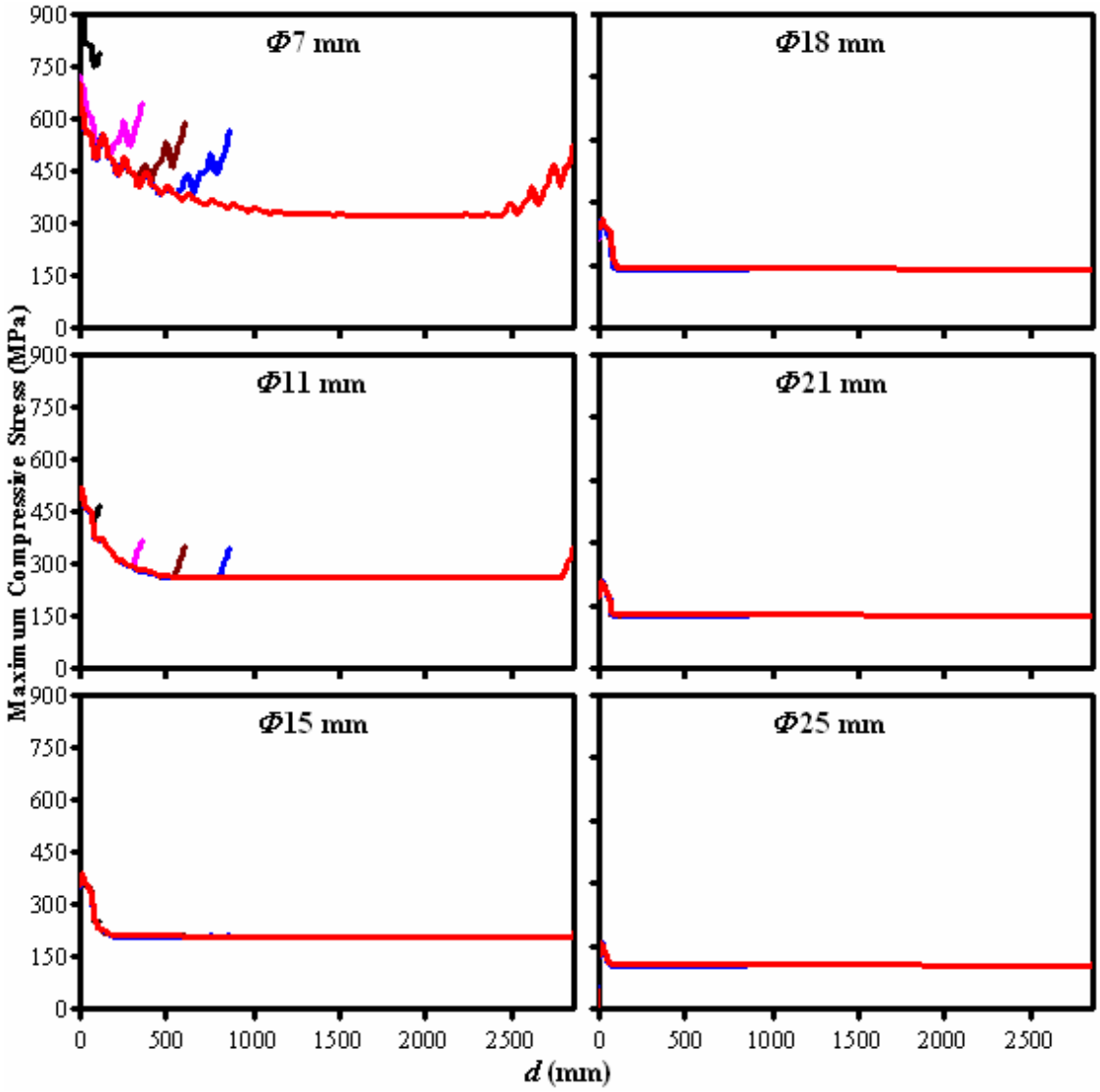

Figure 4.13 Maximum compressive stress vs. d when K=2x10^8 N/m.

4.4 Conclusion

In this chapter, maximum tensile and compressive stresses seen along drill bits with different dimensions have been investigated in varying rock hardness conditions.

When tensile stresses are concerned, stresses are higher when the rock is soft or hard, while they reduce in case of medium rock. Thinner drill bits are more critical than thicker drill bits. Longer drill bits, which are more critical in case of soft rock, are safer in case of hard rock.

When the rock is soft, the critical region is the region, where the drill rod is attached to the drill shank; as the rock gets harder, stresses at the proximity of the drill bottom increase to compete.

When compressive stresses are concerned, for the thicker drill bits, the hardening rock squeezes the drill bit bottom, while cannot affect other regions at all. For the thinner drill bits, soft rock can create highly compressed regions near the drill shank, but the hard rock case is more critical, where the whole drill bit is under high compression, the drill bit bottom being the most squeezed part.

The stresses decrease with thickness as a general rule, and decrease with length at the critical hard rock case that is mentioned.

CHAPTER 5

SIMULATION OF CHISELING TEST

5.1 Introduction

Chiseling test is used in order to prove hammer drill bits under axial impact loading. For this study, the test is performed with two drill bits having different thicknesses, and it is seen that the drill head fractures in the thinner drill bit, while the thicker bit stands, although the same conditions are applied to both.

In this chapter, simulation of chiseling test with axisymmetric finite element method is performed, and the stress distribution in the drill head arising during chiseling test is revealed in order to explain the fracture of the thinner drill bit. Since the reason of a fracture is being searched, especially the tensile stresses at the drill head are focused on.

Throughout the chapter, unlike the previous chapters, tensile stresses are taken to be positive.

Below, first, test setup and test results, then, simulation results and interpretation are given.

5.2 Test Setup and Results

For the test, the drill bit is fixed to move in axial direction only, as can be seen in Figure 5.1. Hammering is then performed by the drilling machine without rotating action. The drill bit contacts a steel cylindrical rebar eccentrically, and the rebar is buried into a large concrete block.

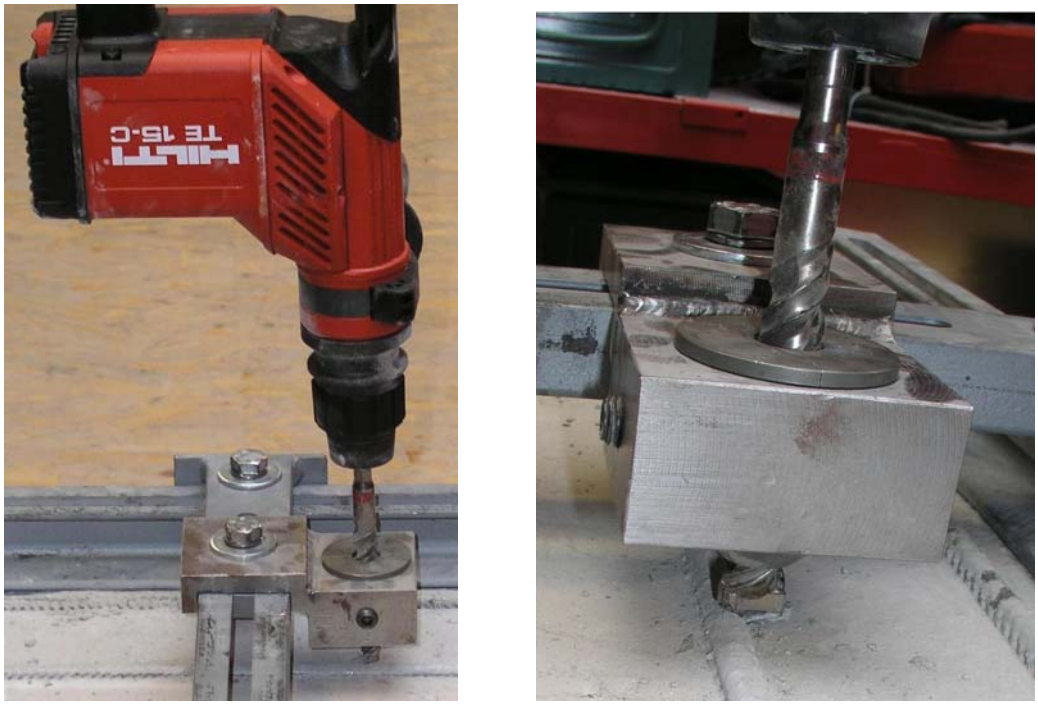

Figure 5.1 Chiseling test setup.

The aim of the chiseling test is to compare the service life of hammer drill bits, taking the fracture times into consideration. According to the test results performed with 350 mm long, Φ7 mm and Φ9 mm drill bits, the thinner drill bit fractures in 5-10 seconds,

while the thicker one stands after 120 seconds. The crack seen in the thinner drill bit is given in Figure 5.2.

Figure 5.2 350 mm long, Φ7 mm drill bit after fracture.

As can be seen in Figure 5.2, the crack occurs at the drill head.

5.3 Simulating Chiseling Test

In order to simulate the chiseling test, a cylindrical rebar and a concrete block are placed under the drill bit model, as can be seen in Figure 5.3. Since axisymmetric approach is used, the eccentricity of the rebar is omitted. The bottom of the block is constrained in axial direction.

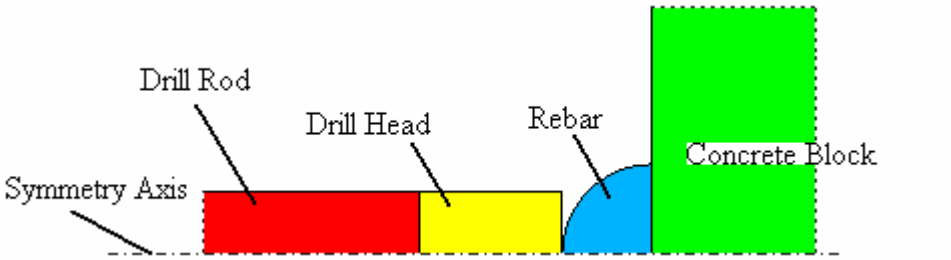

Figure 5.3 The rebar and the concrete block added to the model.

5.3.1 Dynamic Simulation

The effect of the cylindrical geometry of the rebar on the tensile stress distribution in the drill head is given in Figure 5.4.

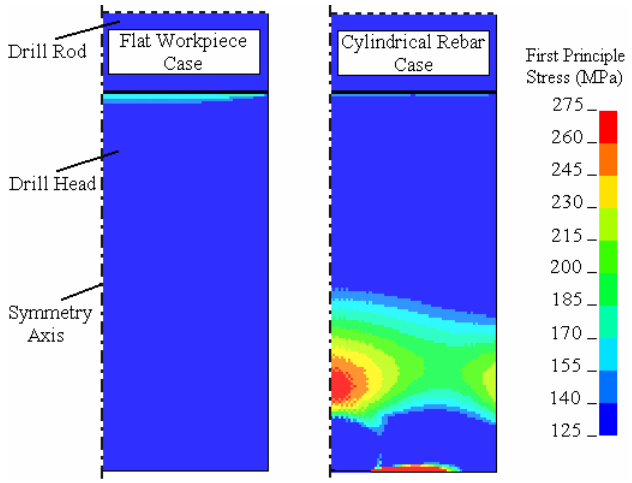

Figure 5.4 First principal stress distribution in the Φ7 mm drill head.

The results in Figure 5.4 are taken at the instant that the first principle stresses reach the maximum values. As it is seen in the figure, a cylindrical rebar leads tensile stress concentrations in the drill head.

High maximum principle stresses are due to the radial and circumferential stresses (see Figure 5.5). Shear stresses are not strong enough to result in maximum principle stresses much greater than radial or hoop stresses.

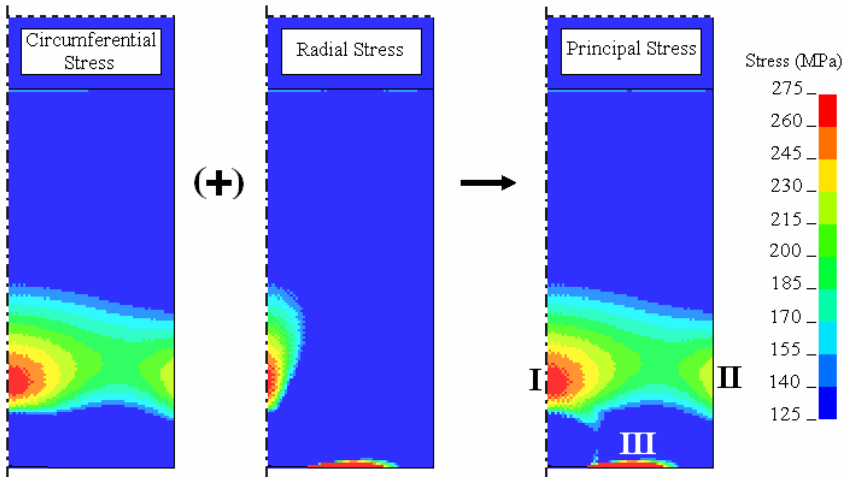

Figure 5.5 Distribution of stress in Φ7 mm bit head (cylindrical rebar case).

As designated in Figure 5.5, there are three main tensile stress concentration regions in the drill head. The one at the axis suffers both radial and circumferential tension, and is denoted by I. Region II is under circumferential tension, while Region III is under radial tension.

The results in the figure are given for the thinner drill bit, but these three regions can also be seen in the thicker drill bit, as it is going to be seen in the following graphs (go to Figure 5.8.b).

For Region III, unlike Regions I and II, it is not possible to achieve a solution that is not dependent on mesh density. The results with respect to mesh density are given in Figure 5.6.

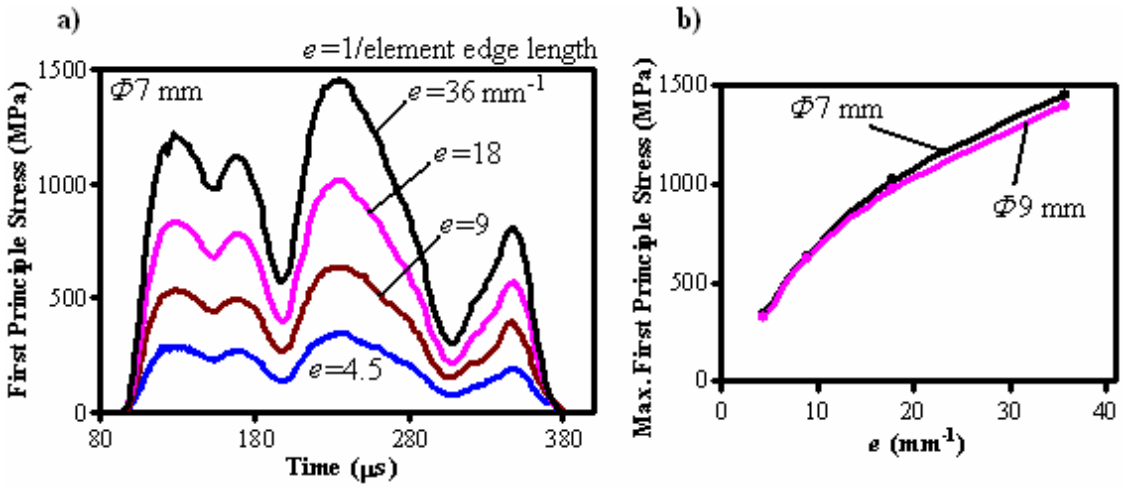

Figure 5.6 a) Tension at the most critical point of Region III (Φ7 mm bit). b) Max. tension reached at that point (Φ7 and Φ9 mm bits).

The results in Figure 5.6 are given with respect to parameter *e*, 1/element edge length, since local mesh refinement is performed in Region III. It is obvious in the figure that, the stress in Region III does not converge to a solution when *e* is increased.

Looking at the results, it can be said that there is a tensile stress concentration in Region III; however, it is impossible to be sure of the magnitudes and whether the thicker or the thinner drill bit is more critical.

The tensile stresses arise in the drill head because of the axial compressive stress waves sent by the piston impact. A compressive wave coming from the top of the drill bit forces the drill head to move downward in axial direction. While the material near the axis is prevented by the rebar, outer portion can move. The opposition of the rebar compresses the head in axial direction, and simultaneously, the outer portion pulls the drill head and creates tensile stresses.

This is approved by Figure 5.7, in which the stress time histories of the most critical points from Regions I and II are compared with the compression of the head with respect to time. As a measure of the compression of the head, the axial compressive force applied on the head by the rebar is employed after being divided by the cross-sectional area of the head. Both Φ7 mm and Φ9 mm results are given in the figure.

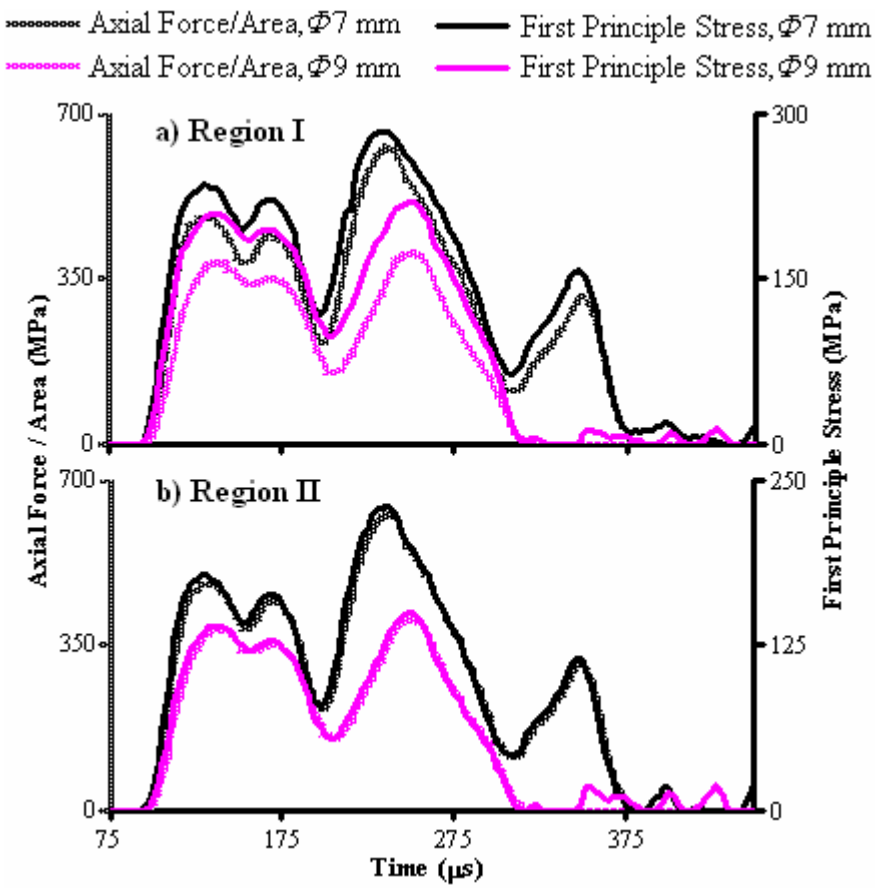

Figure 5.7 Head compression and tensile stresses in Region I and Region II.

In the two plots given in Figure 5.7, the porous lines represent the axial compression time history of the drill head, which are, naturally, the same in both plots. Observing these lines, it can be noticed that the compression of the drill head is weaker in the thicker drill bit.

The solid lines are the stress time histories of the most critical points from Regions I and II. As it is seen in the figure, the behaviors of tensile stress and head compression with respect to time are parallel; notwithstanding, (tensile stress) / (head compression) ratio can change with respect to material point and thickness.

It can also be observed in Figure 5.7 that, the stresses in thinner and thicker drill bits reach the maximum points at different instants. In Figure 5.8, the stress distributions at the most stressed instants in thin and thick drill bits are compared.

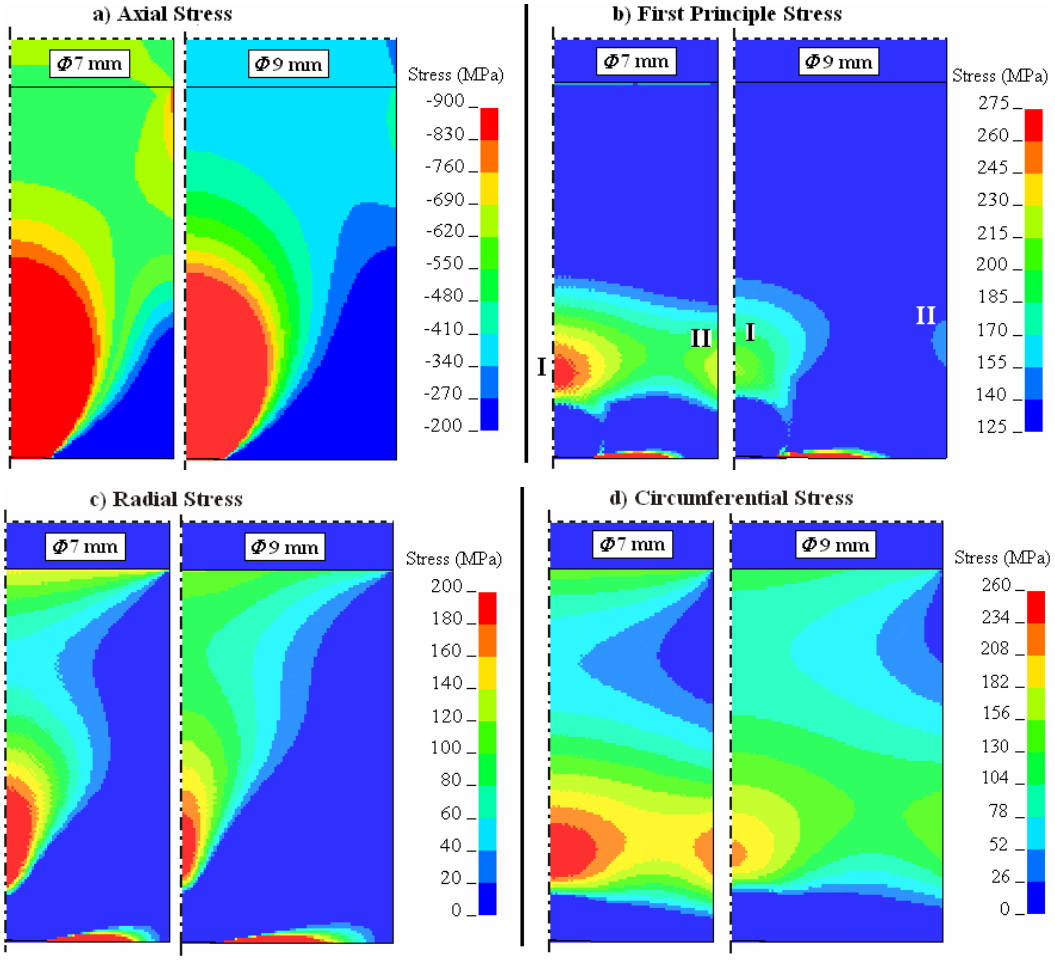

Figure 5.8 Stress distributions in the drill head with respect to thickness.

In Figure 5.8, different scales are used in figures b, c and d, in order to reveal the differences between thinner and thicker drill bits better. The radial, circumferential and hoop stresses can be compared with each other in Figure 5.5. In addition, red color indicates greater stresses (magnitude wise) both in tension and compression cases.

Observing Figure 5.8.a, it can easily be said that the thinner drill head is compressed more, which was a fact revealed before. Additionally, Figure 5.8.b explicitly reveals that the thinner drill bit is more critical in terms of tensile stresses both in Region I and Region II, which are denoted in the figure. Figures 5.8.c and 5.8.d show the radial and circumferential stress results, which are the roots for the differences in first principle stress results.

5.3.2 Static Simulation

In the static simulation of the chiseling test, unlike the dynamic simulation model, the piston does not hit the anvil but applies a representative static force on it. Static results are obtained by the commercial finite element code DEFORM.

In Figure 5.9, the static and dynamic results of tension are given. For the dynamic results, the scale contours given in Figure 5.8 are used.

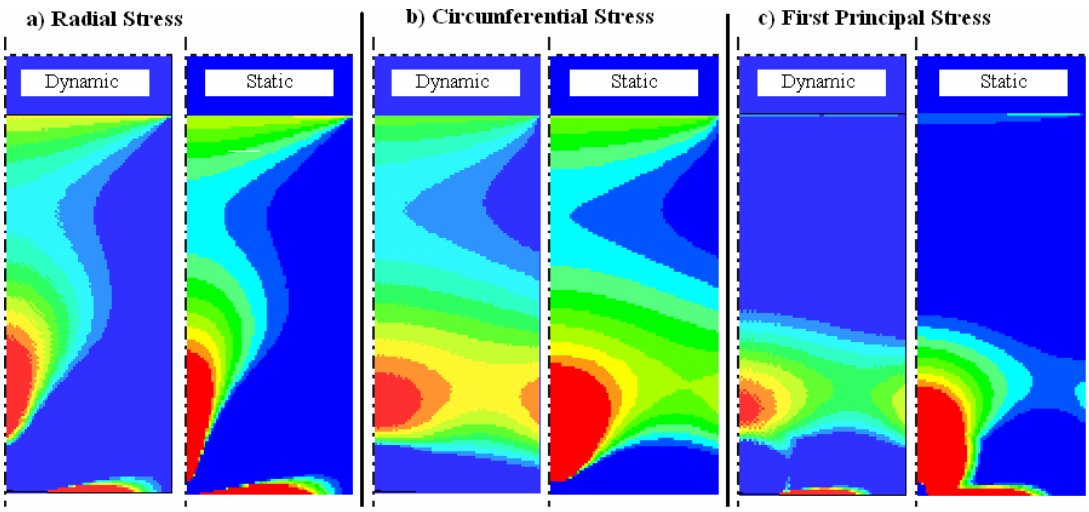

Figure 5.9 Stress distributions in the drill head for static and dynamic cases.

As it is seen in Figure 5.9, static simulation is successful in detecting tensile stress concentration regions in the drill head. However, it predicts these regions to be closer to the rebar than dynamic simulation does.

When the static results are resorted to distinguish thicker and thinner bits, as can be seen in Figure 5.10, the radial and hoop stress concentration regions are greater for a thinner drill bit.

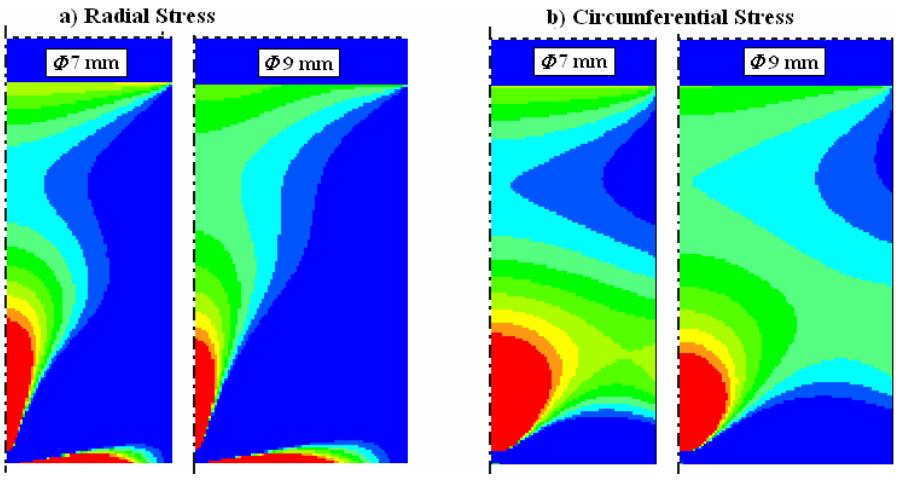

Figure 5.10 Stresses in the drill head with respect to thickness (static solution).

Indeed, the differences in the stresses seen in thinner and thicker drill bits can be partially explained in static means: The same stress wave coming from the drill shank hits a thinner rod in a thinner drill bit. In other words, the same force is applied on a thinner part. However, another effect of thickness is widening stress waves and leading stress wave superposition, which cannot be represented in a static analysis.

Hence, it is logical for a static analysis to capture differences between thin and thick drill bits to some extent; still, dynamic analyses are revealing the differences better, as it is noticed when Figure 5.8 and 5.10 are compared.

5.4 Interpretation of the Results

Considering the effect of the rebar provoking the formation of tensile stress concentrations, an analogy between axisymmetric and 3-dimensional (3-D) models can be drawn.

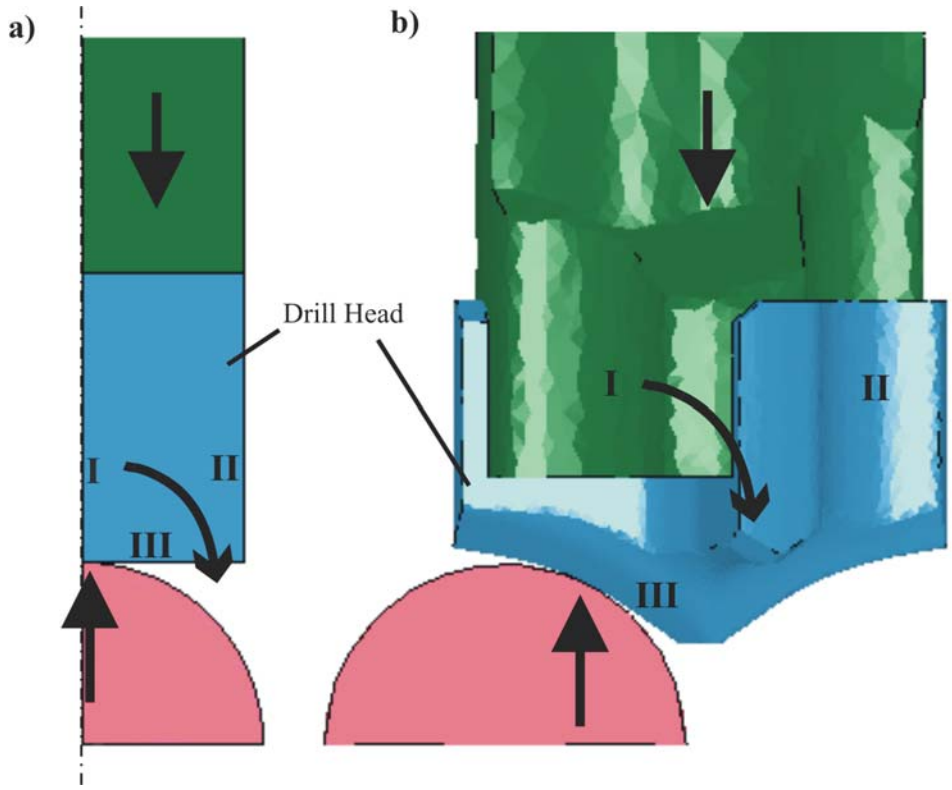

Figure 5.11 Tensile stress regions in axisymmetric (a) and 3-D (b) models.

It was stated before that, the tensile stresses in the axisymmetric model are triggered by the partial opposition of the rebar to the movement of the drill bit. The material that are not stopped by the rebar pull the material stopped by the rebar, and tensile stresses occur, concentrated on the three regions denoted by I, II and III in Figure 5.11.a. The same mechanism can also work in the real 3-D case, and create the same regions, as designated in Figure 5.11.b.

These regions can also be shown on the picture of the fractured drill bit (see Figure 5.12).

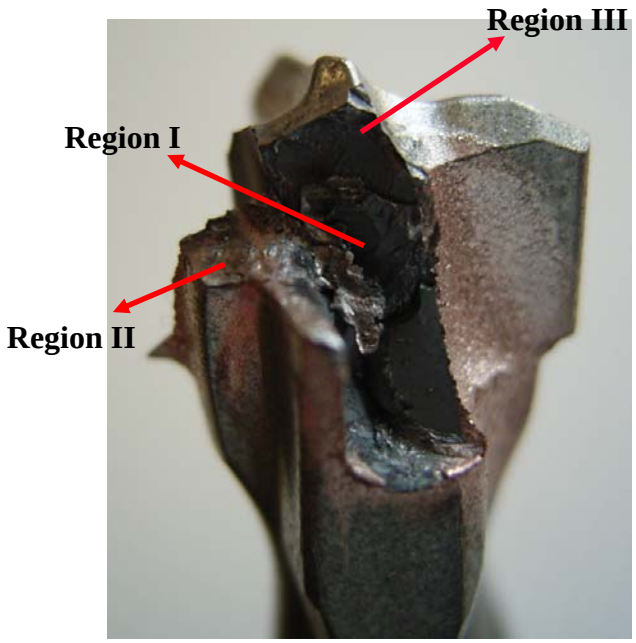

Figure 5.12 Stress concentration regions shown on fractured drill head photo.

The bit in Figure 5.12 seems to be ruptured by a crack that has started from one of the tensile stress concentration regions (I, II or III) and spread to the others. At that point, it is hard to state the one initiating the rupture, because stress magnitudes in Region III cannot be obtained by finite element method.

Still, it is clear that Region I is more critical than Region II. Although to be sure is impossible, the general prospect of stresses in the drill bits makes it reasonable to expect higher stresses for the thinner drill bit in Region III, too.

As the regions that are responsible from the fracture are all more critical in the thinner drill bit, the difference between thinner and thicker drill bits in fracture behavior, which is revealed by the chiseling test, is far away from being surprising.

Indeed, in any drilling condition that the drill bottom is in full contact with the workpiece, tensile stress concentrations can be created in the drill bit. These tensile stresses will be greater in case of higher head compression. In Chapter 4, it was stated that the head compression is severer in case of hard rock, in thinner and shorter drill bits. That is, these conditions have a great potential to cause fracture in the drill bit.

A point worth noting is that, the tensile stress concentration regions and the differences between thin and thick bits can be captured with static analyses, which are much cheaper than dynamic analyses. With this property, static analyses can also be used for the simulation of the full 3-D model, which may give other clues about the nature of the drill head crack.

CHAPTER 6

CONCLUSIONS & FURTHER RECOMMENDATIONS

The task of a hammer drill bit is to transfer the energy introduced to it by the percussive loading to the workpiece. The drill bit receives the energy by means of an axial stress wave, and converts it into successive axial incident stress waves to hit the rock. The efficiency of energy transfer and the stress history of the drill bit during drilling are mostly dependent on the properties of these stress waves.

In hand-type hammer drill bits, being different from hammer drill bits used in mines and quarries, there exists a c-s discontinuity separating the drill bit into two sections. From the two sections, the drill shank has standard dimensions, while the length and diameter of the drill rod vary with respect to hole dimensions.

The main aim of this study is to investigate the efficiency and stress behavior of hand-type hammer drill bits under percussive loading with respect to drill rod dimensions. Being a very important factor affecting the effect of bit dimensions, rock hardness is also taken into consideration. For the investigation, results taken from dynamic axisymmetric finite element simulations are utilized, and only a single hit is simulated.

The efficiency of hammer drilling process has been studied by numerous authors before. However, the focus was generally hammer drilling of large holes for mining; so, the drill bits were very long and uniform c-s ones. In such drill bits, the efficiency

has a maximum for medium rock hardness, while it decreases for harder and softer rock conditions [23].

In case of a c-s change in the bit, which is covered in this study, the waveforms created by the drill bit are affected by the c-s change. This leads significant changes in efficiency:

To begin with, a c-s change increases the width of axial incident waves. Wide incident waves can superpose during application on the rock, which is a phenomenon that increases efficiency. The effect of wave superposition gains importance as the drill bits get shorter, thinner and as the rock gets softer. The superposition has two significant results:

First, a c-s change modifies the regime of (efficiency vs. hardness) curve. In a drill bit with a c-s change, the efficiency has one more local maximum appearing when the rock is soft enough. It appears at a higher K when the drill bit gets shorter and thinner.

Second, with the help of the superposition and the second maximum, shorter and thinner drill bits are more efficient in case of soft rock.

As another effect of the c-s change, as the drill rod gets thinner, the drill bit produces incident waves which are more suitable for energy transfer to softer rock.

Combining with the effect of wave superposition, when the rock is soft, thinner drill bits are more efficient, and when the rock is hard, thicker bits are more efficient.

In the chapter of efficiency considerations, the results of 24 different drill bit models are given for 9 different rock hardness values. The results are checked with theoretical

hand calculations whenever possible, showing perfect agreement; however, comparing the results with experiments would be a complementary addition to the study.

With the help of experiments, the evaluation of the assumptions made would also be easier (neglecting rotational motion, neglecting spirals on the drill rod, neglecting complex shape of the drill head, simulating a single hit only). Detecting large deviations between theoretical and experimental results would be a sign for the errors in the significant assumptions like neglecting rotational motion, neglecting spirals on the drill rod, neglecting complex shape of the drill head, and simulating a single hit only, assuming that the waves die out until the next hit.

The effect of these assumptions can also be observed by using 3D models and simulating successive hits in future works.

In the following chapter, the maximum tensile and compressive axial stress magnitudes seen along the drill bits under percussive loading are investigated. According to the results, regardless of rock hardness, thinner drill bits are more critical in terms of both tensile and compressive stresses. The maximum stresses are smaller for medium rock, while they increase for hard and soft cases. The length of the bit does not have a significant effect on the results like it has on the efficiency results.

Maximum tensile stresses are reached by the points at the proximity of drill rod – drill shank connection in case of soft rock. In case of hard rock, this region is critical again, while the points from the proximity of drill bottom compete. The points that are very near to the drill bottom can never have high axial tensile stresses, being very near to an unbonded edge that reflects every incoming tensile wave as a compressive wave. However, the most critical case for compressive stresses can be seen in the drill bottom, in case of hard rock, thin and short bit.

In this chapter, only the maximum stress results along the drill bits are given, and the differences between short and long, thin and thick drill bits are revealed and explained. However, any failure criterion is not employed in order to evaluate fatigue or yield in the bit.

In addition, the results are not compared with experiments; however, it would be very beneficial to compare the simulation results with stress and service life measurements.

In the last chapter, the simulation of chiseling test, which is used to evaluate hammer drill bits under percussive loading, is performed, and the experimental results are explained with the help of data obtained from simulations.

According to the experiments, which are performed with Φ7 mm and Φ9 mm drill bits having 350 mm length, there is a significant difference between failure characteristics of the two bits: the thinner drill bit fractures at the drill head in 5-10 seconds, while the thicker one stands after 120 seconds.

When 2D axisymmetric simulations are performed, it is seen that, when a workpiece that is not contacting the whole bottom surface of the bit is used, axial compression of the drill head creates radial and circumferential tensile stress concentrations in the head. In a thinner drill bit, the axial compression of the drill head is greater, leading greater tensile stresses, which explain the difference in fracture behavior between thinner and thicker drill bits.

It was stated in the previous chapter that, higher compression of the head occurs for harder rock, in thinner and shorter drill bits. Consequently, thinner and shorter drill bits have a greater potential of fracture, in hard rock conditions.

In this chapter, it is also noted that the static analysis can capture the tensile stress concentrations in the drill head, too. Hence, being much cheaper than dynamic analysis, static analysis can be used to detect tensile stresses in large 3-D models which can represent the complex geometry of drill bit head better.

The static analysis can capture differences between thinner and thicker drill bits to some extent (until where the length of the drill bit changes the differences between thinner and thicker drill bits), but it can never capture any effect of length, which are created by fully dynamic factors.

REFERENCES

1. Fairhurst, C.: Wave Mechanics of Percussive Drilling, Mine & Quarry Engineering, 27 (1961), pp. 122-130, 169-178, 327,328.

2. Elias, D. A.; Chiang, L.E.: Dynamic Analysis of Impact Tools by Using a Method Based on Stress Wave Propagation and Impulse-Momentum Principle, Journal of Mechanical Design, 125 (2003), pp. 131-141.

3. Lundberg, B.; Okrouhlik, M.: Influence of 3D Effects on the Efficiency of Percussive Rock Destruction, International Journal of Impact Engineering, 25 (2001), pp. 345-360.

4. Chiang, L.E.: Dynamic Force-Penetration Curves in Rock by Matching Theoretical to Experimental Wave Propagation Response, Experimental Mechanics, 44 (2004), pp. 167-175.

5. Chiang, L.E.: Design Optimization of Valveless DTH Pneumatic Hammers by a Weighted Pseudo-Gradient Search Method, Journal of Mechanical Design, 120 (1998), pp. 687-694

6. Muro, T.: Drilling Rate of Rotary Percussion Drill Bits and Rock Characteristics, Journal of Terramechanics, 25 (1988), pp. 191-199.

7. Impact Mechanism, *Retrieved* 16.12.2006, *from* BOSCH Encyclopedia of Power Tools: http://www.wissen-elektrowerkzeuge.de/mdb/data/en/lexika/eopt/impact_mechanism.html.

8. TE-YX (Ø18-40 mm) Drill Bits, *Retrieved* 14.12.2006, *from* HILTI Product Catalog: http://www.hilti.com/holcom/modules/prcat/prca_navigation.jsp?OID=-9311

9. Topanelian, E.: Effect of Low Frequency Percussion in Drilling Hard Rock, AIME Petroleum Transactions, 213 (1958), pp. 393-395.

10. Hartman, H.L.: Basic Studies of Percussion Drilling, Mining Engineering, 11 (1959), pp. 68-75.

11. Dutta, P.K.: The Determination of Stress Waveforms Produced by Percussive Drill Pistons of Various Geometrical Designs, Journal of Rock Mechanics and Mining Sciences, 5 (1968), pp. 501-518.

12. Liu, D.; Li, X.B.: Dynamic Inverse Design and Experimental Study of Impact Pistons, Chinese Journal of Mechanical Engineering, 34 (1998), pp. 506-514.

13. Lok, T.S.; Asce, M.; Li, X.B.; Liu, D.; Zhao, P.J.: Testing and Response of Large Diameter Brittle Materials Subjected to High Strain Rate, Journal of Materials in Civil Engineering, 14 (2002); pp. 262-269.

14. Hustrulid, W.A.; Fairhurst, C.: A Theoretical and Experimental Study of the Percussive Drilling of Rock, Part I and II, International Journal of Rock Mechanics and Mining Sciences, 8 (1971), pp. 311-333, 335-356, 9 (1972), pp. 417-429, 431-449.

15. Lundberg, B.; Henchoz, A.: Analysis of Elastic Waves from Two-point Strain Measurement, Experimental Mechanics, 17 (1977), pp. 213-218.

16. Lundberg, B.; Carlsson, J.; Sundin K. G.: Analysis of Elastic Waves in Non-uniform Rods from Two-point Strain Measurement, Journal of Sound and Vibration, 137 (1990), pp. 483-493.

17. Carlsson, J.; Sundin, K. G.; Lundberg, B.: A Method for Determination of In-hole Dynamic Force-Penetration Data from Two-point Strain Measurement on a Percussive Drill Rod, International Journal of Rock Mechanics and Mining Sciences & Geomechanic Abstracts, 27 (1990), pp. 553-558.

18. Simon, R.: Transfer of the Stress Wave Energy in the Drill Steel of a Percussive Drill to the Rock, International Journal of Rock Mechanics and Mining Sciences, 1 (1964), pp. 397-411.

19. Lundberg, B.: Energy Transfer in Percussive Rock Destruction, International Journal of Rock Mechanics and Mining Sciences & Geomechanic Abstracts, 10 (1973), pp. 381-399, 401-419, 421-435.

20. Lundberg, B.; Karlsson, L.G.: Influence of Geometrical Design on the Efficiency of a Simple Down-the-hole Percussive Drill, International Journal of Rock Mechanics and Mining Sciences & Geomechanic Abstracts, 23 (1986), pp. 281-287.

21. Hawkes, I.; Chakravariy, P.K.: Strain Wave Behaviour in Percussive Drill Steels During Drilling Operations, Mine & Quarry Engineering, 27 (1961), pp. 318-326, 367-373.

22. Lundberg, B.: Microcomputer Simulation of Stress Wave Energy Transfer to Rock in Percussive Drilling, International Journal of Rock Mechanics and Mining Sciences & Geomechanic Abstracts, 19 (1982), pp. 229-239.

23. Lundberg, B.: Microcomputer Simulation of Percussive Drilling, International Journal of Rock Mechanics and Mining Sciences & Geomechanic Abstracts, 22 (1985), pp. 237-249.

24. Lundberg, B.: Efficiency of Percussive Drilling with Extension Rods, International Journal of Rock Mechanics and Mining Sciences & Geomechanic Abstracts, 24 (1987), pp. 213-222.

25. Chiang, L.E.; Elias, D. A.: Modeling Impact in Down-the-hole Rock Drilling, International Journal of Rock Mechanics and Mining Sciences, 37 (2000), pp. 599-613.

26. Lundberg, B.; Okrouhlik, M.: Efficiency of a Percussive Rock Drilling Process with Consideration of Wave Energy Radiation into the Rock, International Journal of Impact Engineering, 32 (2006), pp. 1573-1583.

27. Stöck, M.; Schad, H. P.: Modelling of Stress Distributions in Rock Drill Heads, International Journal of Rock Mechanics and Mining Sciences, 29 (1992), pp. 355-361.

28. SDS-max, *Retrieved* 16.12.2006, *from* BOSCH Encyclopedia of Power Tools: http://www.wissen-elektrowerkzeuge.de/mdb/data/en/lexika/eopt/sdsmax.html.

29. Yıldırım, R.O., *ME 523 Impact Mechanics, Lecture Notes*. 2005: METU, Ankara.

APPENDIX A

REVIEW OF IMPACT MECHANICS

In this appendix, basic impact mechanics theory that is going to be used in the investigation of the stress waves in a hammer drilling system is going to be given.

A.1 One-dimensional Wave Equation

Due to mathematical difficulty, simplifying assumptions are employed in order to achieve approximate solutions for the problem of longitudinal vibrations in an elastic bar. The most elementary of these is known as the one-dimensional wave equation in which it is assumed that plane cross-sections of the rod remain plane during the passage of the strain pulse and that the strain over the section is uniform. The equation is usually written in the form

$$\frac{\partial^2 u}{\partial^2 t^2} = c^2 \frac{\partial^2 u}{\partial x^2} \ , \tag{A.1}$$

where u is the displacement of a bar cross-section, distance x along the bar from its undisturbed position, t is the time and c is the velocity of the wave propagation given by

$$c = \left(\frac{E}{\rho} \right)^{\frac{1}{2}} , \tag{A.2}$$

where E is the elastic modulus and ρ is the mass density of the bar material [1].

Solution of Equation A.1 indicates that the assumed pulse travels with constant velocity c along the bar without changing its shape [1].

Benefiting from the Hooke's Law, the magnitude of the elastic stress wave can be written as:

$$\sigma = E \cdot \frac{\partial u}{\partial x} . \tag{A.3}$$

One can substitute strain $\frac{\partial u}{\partial x}$ with $\frac{\partial u}{\partial t} \cdot \frac{1}{dx/dt}$, where $\frac{\partial u}{\partial t}$ is the particle velocity, and dx/dt is the elastic wave speed c. Denoting particle velocity with v, manipulations lead the relationship between the stress amplitude and the particle velocity:

$$\sigma = \rho \cdot c \cdot v , \tag{A.4}$$

where the product $\rho \cdot c$ is called the mechanical impedance z of the material. The particle motion is in the same direction of wave propagation for a compressive pulse and in the opposite direction to that of wave propagation for a tensile pulse [1].

A.2 Longitudinal Impact of Elastic Bars

When two bars with initial velocities V_1 and V_2 ($V_1 > V_2$) impact each other, one can calculate the amplitudes of the resulting stress pulses. First, as a result of the impact,

the striking ends of the rods start to move with the same velocity V, as can be seen in Figure A.1. That is, the velocity of the striking end of the first bar reduces to V, while that of the second bar increases to V. Thus, the particles of the bars at the interface are compressed with velocities (V_1-V) and (V-V_2), respectively. These compressions create stress waves moving with velocities c_1 and c_2 (see Figure A.1).

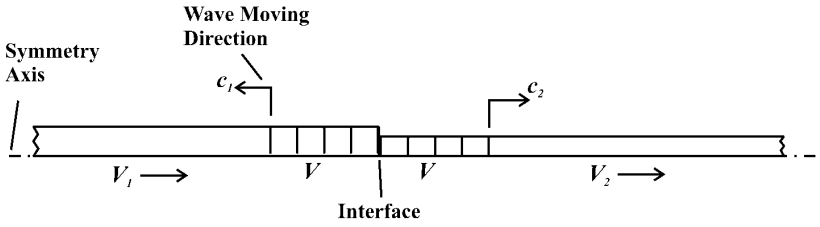

Figure A.1 Co-axial impact of two bars [29].

As the resulting forces on the two bars must be equal, benefiting from Equation A.4:

$$A_1 \cdot \rho_1 \cdot c_1 \cdot (V_1 - V) = A_2 \cdot \rho_2 \cdot c_2 \cdot (V - V_2) \ , \tag{A.5}$$

in which the only unknown is the resulting spatial velocity V. Once V is obtained using equation A.5, the magnitudes of the stress waves in the bars can be found from Equation A.4 [29].

A.3 Reflecting Boundary Conditions

A fixed end reflects compressive or tensile waves without changing shape, magnitude and sign. The stress at the end will be twice the corresponding value when the wave is traveling along the bar [1].

A free end reflects compressive or tensile waves without changing shape and magnitude, but reverses the sign. The displacement and particle velocity of the end of the bar will be twice the corresponding value when the wave is traveling along the bar [1].

Characteristic impedance of a bar is defined as:

$$z_c = A \cdot \rho \cdot c \ , \tag{A.6}$$

where A is the cross-section area of the bar. A singularity, e.g. a characteristic impedance change of a bar on the way of the stress wave reflects a certain portion of the wave energy. In Figure A.2, σ_i, σ_r and σ_t denote amplitudes of incident, reflected and transmitted stress waves; v_i, v_r and v_t denote corresponding particle velocities of the waves; and subscripts 1 and 2 denote the bar sections with different characteristic impedances.

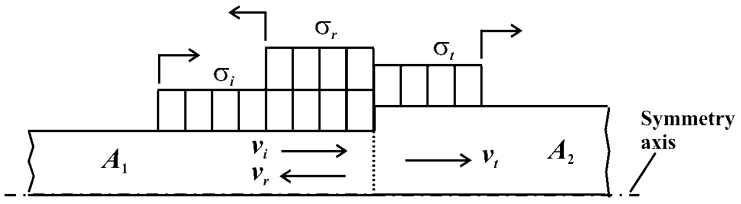

Figure A.2 Wave transmission and reflection [29].

As can be seen in Figure A.2, for the forces and velocities to be equal at the interface:

$$A_1 \cdot (\sigma_i + \sigma_r) = A_2 \cdot \sigma_t \ , \tag{A.7}$$

and

$$v_i - v_r = v_t \ . \tag{A.8}$$

Utilizing Equations A.7, A.8 and A.4, one can find σ_r and σ_t as a function of σ_i:

$$\sigma_t = \frac{2 \cdot A_1 \cdot \rho_2 \cdot c_2}{A_1 \cdot \rho_1 \cdot c_1 + A_2 \cdot \rho_2 \cdot c_2} \cdot \sigma_i \tag{A.9}$$

$$\sigma_r = \frac{A_2 \cdot \rho_2 \cdot c_2 - A_1 \cdot \rho_1 \cdot c_1}{A_2 \cdot \rho_2 \cdot c_2 + A_1 \cdot \rho_1 \cdot c_1} \cdot \sigma_i \tag{A.10}$$

If the interface is unbonded, nothing changes for a compressive wave, but a tensile wave cannot pass any energy to the second bar, so it is reflected as being reflected by a free end [21]. Its effect on the contact is going to be reducing contact forces. The new contact condition can also be solved by using Equations A.9 and A.10. Negative contact force means ceasing contact [29].

APPENDIX B

INITIAL STRESS WAVE

After the piston-anvil impact, the wave interactions between the piston, anvil and the drill shank introduce the initial stress wave to the drill bit. In this appendix, the formation of the initial stress wave $\sigma_{initial}$ is going to be assessed in detail.

According to the theory, the initial impact creates compressive stress waves in the piston and the anvil, which are denoted by σ_{p1} and σ_{a1}, respectively in Figure B.1. If the bodies had infinite length as they have in Figure B.1, σ_{p1} and σ_{a1} would keep traveling forward, forever.

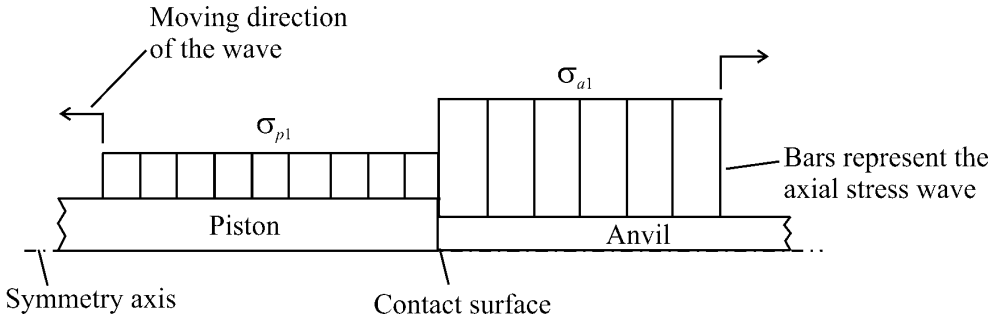

Figure B.1 Waves created by the piston impact, in case of infinite piston.

However, when the piston has a finite length, σ_{p1} hits the free end of the piston, changes sign and turns back to the contact surface as a tensile wave. That tensile wave cannot pass energy to the anvil, but weakens the contact; so that the contact cannot generate σ_{a1} and σ_{p1} any more: it begins to send $\sigma_{a2} < \sigma_{a1}$ and $\sigma_{p2} < \sigma_{p1}$ to the anvil and the piston, respectively (see Figure B.2).

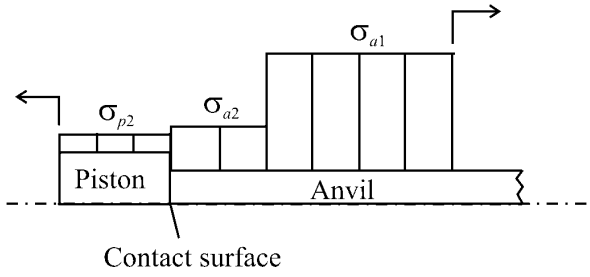

Figure B.2 Waves created by the piston impact, in case of finite piston.

Like σ_{p1}, σ_{p2} is also going to be converted to a tensile wave by the free edge. So, it is also going to weaken the contact. This means a loop in the piston which eventually reduces the contact force to zero, step by step. That mechanism gives a stepped shape to the stress wave generated in the anvil. That phenomenon has been examined by several authors before as given in Chapter 2. More detail can be found in [1,11].

When the generated successive stress waves (σ_{a1}, σ_{a2}, σ_{a3}, etc.) pass to the drill shank, the obtained waveform is called the initial stress wave, $\sigma_{initial}$. In Figure B.3, theoretical and simulated forms of $\sigma_{initial}$ are given for infinite and finite piston length.

In order to be able to make the calculations easier, the curvatures of the anvil are not included in the models. Equations A.4 and A.5 are used for the calculations.

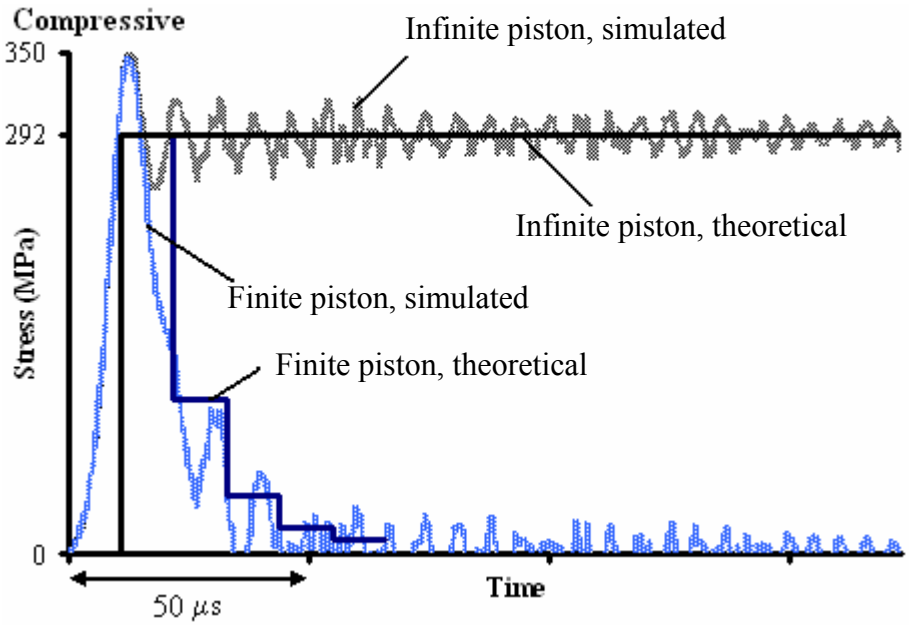

Figure B.3 Theoretical and simulated $\sigma_{initial}$ waveforms.

As can be seen in Figure B.3, theoretically for the infinite piston case, the stress should increase to 292 MPa suddenly, and stay there forever. Theoretically for the finite piston case, the waveform is identical to the infinite piston case until the stepped reduction starts. Then the amplitude reduces to zero step by step.

When FEM simulation is used, for the infinite piston case, the results are parallel to the calculations, except the fluctuations: the stress steeply increases to 292 MPa, but it takes time for it to stabilize there.

For the finite piston case (with FEM), the waveform is identical to the infinite piston case until the stepped reduction starts. The reduction starts much before the stress magnitude stabilizes at 292 MPa, but after it reaches the peak stress value of 350 MPa.

So, because of the fluctuations, the magnitude of the simulated $\sigma_{initial}$ seems to be higher than the magnitude predicted by the theory.

The fluctuations come from the nature of the penalty contact algorithm used by LS-DYNA. This algorithm applies counter forces on the penetrating nodes directly proportional to the penetration distance. These varying counter forces are the sources of the oscillations in the produced stresses. Fluctuations may be reduced by changing contact stiffness or adding contact damping.

For the flat anvil case, the simulation results could be checked with the theoretical results. However, when the curvatures at both ends of the anvil are included, the theoretical models are very hard to be used. In Figure B.4, simulated $\sigma_{initial}$ waveforms are given to reveal the effect of the curvatures.

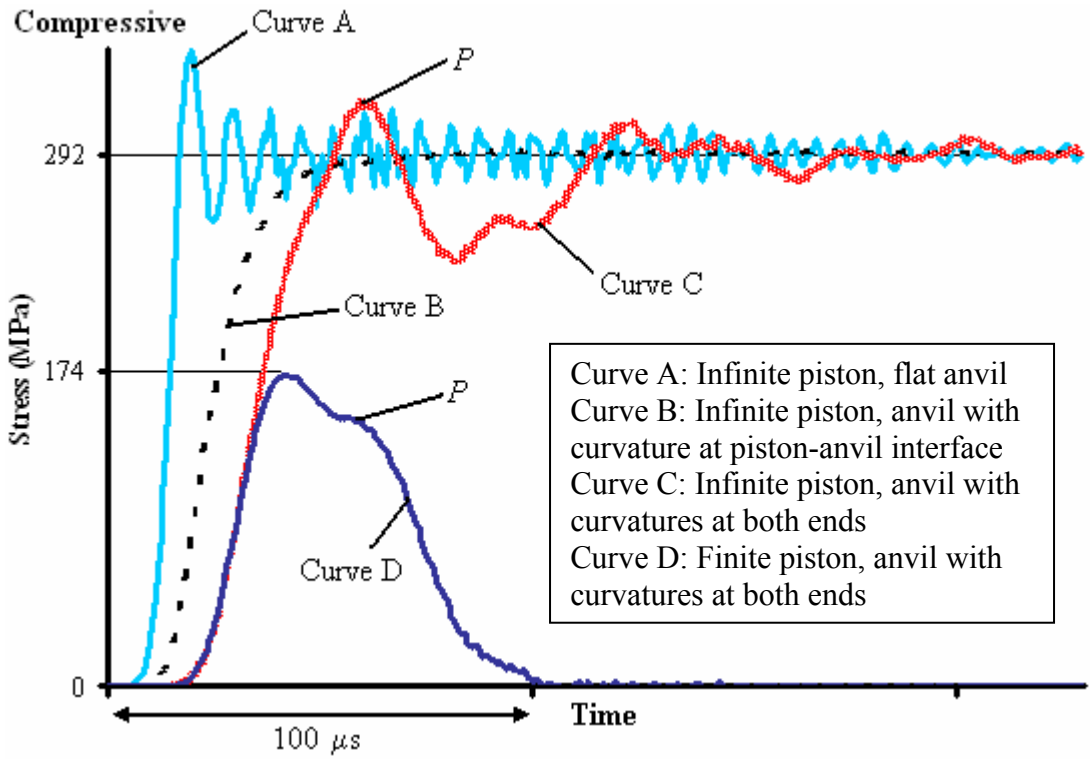

Figure B.4 $\sigma_{initial}$ waveforms predicted by FEM.

When the curves A and B are observed, it can be seen that the inclusion of the curvature at the piston-anvil interface eliminates the fluctuations. In addition, due to the curvature at the piston-anvil interface, the stress increase becomes more gradual. This can be explained as follows:

At the beginning, the piston and anvil touches each other at only one point. However, for the contact stresses to develop, a solid contact surface must be existent between the bodies. This surface develops gradually, which leads the contact stresses develop gradually.

When curves B and C are observed, it can be seen that when the curvature at the anvil-bit interface is included, the arrival of the stress wave to the drill bit is delayed. This can be explained as follows:

At the beginning, the anvil and the drill bit touches each other at a single point. When the compressive stress wave arrives, the end of the anvil is more a free end than a contact surface. So, the leading portion of the wave is reflected back as a tensile wave. This reflection causes the movement of the anvil end towards the bit, so the contact between the bodies develops, and the wave starts to pass to the drill bit.

That reflection has another effect. The reflected tensile portion turns back as a compressive wave, and creates the peak *P*, which is indicated on Curves C in Figure B.4.

When the infinite piston is replaced by the finite one, $\sigma_{initial}$ takes the shape of Curve D. It can be seen that Curve D follows Curve C until the stepped reduction begins, as expected. However, it can reach only half the magnitude of Curve C due to the gradual increase of stress. As indicated on Curve D, the peak *P* has an important role on the form of Curve D: It adds a compressive tail to the wave, so increases the width of the wave.

As a result, $\sigma_{initial}$ waveforms predicted by FEM in case of curved and flat anvil are given in Figure B.5.

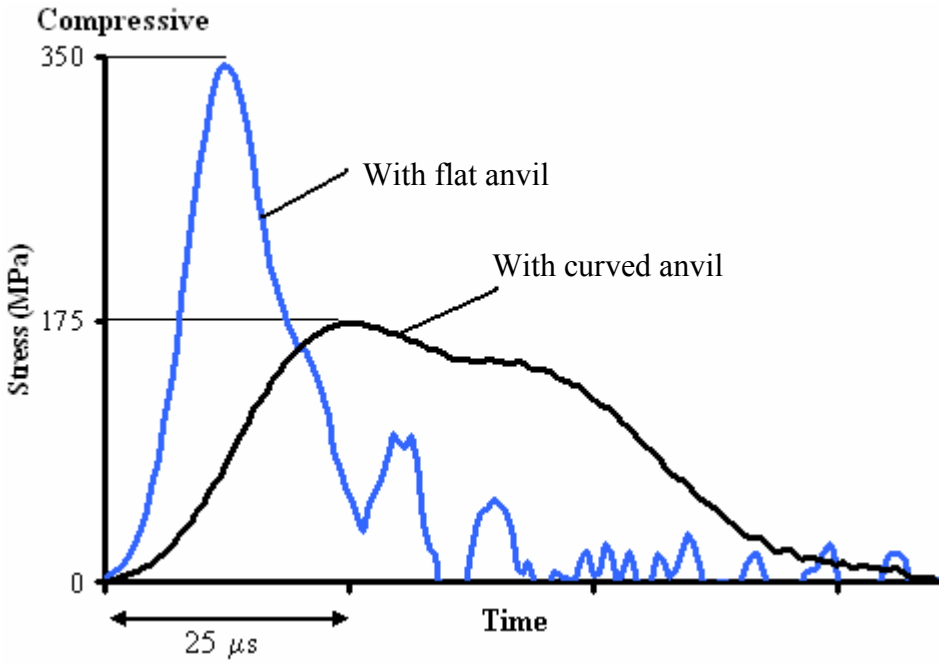

Figure B.5 Simulated $\sigma_{initial}$ waveforms.

In Figure B.5, it can be noticed easily that $\sigma_{initial}$ has lower amplitude but longer wavelength in case of anvil curvatures.

Another point worth noting is, because of the stress wave reflections triggered by the curvatures, some of the initial kinetic energy cannot be transmitted to the drill bit but is trapped in the piston and the anvil. Nearly all of the initial energy is transmitted in case of flat anvil, while %95 is transmitted in case of curvatures.